NOTICE

The quality of this microform is heavily dependent upon the quality of the original thesis submitted for microfilming. Every effort has been made to ensure the highest quality of reproduction possible.

If pages are missing, contact the university which granted the degree.

Some pages may have indistinct print especially if the original pages were typed with a poor typewriter ribbon or if the university sent us an inferior photocopy.

Reproduction in full or in part of this microform is governed by the Canadian Copyright Act, R.S.C. 1970, c. C-30, and subsequent amendments.

AVIS

La qualité de cette microforme dépend grandement de la qualité de la thèse soumise au microfilmage. Nous avons tout fait pour assurer une qualité supérieure de reproduction.

S'il manque des pages, veuillez communiquer avec l'université qui a conféré le grade.

La qualité d'impression de certaines pages peut laisser à désirer, surtout si les pages originales ont été dactylographiées à l'aide d'un ruban usé ou si l'université nous a fait parvenir une photocopie de qualité inférieure.

La reproduction, même partielle, de cette microforme est soumise à la Loi canadienne sur le droit d'auteur, SRC 1970, c. C-30, et ses amendements subséquents.

Canada

Maximum Likelihood Sequence Estimation of Quadrature Pulse-Overlapping Modulated Signals

Slimane Ben Slimane

A Thesis

in

The Department

of

Electrical and Computer Engineering

Presented in Partial Fulfilment of the Requirements
for the Degree of Doctor of Philosophy at
Concordia University
Montréal, Québec, Canada

October, 1992

ISBN 0-315-84693-3

ABSTRACT

Maximum Likelihood Sequence Estimation of Quadrature Pulse-Overlapping Modulated Signals

Slimane Ben Slimane, Ph.D.
Concordia University, 1992

Constant-envelope Quadrature Pulse Overlapping Modulated (QPOM) signals have good spectral properties suitable to applications using nonlinear or saturated power amplifiers. In this thesis we present a Maximum Likelihood Sequence Estimation (MLSE) receiver structure for QPOM signals and analyze its performance in both Additive White Gaussian Noise (AWGN) and fading channels.

The quadrature pulse-overlapping modulator is first decomposed into a linear encoder followed by a memoryless modulator. The trellis diagram representing this inherent non-redundant coding structure is then used to construct its MLSE receiver. The upper bounds on the average bit error probability in both AWGN and Rayleigh fading channels are derived. Computer simulations are also used to verify the analytical results. Performance of the introduced scheme in fast fading, shadowed mobile satellite channels is also studied. Results show that this scheme outperforms conventional QPSK techniques in fading channels. While maintaining a low constellation density of 4PSK, its performance is comparable to those of 4-state 8PSK Trellis Coded Modulation (TCM) schemes.

The performance of QPOM signals over fading channels can be further improved using some extra redundancy. Based on the new representation of the QPOM scheme, an external convolutional code is combined with the QPOM memory and considered as one

entity to be optimized. This optimization is achieved by maximizing the minimum length of the shortest error event path through the trellis diagram of the equivalent code as well as the product of the squared branch distances along that error event path. The obtained structure is then applied to M-ary QPOM signals

The constant envelope, compact spectrum, superior performance, and low complexity make the QPOM scheme a good choice for portable/mobile satellite communications to achieve the requirements of low cost, small size, and high power and bandwidth efficiencies.

ACKNOWLEDGEMENTS

I would like to express my deep and sincere appreciation to my advisor Dr. Tho Le-Ngoc for his invaluable assistance and constant guidance throughout this research, and for his advice and constructive criticism during the preparation of this thesis.

My appreciation is also addressed to the Government of Tunisia for giving me the chance to come and study here.

I am deeply grateful to my family for their support and patience, especially my parents who gave the best of themselves so that I, my brothers and sisters had the best of everything. I would also like to thank all my friends for their help, encouragement and support throughout my studies.

I dedicate this work

to

my parents

Table of Contents

LIST OF FIGURES

LIST OF TABLES

LIST OF PRINCIPAL SYMBOLS

$\mathbf{A}$	Signal Set of the QPOM Encoder
$\mathbf{A}_i$	Subset of the Signal Set $\mathbf{A}$
a	Fading Amplitude sample
$a(t) = a_I(t) + ja_Q(t)$	Complex Multiplicative Fading
a_d	Number of Paths of Length L along a Trellis
B_D	Fading Bandwidth or Doppler Spread
c_n	Output Symbol of a Convolutional Code at Time nT.
cc_n	Output Symbol of a Concatenated Code at Time nT
$d^2(\mathbf{s}, \hat{\mathbf{s}}), d^2$	Normalized Squared Euclidean Distance Between the two Sequences $\mathbf{s}$ and $\hat{\mathbf{s}}$
$d^2_{\min}$	Minimum Normalized Squared Euclidean Distance
$D^2(\mathbf{s}, \hat{\mathbf{s}})$	Squared Euclidean Distance Between the Sequences $\mathbf{s}$ and $\hat{\mathbf{s}}$
E_b	Average Energy per Bit
E	Average Energy per Symbol
$\mathbf{e}$	Error Event
$E_a\{f(a)\}$	Statistical Average of $f(a)$ over the Random Variable a
f_c	Carrier Frequency
$F(\mathbf{A}_i, \mathbf{e}, D)$	Weight Profile of the Subset $\mathbf{A}_i$ with Respect to an Error Event $\mathbf{e}$
g_i	Generator Matrix of a Convolutional Code
$h(\tau, t)$	Low-pass Impulse Response of a Fading Channel

$H(f, t)$	Low-Pass Transfer Function of a Fading Channel
k	Symbol Size
L	Shortest Error Event Path Length (Time Diversity)
$m(\mathbf{r}, \mathbf{s})$	Metric for the Received Sequence of Vectors **r** and Transmitted one **s**
$m(\mathbf{r}, \mathbf{z}, \rho)$	Metric for the Received Sequence of Vectors **r** and Transmitted one **z** in a Fading Channel with CSI one **s**
$n(t)$	Bandpass AWGN Process
$n_c(t)$	In-Phase Component of the Bandpass AWGN Process $n(t)$
$n_s(t)$	Quadrature Component of the Bandpass AWGN Process $n(t)$
$\underline{n}_I$	Noise Vector corresponding to $n_I(t)$
$\underline{n}_Q$	Noise Vector Corresponding to $n_Q(t)$
N	Length of a Sequence of Vectors
N_0	Single Sided Power Spectral Density of the AWGN
$p(t)$	Double-Interval Overlapping Pulse Shape
$P(f)$	Fourrier Transform of $p(t)$
P_b	Average Bit Error Probability
P_I	Average Bit Error Probability of the In-Phase Component of the Received Signal
P_Q	Average Bit Error Probability of the Quadrature Component of the Received Signal
$P\{\mathbf{z} \rightarrow \underline{\hat{\mathbf{z}}}\}$	Pairwise Error Probability of the Sequences **z** and $\hat{\mathbf{z}}$
$P\{\mathbf{z} \rightarrow \underline{\hat{\mathbf{z}}} \mid \mathbf{a}\}$	Pairwise Error Probability of the Sequences **z** and $\hat{\mathbf{z}}$ Conditioned on the Fading Vector **a**

$r(t)$	Received Signal
$r_I(t)$	In-Phase Component of the Received Signal $r(t)$
$r_Q(t)$	Quadrature Component of the Received Signal $r(t)$
$\underline{r}_I$	Received Vector Corresponding to $r_I(t)$
$\underline{r}_Q$	Received Vector Corresponding to $r_Q(t)$
$\mathbf{r}$	Sequence of N Received Vectors
s(t)	Linear Transmitted Signal
$S(t)$	Equivalent Complex signal of s(t)
$s_I(t)$	In-Phase Component of the Transmitted Signal $s(t)$
$s_Q(t)$	Quadrature Component of the Transmitted Signal $s(t)$
$\underline{s}_I$	Transmitted Vector Corresponding to $s_I(t)$
$\underline{s}_Q$	Transmitted Vector Corresponding to $s_Q(t)$
$s_i(\tau)$	Transmitted Linear QPOM Waveform
$\mathbf{s}$	Sequence of N Transmitted Vectors
$\mathbf{s}_e$	Channel Signal Corresponding to an Error Event $\mathbf{e}$
$S_s(f)$	Power Spectral Density of $s(t)$
T_b	Bit Time Interval
T	Symbol Time Interval
$T(D,N)$	Transfer Function of a given Encoder
$T(\bar{D},N)$	Modified Transfer Function for Rayleigh Fading Channels
$z(t)$	Hard-Limited QPOM Transmitted Signal
$Z(t)$	Equivalent Complex Signal of $z(t)$

$z_I(t)$	In-Phase Component of $z(t)$
$z_Q(t)$	Quadrature Component of $z(t)$
$z_i(\tau)$	Transmitted Hard-Limited QPOM Waveform
$\underline{z}_i$	Transmitted Vector Corresponding to $(z_I(t), z_Q(t))$
$\underline{z}_{Ii}$	Transmitted Vector Corresponding to $z_I(t)$
$\underline{z}_{Qi}$	Transmitted Vector Corresponding to $z_Q(t)$
z_{ij}	Element of the Vector $\underline{z}_i$
α_i	Normalized Euclidean Distance Between Hard-Limited QPOM Signals
β_i	Coefficient Depending on the Pulse Shape $p(t)$
ρ	Channel State Information Sequence Vector
λ	Chernoff Parameter

LIST OF ABBREVIATIONS

AWGN	Additive White Gausian Noise
AM	Amplitude Modulation
CPFSK	Continuous Phase Frequency Shift Keying
DSB	Double Side-Band
EUP	Eulclidean Uniform Profile
FFSK	Fast Frequency Shift Keying
GMSK	Gaussian Minimum Shift Keying
HPA	High Power Amplifier
i.i.d	independent, identically distributed
ISI	Intersymbol interference
MLSE	Maximum Likelihood Sequence Estimation
MSK	Minimum Shift Keying
p.d.f	probabilty density function
PM	Phase Modulation
PSD	Power Spectral Density
PSK	Phase Shift Keying
QAM	Quadrature Amplitude Modulation
QPOM	Quadrature Pulse-Overlapping Modulation

QPSK	Quadrature Phase Shift Keying
Q^2PSK	Quadrature-Quadrature Phase Shift Keying
QORC	Quadrature Overlapped Raised-Cosine
SFSK	Sinisoidal Frequency Shift Keying
SQPSK	Straggered Quadrature Phase Shift Keying
TCM	Trellis Coded Modulation
TWT	Traveling Wave Tube
8PSK	8-level Phase Shift Keying

CHAPTER I

INTRODUCTION

1.1. MOTIVATION

The traditional role of fixed services satellite systems in the telecommunications network has been so far that of providing international trunk connections. The interface with the existing terrestrial network has been therefore limited to the highest hierarchical level of international exchanges. In recent years, new satellite techniques are pushing towards an innovative role which foresees the interfacing of satellite networks at lower hierarchical levels, even at the user's premises and paves the way for the introduction of new applications such as business-oriented closed networks, mobile and portable personal communications. This goal can be achieved mainly if both size and cost of the earth-stations involved in the satellite systems are reduced. Power and bandwidth efficiencies therefore become the important system parameters in designing modulators/demodulators (modems) for these applications.

High power and bandwidth efficient modulation techniques are derived for portable equipment to allow the use of

i) high-efficiency class-C, saturated solid-state power amplifiers,

ii) low-gain, small antenna, and

iii) long duration, low-cost batteries.

High power efficiency also helps to reduce space and heat dissipation and consequently the size of portable equipments. In addition to spectral efficiency, modulation techniques for mobile satellite communications should provide a constant envelope signal and be easy to implement. The first requirement is useful to increase the transmitter power efficiency with the use of nonlinear devices, and the need to communicate over a

channel which is corrupted by severe fading. The second follows from the desire to maintain a low cost and small size mobile terminal.

In recent years efforts have been made in the search of power and bandwidth efficient modulation techniques [1, 3-19]. Different techniques have been proposed. Smoothing the pulse shape of the transmitted signal over one symbol interval is effective [3-6]. The spectrum is improved as its side lobes are considerably reduced. However, the main lobe gets larger, making the modulation scheme inappropriate for narrow band applications. This leads to the adoption of a new approach. This approach consists of spreading the pulse shape over more than one symbol interval [1, 7-17]. The spectrum is improved at almost all frequencies with very low out-of-band. Many modulation techniques have been introduced based on this technique, namely, Interference-and-Jitter-Free-Offset Quadrature Phase Shift Keying (IJF-OQPSK) [1], Gaussian Minimum Shift Keying (GMSK) [14], Tamed FSK [15], etc. Another approach to improve the spectral properties of quadrature modulated signals has been introduced in [18]. This modulation technique is called Quadrature-Quadrature Phase Shift Keying (Q^2PSK), and is designed based on multi-dimensional signal space. It uses two data shaping pulses and two carriers, which are pairwise quadrature in-phase, and creates two more dimensions in addition to the existing two already in use by Quadrature Phase Shift Keying (QPSK) and Minimum Shift Keying (MSK). This scheme was introduced to increase the bandwidth efficiency without substantially altering the average bit error probability.

The performance of these modulation schemes is poor when independent symbol-by-symbol detection is used. This is due to the fact that the type of demodulation ignores the memory inherent in the quadrature pulse-overlapping modulation scheme.

Choosing a modulation technique depends not only on its spectral properties but on its performance as well. The most effective way in selecting a modulation technique is to consider its spectrum and performance simultaneously. Studies showed that using

double-interval overlapping pulse shapes is enough to generate modulated signals with very compact spectra [1, 9, 10]. These techniques are suitable because they introduce a limited Intersymbol Interference (ISI) which can be fully controlled. Furthermore, most of these modulation techniques are generated using direct modulation where the modulation process is done in baseband which facilitates the implementation of the scheme especially if Digital Signal Processing (DSP) is to be used.

Attempts have been made in improving the performance of these schemes [20-24], and different techniques have been used. One of the well known methods is the use of equalization. The main objective of this method is to remove the effect of ISI from the received signal. Some authors have employed a demodulator that exploits the memory introduced by the overlapping pulse shape [20, 21]. This technique observes the signal over a sequence of symbols and decides on one of them, and is known as Maximum Likelihood Sequence Estimation (MLSE) receiver. In AWGN channels, the bit error rate is a function of the minimum Euclidean distance between signal points [27]. Therefore, idealy most of these methods are optimum and the best achievable performance will be that of the interference free system [24].

Although these demodulation techniques are optimum for the AWGN channel, it may not be the case for the fading channel. Studies showed that the minimum Euclidean distance of a given system is considered as a secondary parameter on fading channels [29]. Instead, the time diversity provided by the scheme under consideration, controls the behavior of the system performance and allows the error rate to decrease with signal-to-noise ratio accordingly; usually faster than the inverse dependence commonly found in Rayleigh fading channels [29]. Eventually, this property has not been used in dealing with ISI. Hence, studying and exploiting the time diversity that can be provided by quadrature pulse-overlapping modulation schemes can further improve its performance in fading channels and make it suitable to portable/mobile communication systems.

1.2. THESIS OUTLINE

The main objective of this research is to present a maximum likelihood sequence estimation receiver structure for quadrature pulse-overlapping modulated signals in both AWGN and fading channels. Rather than using coded schemes to achieve this goal, the proposed detection technique makes use of all the memory introduced by the overlapping pulse shape into the modulated signal with no extra redundancy. This detection technique is optimum and can be applied to any double-interval overlapping pulse shape. In fact, the performance of the system is expressed in terms of the pulse shape giving the possibility to select a pulse shape for a compact spectrum and a good performance simultaneously. This technique will make Quadrature Pulse Overlapping Modulation (QPOM) schemes more complete and suitable to applications such as mobile communications and personal communications.

After this introduction, a review concerning the spectral properties of both linear and hard-limited QPOM signals is given in Chapter 2. Chapter 2 starts with the well known QPSK modulation scheme and continue up to the recently developed power and bandwidth efficient modulation schemes. We discuss some of the techniques available in choosing good overlapping pulse shapes, and their effect on the performance of the system. The motivation for the research work, described in the subsequent chapters, will be highlighted and discussed throughout Chapter 2.

In Chapter 3 we introduce a new detection scheme in order to improve the performance of quadrature pulse-overlapping modulated signals. Based on the structure of QPOM signals, a new configuration is obtained. The QPOM modulator then takes the form of a coded scheme defined by two separate blocks. The first block represents the memory introduced by the overlapping pulse shape, and the second block represents a memoryless modulator. Based on this new configuration and the maximum likelihood sequence estimation the demodulator is structured, and its performance over AWGN

channels is derived. The upper bound on the bit error rate is derived in a general form as a function of the transmitted pulse shape. Simulation results are then given for some specific pulse shapes to verify the analytical results. Chapter 3 contains two main parts. The first part deals with linear QPOM signals, and the second part with hard-limited QPOM signals. We also study the performance of Offset-QPOM signals.

In Chapter 4 we analyze the performance of QPOM signals in fading channels. In particular, we are interested in exploiting the time diversity provided by the memory of the overlapping pulse shape in the benefit of optimizing the MLSE receiver. We start Chapter 4 with a general description of the statistical behavior of the fading channel. Then, we derive an upper bound on the bit error rate of QPOM signals in Rayleigh fading channels. This upper bound is given as a function of the transmitted pulse shape. This form of upper bound is very important for the development of good modulation/demodulation schemes. We then discuss the effect of pulse shaping on the performance. Finally we compare QPOM schemes to ideal coherent QPSK and some coded schemes of the same complexity and the same net throughput.

Chapter 5 presents the structure, performance, and realization of combined hard-limited QPOM schemes and convolutional codes for fading channel applications. As a direct result of the structural analysis, we provide solutions to the problem of how to optimize the combined coding/modulation for hard-limited QPOM schemes. The main result of this chapter is the way of combining the memory of the QPOM scheme and that of the outer convolutional code. This result calls for a proper way of defining the memory of the modulation scheme.

Higher bandwidth efficiency can be obtained using multi-level schemes In Chapter 6 we study the application of the results obtained in the previous chapters for the case of M-ary QPOM schemes. The first part of Chapter 6 deals with the performance and realization of uncoded and coded linear 16-QPOM schemes. The second part deals with a

power efficient 16-QPOM scheme. This modulation scheme is designed using two hard-limited QPOM schemes. We provide a comparison between the two schemes in terms of performance and complexity. The coding scheme used is a rate 1/2 convolutional code. The coded scheme is compared to uncoded QPOM and some TCM 8PSK schemes.

Finally, Chapter 7 presents the conclusions and a summary of suggested future research directions.

CHAPTER II

QUADRATURE PULSE-OVERLAPPING MODULATION SCHEMES

The efficient use of frequency spectrum is of great importance for transmission of information in terrestrial, and mobile communication systems. For spectrum conservation, the band occupancy of the chosen modulation scheme has to be small so that as many channels as possible can be used in a given band. This calls for modulated signals with compact spectra.

The main objective of this chapter is to review a class of power and bandwidth efficient modulation techniques known as Quadrature Pulse-Overlapping Modulation (QPOM) schemes. As the name indicates, these schemes use the technique of overlapping pulse shapes in improving their spectral properties.

We start this chapter with a general description of a digital modulated signal. This description is then used to represent and compare two classes of modulation schemes, Quadrature Amplitude Modulation (QAM) and Continuous Phase Frequency Shift Keying (CPFSK) schemes. This comparison shows that QAM schemes are better choice for mobile satellite communication systems due to their ease of implementation by using direct modulation. The second part of this chapter deals with the spectral properties of QAM schemes. We describe the well known QPSK and MSK. From the discussion of their spectral properties as well as their performance, the need for more power and bandwidth efficient modulation schemes is justifyed. We then continue with considering the spectral properties of quadrature pulse-overlapping modulated signals. Reviewing the performance of these modulated signals and the effect of the overlapping pulse shape on the bit error rate, a more efficient detection scheme then seems inevitable.

2.1. REPRESENTATION OF DIGITAL MODULATED SIGNALS

A digital modulated signal can be written in its general form as follows:

$$s(t) = y(t)\cos[2\pi f_c t + \theta(t)], \tag{2.1}$$

where $y(t)$ denotes the amplitude (envelope) of $s(t)$, $\theta(t)$ denotes the phase of $s(t)$, and f_c represents the carrier frequency of the modulated signal.

By expanding the cosine function in (2.1) a new representation of $s(t)$ is obtained as

$$s(t) = s_I(t)\cos 2\pi f_c t + s_Q(t)\sin 2\pi f_c t, \tag{2.2}$$

where the signals $s_I(t)$ and $s_Q(t)$, called in-phase and quadrature components of $s(t)$, are defined as:

$$s_I(t) = y(t)\cos\theta(t) \tag{2.3a}$$

$$s_Q(t) = -y(t)\sin\theta(t). \tag{2.3b}$$

Since the frequency content of these components is concentrated at low frequency (around $f = 0$), they are called baseband (low-pass) components.

Consider the complex envelope $S(t)$ defined as

$$S(t) = s_I(t) + js_Q(t) \tag{2.4}$$

so that

$$s(t) = \mathrm{Re}\left[S(t)e^{j2\pi f_c t}\right], \tag{2.5}$$

where Re[ ] denotes the real part of the complex-valued quantity in the brackets.

The signal waveform $S(t)$ depends on the method by which the binary information sequence is mapped into the set of transmitted waveforms. For example, if $\{c_n\}$ represents the sequence of binary data appearing at the input of the modulator at a bit rate of $1/T_b$ bits/s, then the complex envelope can be written as

$$S(t) = \sum_{n=-\infty}^{+\infty} I_n p(t - nT), \tag{2.6}$$

where $\{I_n\}$ is a complex-valued sequence that depends on the modulation technique and the sequence $\{c_n\}$, T is the symbol interval, and the function $p(t)$ is a pulse shape whose selection constitutes an important signal design when there is a bandwidth limitation on the channel. Bandwidth limitation exists in most communication channels such as mobile satellite communication and indoor communication channels. Hence, power and bandwidth efficient modulation techniques are needed.

From the above representation of digital communications signals, it is observed that the signal is modulated in baseband and then up-converted to the carrier frequency. Thus, a digital modulated signal is completely defined by its complex envelope representation. This representation helps us to reduce the complexity of implementation and gives more flexibility in designing good digital modulation schemes.

The modulated signal $s(t)$ can be generated using the block diagram of Fig. 2.1. This block diagram consists of a baseband modulator and an oscillator. Therefore, in order to generate a new modulated signal we need only to modify the baseband modulator. Depending on the modulation scheme, this modification can be very simple especially when digital signal processing is used [28]. In such a situation only some software need to be changed and no hardware is involved.

Although all modulation schemes can be generated using the block diagram of Fig. 2.1, we emphasize on the two most important classes of bandwidth efficient modulation

schemes, namely, Quadrature Amplitude Modulation (QAM) [24] and Continuous Phase Frequency Shift Keying (CPFSK) [5, 17]. During the past years these two classes have been studied extensively and modulated signals with compact spectra have been obtained.

2.2. QAM AND CPFSK SCHEMES

The equivalent baseband complex envelope of a QAM signal is represented as

$$S(t) = \sum_{n=-\infty}^{+\infty} (A_n + jB_n)p(t - nT), \tag{2.7}$$

where

$$A_n, B_n = \pm 1, \pm 3, \ldots, \pm(M-1),$$

with equal probability. Using Eq. (2.7), the transmitted signal $s(t)$ becomes

$$s(t) = \sum_{n=-\infty}^{+\infty} A_n p(t - nT)\cos 2\pi f_c t + \sum_{n=-\infty}^{+\infty} B_n p(t - nT)\sin 2\pi f_c t. \tag{2.8}$$

We notice that $s(t)$ can be obtained by extracting two separate symbols a_n and b_n from the data stream $\{c_n\}$, and then apply them to two double sideband (DSB) modulations as shown in Fig. 2.2. It is observed that the block diagram of the QAM scheme is similar to the one given in Fig. 2.1. Furthermore, the implementation of this scheme is straightforward since only two low-pass filters are needed.

The power spectral density (PSD) of these signals has the same shape as that of the pulse shape $p(t)$. In fact, the baseband power spectral density can be written as

$$S_s(f) = \frac{1}{T}|P(f)|^2, \tag{2.9}$$

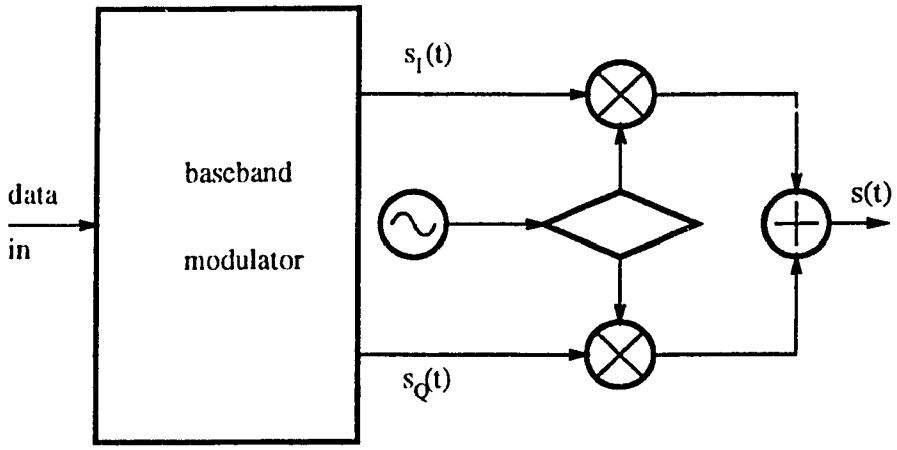

Fig. 2.1 - The block diagram of direct quadrature modulator.

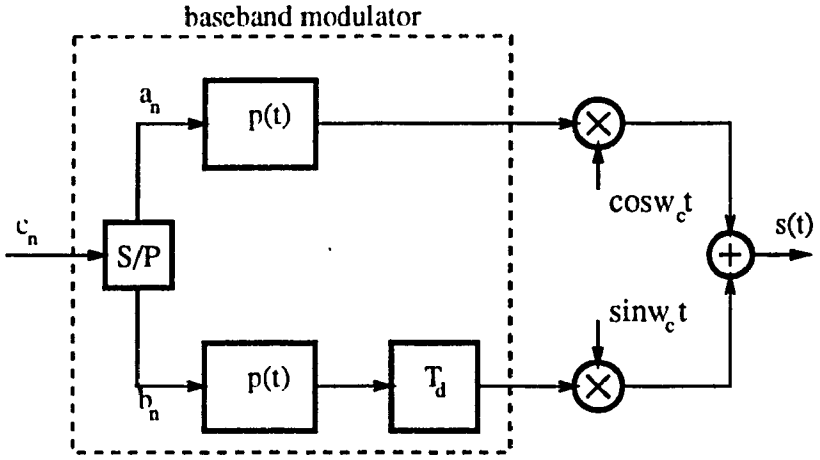

Fig. 2.2 - The block diagram of a QAM scheme.

where $P(f)$ represents the Fourier transform of the pulse shape $p(t)$. By properly choosing this pulse shape, it is possible to generate QAM signals with compact spectra.

Now consider the case of CPFSK modulation schemes. The equivalent baseband complex envelope signal can be written as [24]:

$$S(t) = \exp\{j(2\pi f_d \int_0^t m(\tau)d\tau + \phi)\}, \tag{2.10}$$

where f_d is called the *peak frequency deviation* and ϕ is a uniformly distributed initial phase of the carrier. The signal $m(t)$ is used to frequency-modulate the carrier, and is defined as

$$m(t) = \sum_{n=-\infty}^{+\infty} I_n p(t - nT), \tag{2.11}$$

where in this case I_n is obtained by mapping k-bit blocks of binary digits from the sequence $\{c_n\}$, and $p(t)$ is the pulse shape defined earlier.

We notice that the equivalent complex envelope of the CPFSK scheme is very complicated compared to that of the QAM scheme. For example, if $p(t)$ is a rectangular pulse, $S(t)$ takes the following form [24]:

$$S(t) = e^{j\phi} \sum_{n=-\infty}^{+\infty} e^{j2\pi f_d[\alpha_n T + (t-nT)I_n]} p(t - nT), \tag{2.12}$$

where α_n is defined as

$$\alpha_n = \sum_{k=-\infty}^{n-1} I_k. \tag{2.13}$$

We observe that the complex baseband representation of the CPFSK scheme is not as

simple as that of the QAM scheme. The implementation of its baseband modulator is quite complicated even for the simple rectangular pulse shape. To generate bandwidth efficient CPFSK signals, more spectral efficient pulse shapes are needed. In this case, evaluating the integral in (2.10) becomes questionable and obtaining a compact form for $S(t)$ may not always be possible.

Studies [1, 3-19] showed that by properly choosing the pulse shape $p(t)$, bandwidth efficient modulation schemes can be obtained using either QAM or CPFSK. Because they are easier to implement, quadrature amplitude modulation schemes are more suitable for mobile satellite communications applications. This extra feature will help reduce the size and the cost of the transmitter. In the following sections, we focus our studies to QAM schemes. We describe some of the conventional schemes such as QPSK and MSK, and continue with the technique of generating more power and bandwidth efficient modulation schemes using double-interval overlapping pulse shapes.

2.2.1. Quadrature Phase Shift Keying (QPSK) and Offset-QPSK

A QPSK modulated signal can be generated using the block diagram of Fig. 2.2. The input binary data stream $\{c_n\}$ with a bit rate of $1/T_b$ is demultiplexed into two data streams $\{a_n\}$ and $\{b_n\}$ by a Serial-to-Parallel (S/P) converter. Each data stream is passed through a low-pass filter with impulse response $p(t)$, and then multiplied by a sine carrier. The QPSK modulated signal takes the form of Eq. (2.8) with

$$A_n = 2a_n - 1 \tag{2.14a}$$

$$B_n = 2b_n - 1. \tag{2.14b}$$

The impulse response of the low-pass filter for the QPSK scheme is a *single-interval* rectangular pulse shape.

$$p(t) = \begin{cases} 1, & |t| \le T/2 \\ 0, & elsewhere, \end{cases} \tag{2.15}$$

and $T = 2T_b$.

At any given time interval, the transmitted signal $s(t)$ is a function of both a_n and b_n. Depending on the values of these bits, the phase difference between the in-phase and quadrature components can take one of the values $0, \pm 90^o, \pm 180^o$. A change of sign in both streams will cause a phase transition of 180^o. Usually, the transmi ted QPSK signal is band-limited by a bandpass filter so as to reduce the out-of-band spectral side lobes and prevent interference with adjacent channels. A consequence of this filtering is that the band-limited QPSK signal will no longer present a constant envelope. In fact, the occasional 180^o phase shifts occur now in a nonzero time and cause the envelope to approach zero. This effect is highly undesirable when the signal undergoes nonlinear amplification, as in satellite communications. Actually, a nonlinear amplifier operated at saturation tends to restore the constant envelope of the signal, but at the same time it enhances also the out-of-band spectral side lobes. Thus, the filtering action at the transmitter is destroyed. As a result Intersymbol Interference (ISI) is introduced and a degradation in the performance of the system is obtained.

A reduction of the envelope fluctuations can be obtained by delaying the quadrature component by T_d $(0 < T_d \le T/2)$ seconds relative to the in-phase component. as shown in Fig. 2.2. When $T_d = T/2$, the modulation scheme is called Offset-QPSK or sometimes *straggered QPSK* (SQPSK) [3] because the two quadrature components are offset in time by a bit period T_b. This solution eliminates the possibility of instantaneous phase transitions of 180^o. In fact, phase changes of only $\pm 90^o$ can occur every T_b seconds. As a result, filtered Offset-QPSK signal has a much smaller envelope fluctuation than the QPSK signal. Consequently, the absence of fast phase transitions (180^o) means that non-linear amplification will not regenerate the undesired high-frequency components

originally removed by the band-limiting filter.

Experiments show that the spectrum of Offset-QPSK , unlike QPSK, remains almost unchanged after limiting, hence retaining its band-limited nature almost in its entirely [31]. Spectral advantages of Offset-QPSK comes mainly from the fact that this modulation technique avoids the large phase transition of 180^o associated with the QPSK format. This suggests that further suppression of spectral spreading in band-limited nonlinear applications can be obtained if the Offset-QPSK signal can be modified in such a way that phase discontinuities are avoided. This can be thought of as an obvious motivation for designing constant-envelope quadrature amplitude modulation schemes with continuous phase.

2.2.2. Minimum Shift Keying Modulation

Minimum Phase Shift Keying (MSK) is a form of Offset-QPSK with continuous phase, in which the pulse shape is chosen as

$$p(t) = \begin{cases} cos(\pi t/T), & |t| \leq T/2 \\ 0, & elsewhere, \end{cases} \tag{2.16}$$

rather than the usual rectangular pulse shape. Because of this pulse shaping, the phase transitions of the transmitted signal are not abrupt as in QPSK and Offset-QPSK, but instead the phase moves linearly from one symbol interval to the next. Therefore, with its constant envelope and continuous phase, when the MSK signal is nonlinearly amplified, it suffers no significant spectral spreading into adjacent channels and provides faster spectral roll-off and lower high-order spectral side lobes than the filtered Offset-QPSK signal. However, its spectral main lobe is 50% wider than that of unfiltered QPSK and Offset-QPSK signals. Therefore, the MSK scheme provides better power and bandwidth efficiencies for wide channel spacings and worse efficiencies for narrow channel spac-

ings, relative to QPSK and Offset-QPSK.

MSK scheme can also be viewed as a special case of continuous phase modulation with a frequency deviation of one half the bit rate $1/2T_b$. In this view, it is also known as Fast Frequency Shift Keying (FFSK) because it can transmit faster pulse trains than any other ordinary FSK or PSK with equal bandwidth and signal-to-noise ratio.

It is well known that the Power Spectral Density (PSD) of these signals has the same shape as that of the pulse shape $p(t)$. Using Eq. (2.9), the baseband power spectral densities $S_{qpsk}(f)$ and $S_{msk}(f)$ for QPSK (or Offset-QPSK) and MSK are derived and are given by

$$S_{qpsk}(f) = \left[\frac{\sin\pi fT}{\pi fT}\right]^2 \tag{2.17}$$

$$S_{msk}(f) = \left[\frac{16}{\pi^2}\right]\left[\frac{\cos\pi fT}{1-4f^2T^2}\right]^2, \tag{2.18}$$

where in all cases,

$$\int_{-\infty}^{+\infty} S_s(f)df = 1.$$

From these expressions, it is observed that the PSD of MSK decreases much faster than that of QPSK.

So far we have seen that the baseband pulse shape, phase transition, and envelope fluctuation of a modulated signal are important parameters which affect the spectral properties of a transmitted signal. Furthermore, from the expression of $S_s(f)$, we notice that the spectral properties of the QAM-type modulated signal can be improved by using bandwidth-efficient pulse shapes. With this purpose in mind, a number of authors [1, 5-

19] have proposed different pulse shapes to further improve the spectral properties of these modulated signals. Constant envelope is also a desirable feature specially for non-linear type of channels.

2.2.3. Constant Envelope QAM Schemes

These schemes represent a special case of Offset-QAM. The pulse shape $p(t)$ is chosen in such way that the transmitted signal will have a constant envelope. An Offset-QAM modulated signal can be written as

$$s(t) = s_I(t)\cos 2\pi f_c t + s_Q(t)\sin 2\pi f_c t, \tag{2.19}$$

where in this case

$$s_I(t) = \sum_{n=-\infty}^{+\infty} A_n p(t - nT) \tag{2.20a}$$

$$s_Q(t) = \sum_{n=-\infty}^{+\infty} B_n p(t - nT - T/2). \tag{2.20b}$$

The constant envelope property of the transmitted signal is retained if the pulse shape, $p(t)$, satisfies the following constraints [6]

$$p(t) = p(-t), \qquad \forall\, t \tag{2.21a}$$

$$p^2(t) + p^2(-t + T/2) = \text{constant}, \qquad 0 \le |t| \le T/2. \tag{2.21b}$$

Based on these constraints, a class of pulse shapes represented by

$$p(t) = \begin{cases} \cos[(\pi t/T) - U\sin(4\pi t/T)], & |t| \le T/2 \\ 0, & \textit{elsewhere} \end{cases} \tag{2.22}$$

has been proposed [6], where U is a constant in the range [0, 1/2]. Note that for $U = 0$

the MSK pulse shape is obtained. The resulting modulation scheme is called Sinusoidal Frequency Shift Keying (SFSK).

Further work has been carried out in the search of good pulse shapes [5-14]. Continuous pulse shapes, and pulse shapes with one, or several continuous derivatives have been used [8, 12]. The results showed that it is possible to transmit constant envelope signals with very low side lobes. However, all these results indicate that even though very low side lobes are obtained, the main lobe is always wider than that of QPSK (or Offset-QPSK) signal. The spectral side lobes were further reduced relative to those of the original MSK signal, but their main lobes stayed almost unchanged. Hence, these schemes are not attractive for narrow channel spacings in which the difference of the center frequencies of adjacent channels is smaller than the bit rate frequency, such in some satellite systems.

Detecting quadrature amplitude modulated signals can be done by first down-converting the received signal to baseband, and then passing each component through a matched filter to the pulse shape $p(t)$. A block diagram of the receiver which performs coherent demodulation of the QAM signal is shown in Fig. 2.3. It has been shown in [24] that for single interval pulse shapes, the performance of these schemes is given by

$$P_b = \frac{1}{2} erfc\left[\sqrt{E_b/N_0}\right] \tag{2.23}$$

where $erfc$ represents the complementary error function, and E_b/N_0 is the bit signal-to-noise ratio.

The results obtained in this section show that smoothing the pulse shape over one single interval is limited and a different technique for generating more bandwidth efficient schemes is needed. In fact, it has been shown that [1, 12-19] designing modulated signals with more compact spectra can be achieved by spreading the pulse shape over more than one symbol interval, sometimes referred to as *partial response* schemes.

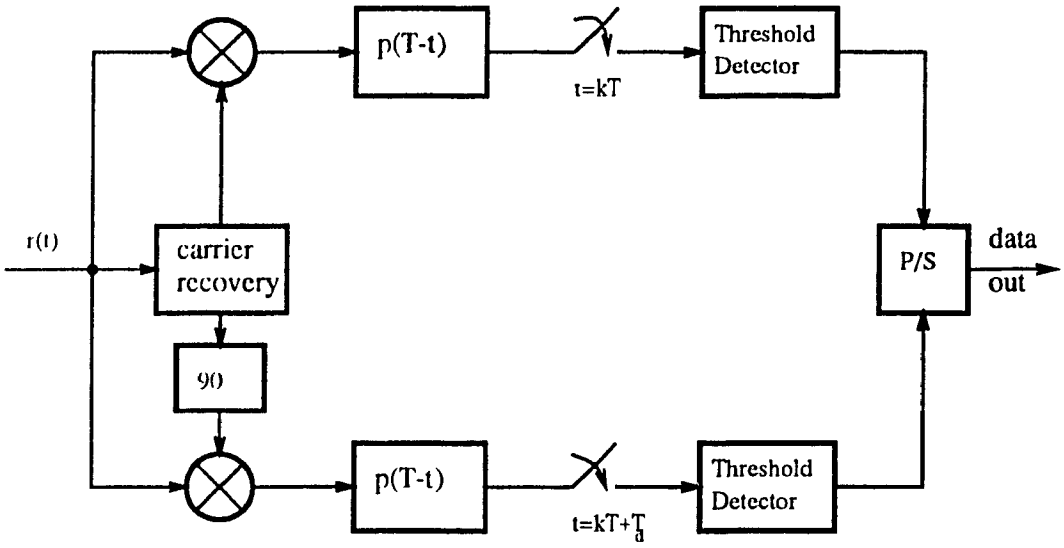

Fig. 2.3 - The block diagram of the QAM coherent demodulator.

By spreading the pulse shape over more than one symbol interval, the spectral properties of the transmitted signal are improved at almost all frequencies and all side lobes becomes considerably lower [17]. However, by doing so, intersymbol interference (ISI) is introduced into the transmitted signal. The transmitted signal at any given symbol interval becomes a function of the present symbol and some of the previous symbols. As a result, independent symbol-by-symbol detection is no more optimum. To be optimum a demodulator has to take into account the effect of the memory introduced by the overlapping pulse shape.

The idea of spreading the pulse shape over more than one symbol interval came from the fact that when a given signal is unlimited in time domain, its frequency domain representation is completely defined over a finite bandwidth. Therefore, if the pulse shape is defined over the interval $]-\infty, +\infty[$ then the transmitted signal will be completely defined over a finite bandwidth. However, the application of this idea was complicated causing some synchronization and delay problems. Consequently, these pulse shapes were truncated or others with finite length were used instead. Results showed that the use of double interval overlapping pulse shapes is enough to generate modulated signals with compact spectra [1, 9, 10].

In the following section, we study the spectral properties of a power and bandwidth efficient transmission technique for digital communications [1]. This modulation scheme is called quadrature pulse-overlapping modulation scheme. Modulated signals are generated by spreading the pulse shape over only two symbol intervals. Using this technique a finite memory is introduced into the system and can be completely exploited at the receiver. The major difficulty is the way of representing this memory in a suitable form that can be efficiently used by the receiver without increasing its complexity substantially.

2.3. QUADRATURE PULSE-OVERLAPPING MODULATION SCHEMES

A quadrature pulse-overlapping modulated signal can be generated from the block diagram of Fig. 2.2. The pulse shape $p(t)$ is a *double−interval* overlapping pulse. The main tool in generating QPOM signals with compact spectra is the selection of this pulse shape.

A common requirement that has been applied in designing pulse shapes is to minimize the intersymbol interference. One solution to this problem resulted in pulse shapes having the following characteristics

$$p(t) = p(-t), \qquad |t| \le T, \tag{2.24a}$$

$$p(t) = 0, \qquad |t| \ge T. \tag{2.24b}$$

These properties were adopted to reduce the ISI caused by the pulse shape and particularly at the sampling points hopping that the degradation in performance would not be pronounced.

With these ideas in mind, the search for bandwidth efficient modulation schemes was studied by different authors [1, 7-19], and several pulse shapes were introduced. These pulse shapes were designed to reduce the out-of-band energy and provide a fast spectral roll-off.

As an illustrative example, we consider the class of double-interval pulse shapes, $p(t)$, defined as [19]:

$$p(t) = \begin{cases} \{\cos(\pi t/2T)\}^{N+1}, & |t| \le T \\ 0, & \textit{elsewhere.} \end{cases} \tag{2.25}$$

As we can see this class of pulse shapes has N continuous derivatives over the interval $]-\infty, +\infty[$. Hence its Fourier transform $P(f)$ decays asymptotically as $|f|^{-(N+2)}$ and its

power spectral density $|P(f)|^2$ as $|f|^{-2(N+2)}$ [12].

The power spectral density of the modulated signal using this class of pulse shapes is derived in [19], and is given by

$$S_s(x) = \begin{cases} \left| (sin(2\pi x)/2\pi x) \prod_{i=1}^{(N+1)/2} i^2/(i^2 - 4x^2) \right|^2, & odd\ N \\ \left| cos(2\pi x) \prod_{i=1}^{1+N/2} (2i-1)^2/\{(2i-1)^2 - 16x^2\} \right|^2, & even\ N, \end{cases} \tag{2.26}$$

where $x = fT$ and $S_s(0) = 1$. Fig. 2.4 shows the normalized power spectral density of a number of double-interval overlapping pulse shapes, $p(t)$. This figure indicates that as N increases, the spectral roll-off of the corresponding QPOM signal becomes faster for high frequencies while the main lobe becomes wider. As a result, the choice of the QPOM signal depends on the trade-off between the main lobe occupancy and side lobes roll-off. In many practical applications, a spectral density of more than 40 dB below the highest spectral density (near 0 Hz) is considered to be negligible. For this reason, pulse shapes corresponding to $N = 0$ and $N = 1$ are more attractive. It is also seen that the spectrum is improved at all frequencies compared to QPSK.

The double-interval pulse shapes $p_0(t)$, $p_1(t)$ corresponding to $N = 0$ and $N = 1$ are given by:

$$p_0(t) = \begin{cases} \cos(\pi t/2T), & |t| \le T \\ 0, & elsewhere, \end{cases} \tag{2.27}$$

$$p_1(t) = \begin{cases} (1 + \cos(\pi t/T))/2, & |t| \le T \\ 0, & elsewhere. \end{cases} \tag{2.28}$$

As shown in Fig. 2.4, the first null frequency of $p_0(t)$ is at $0.75/T$, while that of $p_1(t)$ is at

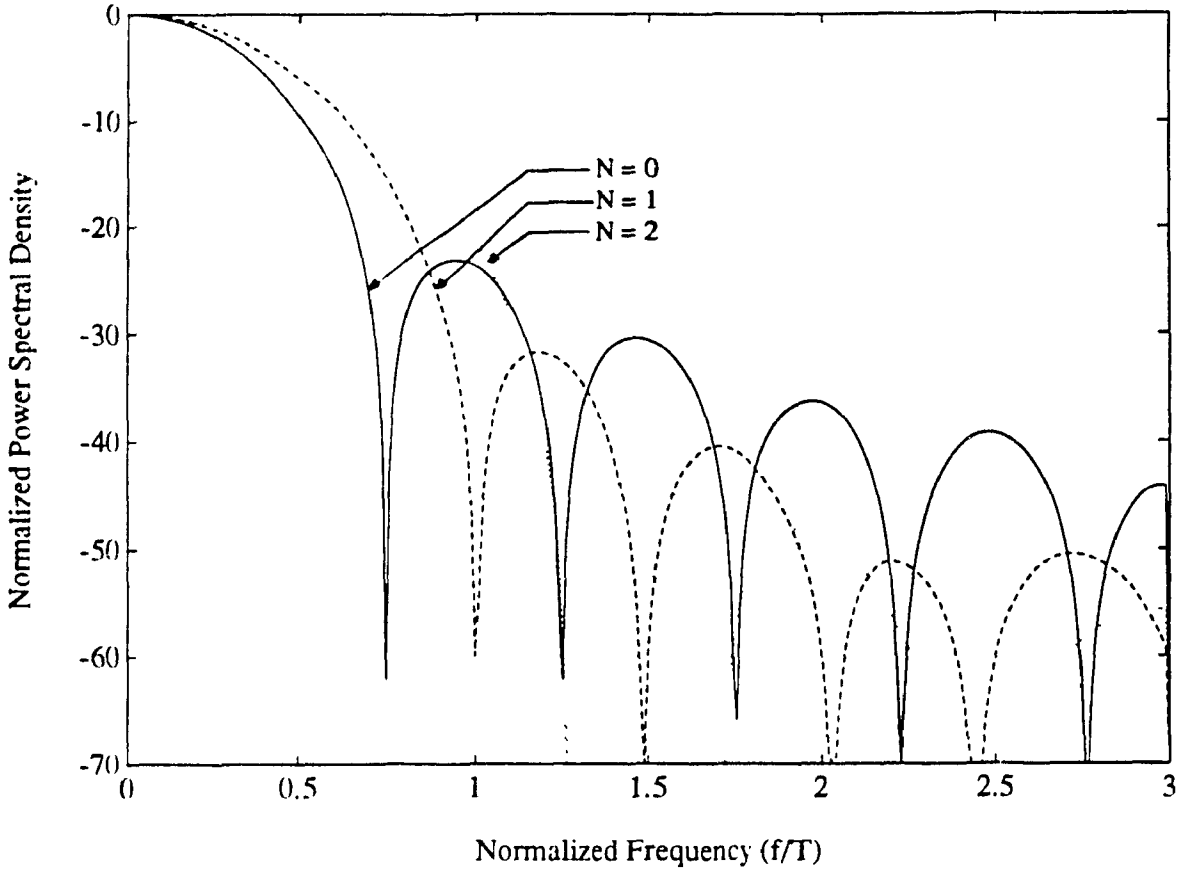

Fig. 2.4 – Normalized power spectral density of QPOM signals, double-interval pulse $p(t) = (cos(\pi t/2T))^{N+1}$

$1/T$. However, the asymptotic spectral roll-off of $p_0(t)$ is of the order of $|f|^{-4}$ while that of $p_1(t)$ is of the order of $|f|^{-6}$. Both of them show spectral advantages over conventional QPSK, and MSK schemes. Note that $p_1(t)$ is also called overlapped raised-cosine pulse shape and used in the QORC modulation scheme [9].

Amoroso [10] presented a class of quasi-band-limited double-interval pulse shapes $p(t)$. This class of pulse shapes is defined as

$$p(t) = \begin{cases} \left[\dfrac{\sin(\pi t/T)}{\pi t/T} \right]^N, & |t| \le T \\ 0, & \textit{elsewhere.} \end{cases} \tag{2.29}$$

These pulse shapes are more and more band-limited by increasing N because the truncated energy outside the interval $[-T, +T]$ is a rapidly decreasing function of N. This can be seen by noting that the unlimited pulse shape $(\sin\pi t/T)/(\pi t/T)$ is strictly band-limited.

The power spectral density of the QPOM signal using some of these pulse shapes is shown in Fig. 2.5. As seen from the figure, good spectral properties are obtained with this kind of pulse shapes. Also by increasing N, very low side lobes are obtained.

The use of overlapping pulse shapes introduces ISI into the transmitted signal. This ISI affects the optimum sampling at the receiver, and therefore, degrades the performance of QPOM signals. The evaluation of error probability in the presence of inter-symbol interference plays a fundamental role in digital transmission systems, particularly in baseband systems where the effect of ISI may be particularly strong.

Several authors have investigated the performance of transmitted signals affected by ISI. Maximum likelihood decoding of these signals has been considered in [20, 21]. However, the complexity of this detector increases exponentially with the length of the message. Forney [21] has introduced a technique in which the received signal is

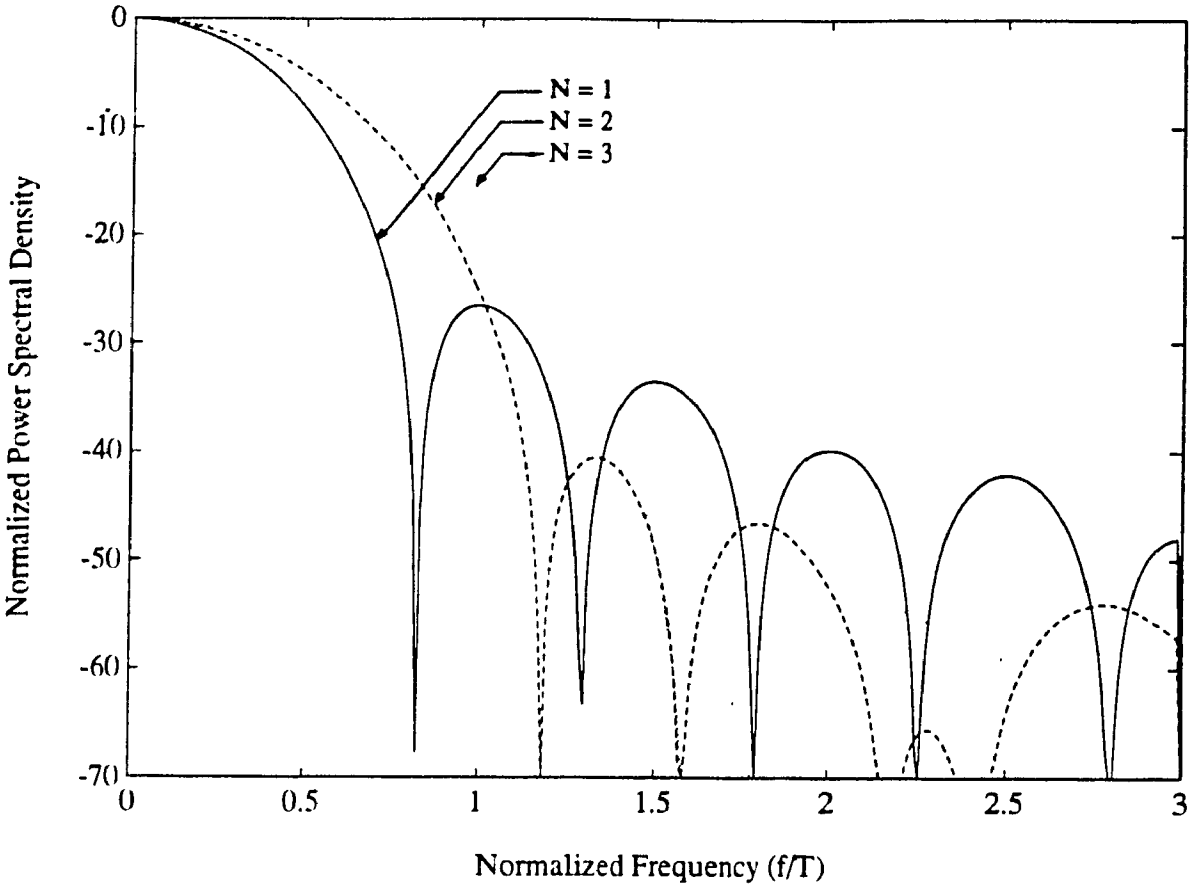

Fig. 2.5 – Normalized power spectral density of QPOM signals, double-interval pulse $p(t) = (sinc(\pi t/2T))^N$

processed by a recursive structure using the Viterbi algorithm, but the implementation of such a receiver was thought of as complex and too expensive. Instead other techniques were used such as linear or non-linear transversal equalizers, and raised-cosine-type receivers. These techniques showed that it is possible to improve the performance of QPOM signals with less complexity. However, the improvement was not enough to attain the performance of ideal coherent QPSK signals. For example, in [19] the performance degradation with respect to ideal coherent QPSK was reduced to 0.4 dB using a raised-cosine-type filter with a roll-off factor of 0.4.

So far we have seen that power and bandwidth efficient schemes can be obtained using double-interval overlapping pulse shapes. The efficiency is obtained without increasing the complexity of the modulator, but at the expense of a performance degradation. Therefore, a more efficient detection scheme is needed to make QPOM schemes more suitable. Furthermore, the envelope of the modulated signal is not constant. Constant envelope may be an additional desirable feature for certain nonlinear type of channels. For instance, the Traveling Wave Tube (TWT) amplifier in a satellite repeater usually converts amplitude variations to spurious phase modulation. A constant envelope for the modulated signal may reduce this problem to a great extent [3]. Also, if there is nonlinearity in the channel due to the presence of class-C, solid state-power amplifiers, constant envelope may be an additional desirable feature. It is possible to insert a hard-limiter at the output of the QPOM scheme without significantly spreading the processed signal. Thus at the output of the hard-limiter, the transmitted signal will have a constant envelope.

2.3.1. Constant Envelope QPOM Signals

To maximize the power efficiency, the High Power Amplifier (HPA) has to operate in a nonlinear mode. Consider the QPOM scheme followed by a saturated HPA shown in Fig. 2.6. The saturated HPA may be modeled as an ideal hard-limiter that produces a

constant envelope and no change to the phase of the QPOM transmitted signal [32]. The transfer function characteristic of the ideal hard-limiter is shown in Fig. 2.7. Such a model closely approximates the Gunn and Impact diode injection looked amplifiers and is a reasonable first order approximation of saturated HPAs in general [32].

The hard-limited QPOM signal $z(t)$ can be represented as [4]:

$$z(t) = z_I(t)cos\,2\pi f_c t + z_Q(t)sin\,2\pi f_c t$$

$$= cos(2\pi f_c t + \phi_z(t)), \tag{2.30}$$

where $z_I(t)$ and $z_Q(t)$ are in-phase and quadrature equivalent baseband components of the hard-limited QPOM signal with

$$z_I^2(t) + z_Q^2(t) = 1$$

and

$$\phi_z(t) = -\tan^{-1}\left[\frac{z_I(t)}{z_Q(t)}\right].$$

It is easy to verify that

$$z_I(t) = \frac{s_I(t)}{\left[s_I^2(t) + s_Q^2(t)\right]^{1/2}} \tag{2.31a}$$

and

$$z_Q(t) = \frac{s_Q(t)}{\left[s_I^2(t) + s_Q^2(t)\right]^{1/2}} \tag{2.31b}$$

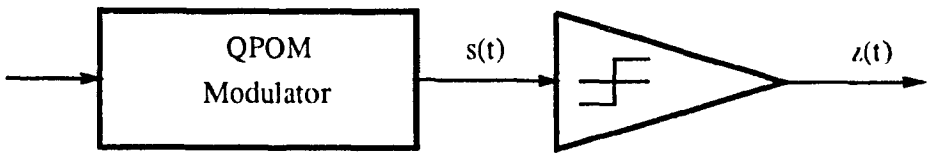

Fig. 2.6 - Block diagram of a QPOM modulator followed by a hard-limiter.

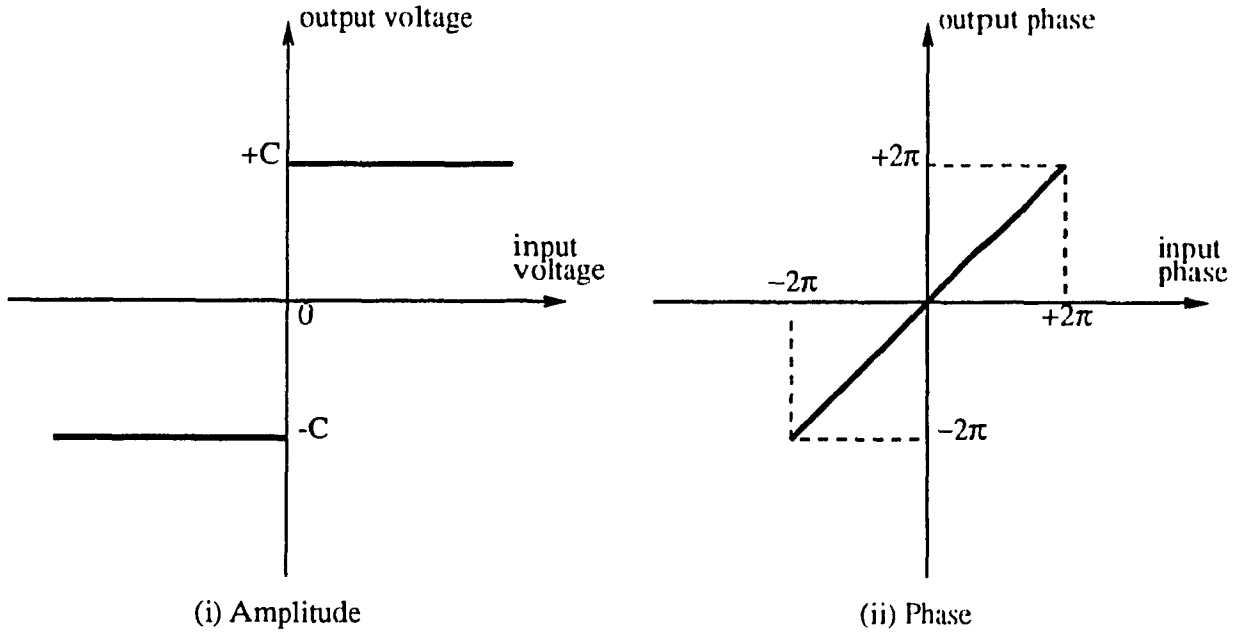

(i) Amplitude (ii) Phase

Fig. 2.7 - Transfer characteristics of an ideal hard-limiter.

where

$$s_I(t) = \sum_{n=-\infty}^{+\infty} A_n p(t - nT)$$

and

$$s_Q(t) = \sum_{n=-\infty}^{+\infty} B_n p(t - nT).$$

We notice that the two components of the transmitted signal are no longer independent, and any change in $s_I(t)$ (or $s_Q(t)$) will affect both components. This has as effect to introduce more ISI into the QPOM signal.

The power spectral density of this type of signals has been studied in the literature and different techniques have been used [1-31]. In [1] a finite-state Markov chain model was used to calculate the power spectral density of hard-limited QPOM signals. These studies showed that the spectral regrowth of hard-limited QPOM signals depends on the time offset T_d. It was shown that the spectral regrowth is minimum when $T_d = T/2$.

As an illustrative example, we consider the spectral regrowth of hard-limited QPOM signals having the double-interval pulse shape $p_1(t)$. The results of Fig. 2.8 confirm the above statement, and indicate that the minimum spectral regrowth is obtained at $T_d = T/2$. The modulation scheme with $T_d = T/2$ is called IJF-OQPSK [1].

The eye diagrams of the equivalent baseband components of the hard-limited QPOM signal with different values of T_d are shown in Fig. 2.9. We notice that the signal contains ISI and jitter, and this interference effect increases with the time delay T_d. It is maximum (3 dB peak-to-peak) at $T_d = T/2$ and zero at $T_d = 0$. This interference affects the P_e performance of the QPOM signal.

The results of Fig. 2.10 indicate that the hard-limited Offset-QPOM signal has more

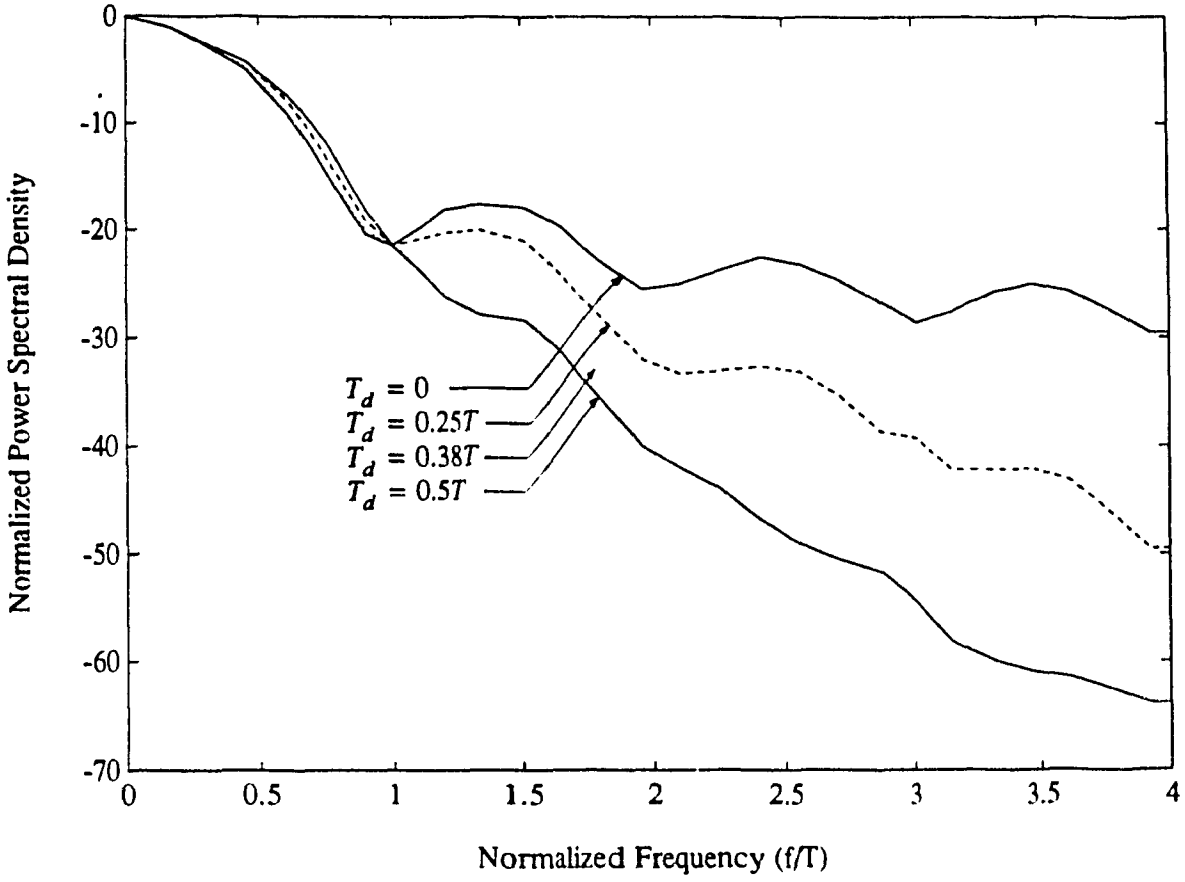

Fig. 2.8 – Power spectra of hard-limited QPOM signals with different values of T_d (for $p(t) = 0.5(1 + \cos\pi t/T)$)

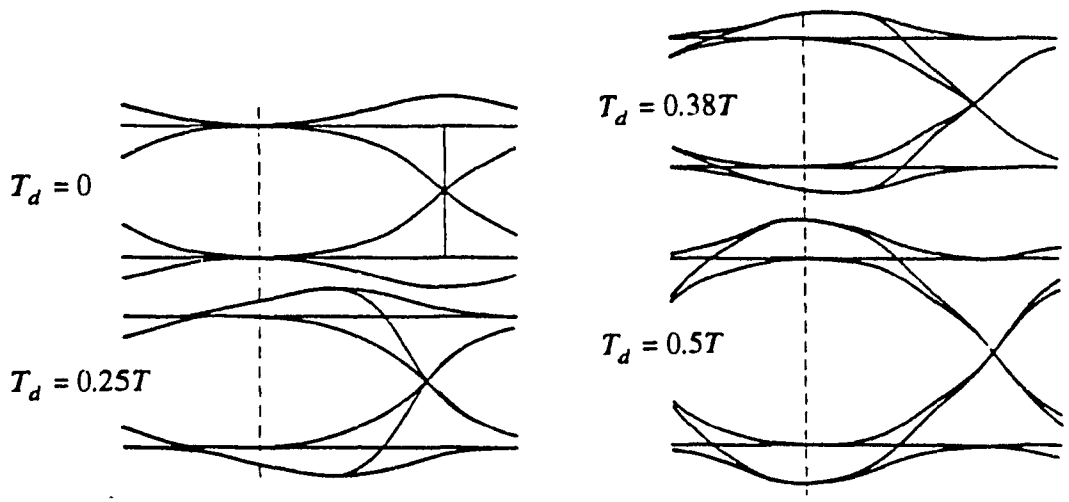

Fig. 2.9 – Eye diagrams of the demodulated baseband components of hard-limited QPOM signals

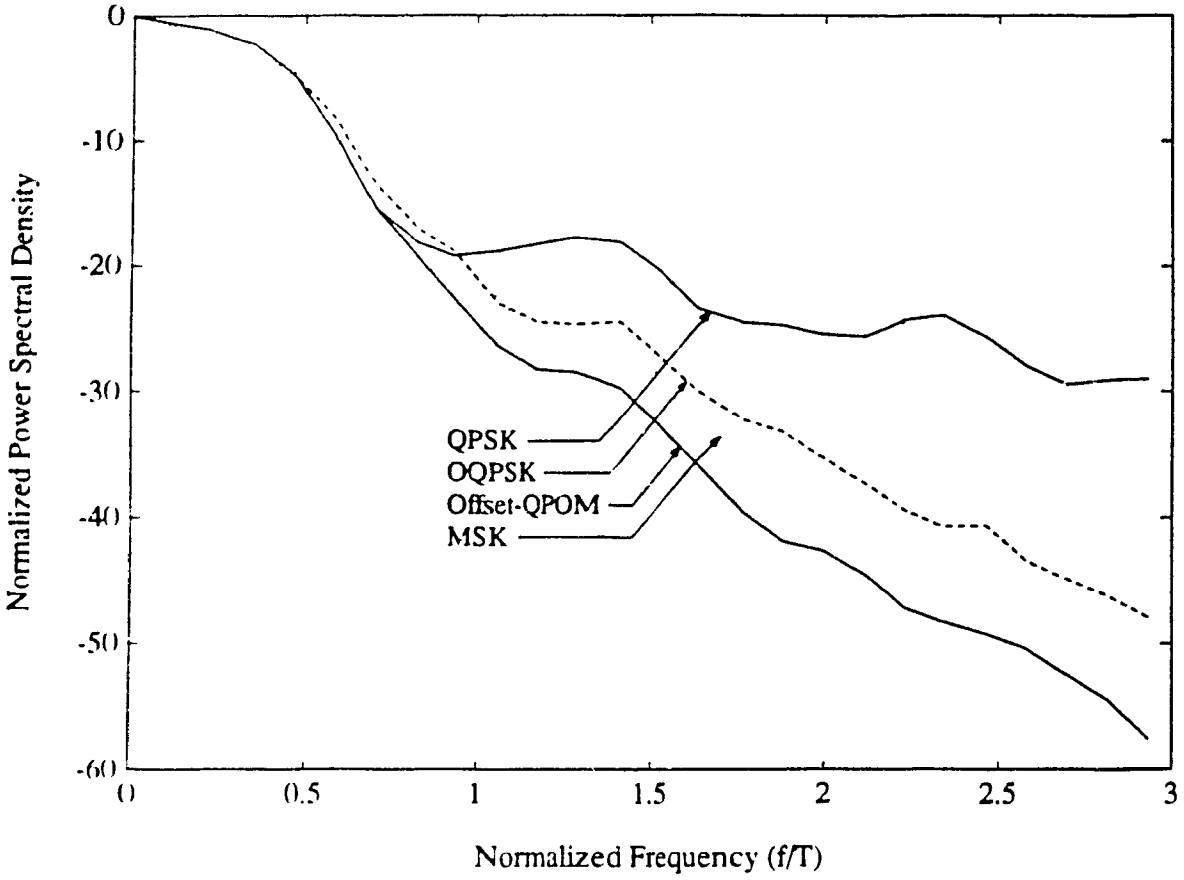

Fig. 2.10 – Comparison of power spectra of hardlimited QPSK, OQPSK and QPOM signals

significant spectral advantages than the hard-limited QPSK, Offset-QPSK, and MSK signals. Hard-limited QPOM signal has a constant envelope. Comparing its power spectral density to those of some other constant envelope modulated signals such as TFM [15, 16] and GMSK [14] indicates that for the frequency region within the bit rate frequency, the hard-limited Offset-QPOM with the pulse shape $p_0(t)$ has a more compact spectrum.

The performance of hard-limited QPOM schemes has been studied in the literature [25, 36, 37]. It was shown that in a hard-limited signal-channel model, the QPOM ($T_d = 0$) scheme outperforms the Offset-QPOM ($T_d = T/2$) scheme. This is explained by the fact that the sampling instants of the baseband components of the hard-limited QPOM have less intersymbol interference than those of the hard-limited Offset-QPOM due to the in-phase-to-quadrature crosstalk (see the eye diagram of Fig. 2.9).

For its spectral advantages over many modulation techniques and its ease of implementation, the QPOM scheme is very attractive. However, a more efficient detector is needed to make the QPOM scheme suitable to mobile satellite communication channels. That is a major motivation behind the investigation of the performance of QPOM signals in this dissertation.

2.4. QUADRATURE-QUADRATURE PHASE SHIFT KEYING

Quadrature-Quadrature Phase Shift Keying (Q^2PSK) is a form of direct quadrature modulation. This modulation scheme was designed based on a 4-dimensional signal space, thus increasing its bandwidth efficiency by a factor of two over two dimensional schemes such as QPSK and MSK [18].

A Q^2PSK transmitted signal can be written as:

$$s(t) = \sum_{n=-\infty}^{+\infty} A_n s_1(t) + B_n s_2(t) + C_n s_3(t) + D_n s_4(t), \tag{2.32}$$

where A_n, B_n, C_n, and D_n are antipodal data taking the values ± 1 with equal probability of 1/2. The signals $\{s_i(t), i = 1, 2, 3, 4\}$ are defined over the interval $[-T_b, +T_b]$ and are given by

$$s_1(t) = cos(\pi t/2T_b)cos\,2\pi f_c t \tag{2.33a}$$

$$s_2(t) = sin(\pi t/2T_b)cos\,2\pi f_c t \tag{2.33b}$$

$$s_3(t) = cos(\pi t/2T_b)sin\,2\pi f_c t \tag{2.33c}$$

$$s_4(t) = sin(\pi t/2T_b)sin\,2\pi f_c t, \tag{2.33d}$$

and identify $p_1(t) = cos(\pi t/2T_b)$ and $p_2(t) = sin(\pi t/2T_b)$ as two double interval pulse shapes. The signals $\{s_i(t)\}$ form a set of four equal-energy orthogonal signals under the restriction

$$f_c = n/4T_b, \quad n = \text{integer} \geq 2.$$

The dimensionality of the signal set used in this scheme is four, two of them come from the orthogonality of the carriers, the remaining two from the orthogonality of the two pulse shapes $p_1(t)$ and $p_2(t)$. Two carriers and two data shaping pulses are pairwise quadrature in-phase, where the name quadrature-quadrature PSK [18].

From (2.32), we notice that Q^2PSK signals can be written as the sum of two MSK signals. Therefore, this modulation scheme can also be seen as two MSK modulators in parallel which explains more its bandwidth efficiency. The power spectral density of this scheme is illustrated in Fig. 2.11. It is observed that its main lobe is the narrowest compared to conventional QPSK and MSK. In Chapter 6, we will study the performance of a modulation scheme designed in a manner similar to the Q^2PSK. This modulation scheme is considered as two QPOM schemes in parallel and uses two non-linear HPAs to increase its power efficiency.

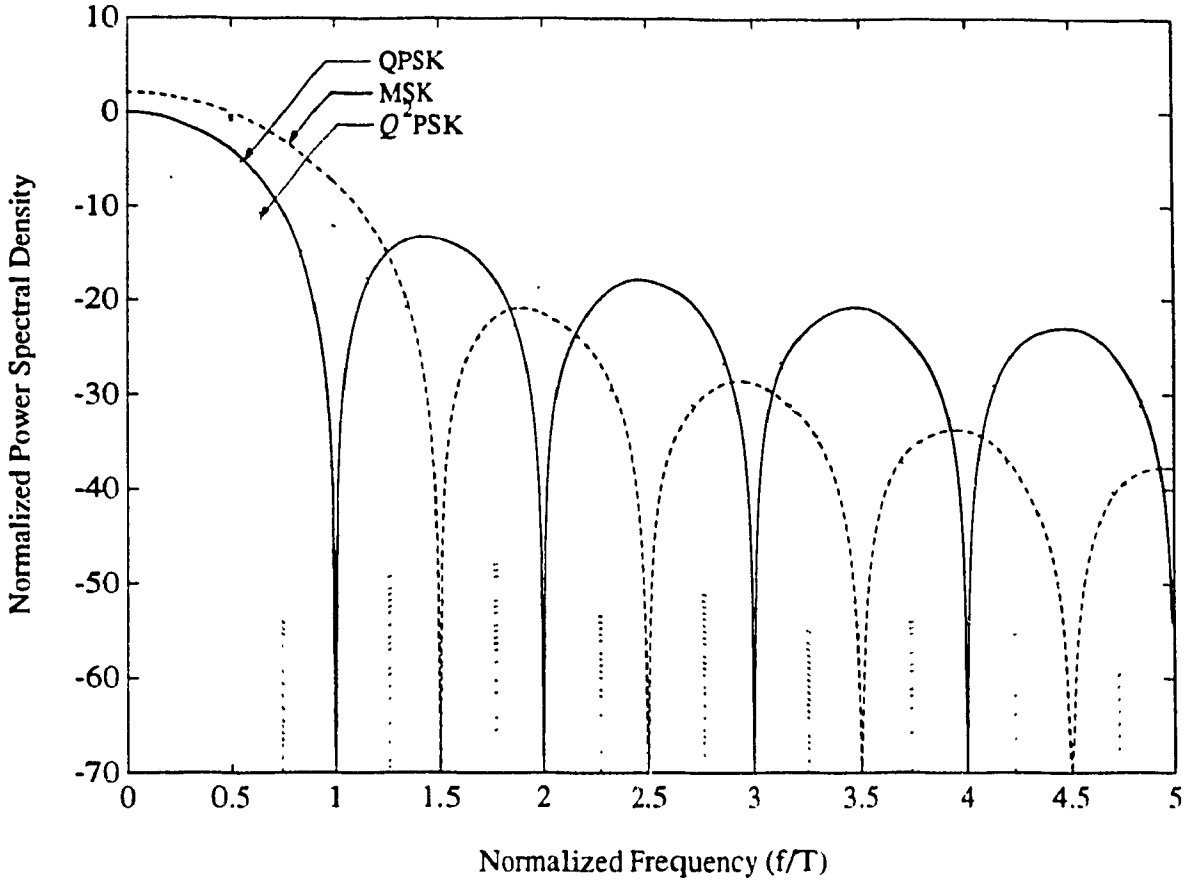

Fig. 2.11 – Normalized power spectral densities of QPSK, MSK, and Q^2PSK modulated signals.

2.5. DISCUSSION

Power and bandwidth efficient modulated signals can be generated using direct quadrature modulation schemes. The transmitted signal is modulated in baseband and then up converted to the carrier frequency. This configuration helps us to reduce both the cost and the size of the modulation scheme. Spectral shaping is achieved using only double-interval overlapping pulses. Thus, avoiding the use of longer pulse shapes.

The use of these overlapping pulse shapes introduces memory into the transmitted signal. This memory reduces the Euclidean distance between signal points and causes a degradation in performance in the case of independent symbol-by-symbol detection.

When the signal is transmitted over AWGN channels, the Euclidean distance is the main parameter which affects the performance. Therefore, the performance can be improved by removing the effect of this memory (using equalization) or by exploiting it in the benefit of the detection scheme (using maximum likelihood sequence estimation). One way or the other, the obtained Euclidean distance will always be less or equal to the Euclidean distance of the interference free signal. The MLSE receiver is an optimum scheme and can exploit the memory affectively especially when this memory is well defined.

Consider for example the in-phase component of a QPOM transmitted signal,

$$s_I(t) = \sum_{n=-\infty}^{+\infty} A_n p(t - nT).$$

Over one symbol interval $[nT, (n + 1)T]$, the signal $s_I(t)$ can be rewritten as

$$s_I(t) = A_n p(t - nT) + A_{n-1} p(t - (n - 1)T)$$

$$A_n = 2a_n - 1.$$

As we can see this signal is a function of both a_n and a_{n-1}. For each combination of this pair of bits, $s_I(t)$ is represented by a different single interval pulse. If these pulses are defined at the receiver, then no intersymbol interference will be present and an optimum MLSE receiver can be implemented. Furthermore, this memory can be represented in a form which can be used affectively by the receiver [38].

In the following chapters, we introduce a technique in improving the performance of Quadrature Pulse-Overlapping Modulated (QPOM) signals. This technique exploits the memory introduced by the overlapping pulse shape. For fading channels, the receiver gets a maximum use of the time diversity that can be provided by the structure of the modulation scheme.

CHAPTER III

PERFORMANCE OF QUADRATURE PULSE-OVERLAPPING MODULATED SIGNALS IN AWGN CHANNELS

This Chapter treats the performance of Quadrature Pulse-Overlapping Modulated (QPOM) signals in Additive White Gaussian Noise (AWGN) channels. The QPOM scheme is first decomposed into a linear encoder followed by a memoryless modulator. The trellis diagram representing this inherent non-redundant coding structure is then used to construct its Maximum Likelihood Sequence Estimation (MLSE) receiver. We will derive an upper bound on the average bit error probability for the QPOM scheme and discuss the effect of the overlapping pulse shape and nonlinear channels on the performance of the system. Computer simulation results are then given to verify the analytical results.

3.1. LINEAR QPOM SCHEMES

Consider the block diagram of the QPOM scheme shown in Fig. 2.2. The transmitted signal $s(t)$ is given by

$$s(t) = s_I(t)\cos 2\pi f_c t + s_Q(t)\sin 2\pi f_c t, \tag{3.1}$$

where

$$s_I(t) = \sum_{n=-\infty}^{+\infty} A_n p(t - nT)$$

$$s_Q(t) = \sum_{n=-\infty}^{+\infty} B_n p(t - nT)$$

are the in-phase and quadrature components of $s(t)$.

Over one symbol interval $nT \le t \le (n+1)T$, the two components can be rewritten as:

$$s_I(t) = A_n p(t - nT) + A_{n-1} p(t - (n-1)T) \tag{3.2a}$$

$$s_Q(t) = B_n p(t - nT) + B_{n-1} p(t - (n-1)T). \tag{3.2b}$$

It is observed that at each symbol interval, the in-phase component $s_I(t)$ is a function of $\{a_n, a_{n-1}\}$, and the quadrature component $s_Q(t)$ is a function of $\{b_n, b_{n-1}\}$. As $\{a_n\}$ and $\{b_n\}$ are statistically independent, $s_I(t)$ and $s_Q(t)$ are also independent.

The two components $s_I(t)$ and $s_Q(t)$ take one of four possible elements

$$s_0(\tau) = p(\tau) + p(\tau - T) \tag{3.3a}$$

$$s_1(\tau) = p(\tau) - p(\tau - T) \tag{3.3b}$$

$$s_2(\tau) = -s_1(\tau) \tag{3.3c}$$

$$s_3(\tau) = -s_0(\tau) \tag{3.3d}$$

where $0 \le \tau \le T$ and $\tau = t - nT$.

The above equations indicate that for each set of bits $\{a_n, b_n, a_{n-1}, b_{n-1}\}$, a pair of waveforms $(s_I(t), s_Q(t))$ is transmitted. Furthermore, these waveforms are generated independently one from the other. Therefore, it is possible to model the QPOM scheme by a different block diagram as shown in Fig. 3.1. The two blocks B_I and B_Q resemble a convolutional encoder represented by the trellis diagram shown in Fig. 3.2a. The states of this trellis diagram are represented by the contents of the shift registers of the encoder, and all possible outputs by the set $\mathbf{A} = \{0, 1, 2, 3\}$. This set is partitioned into two subsets $\mathbf{A}_0 = \{0, 2\}$ and $\mathbf{A}_1 = \{1, 3\}$. The output of the encoder is mapped into a single-interval

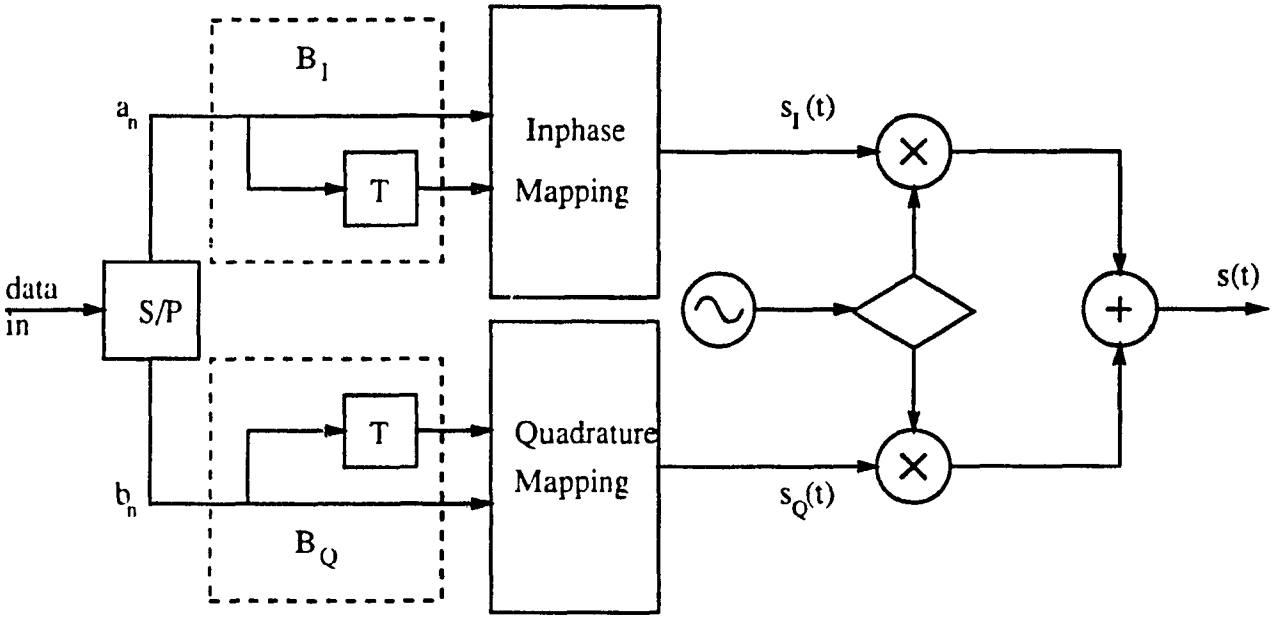

Fig. 3.1 - The new configuration of the linear QPOM scheme.

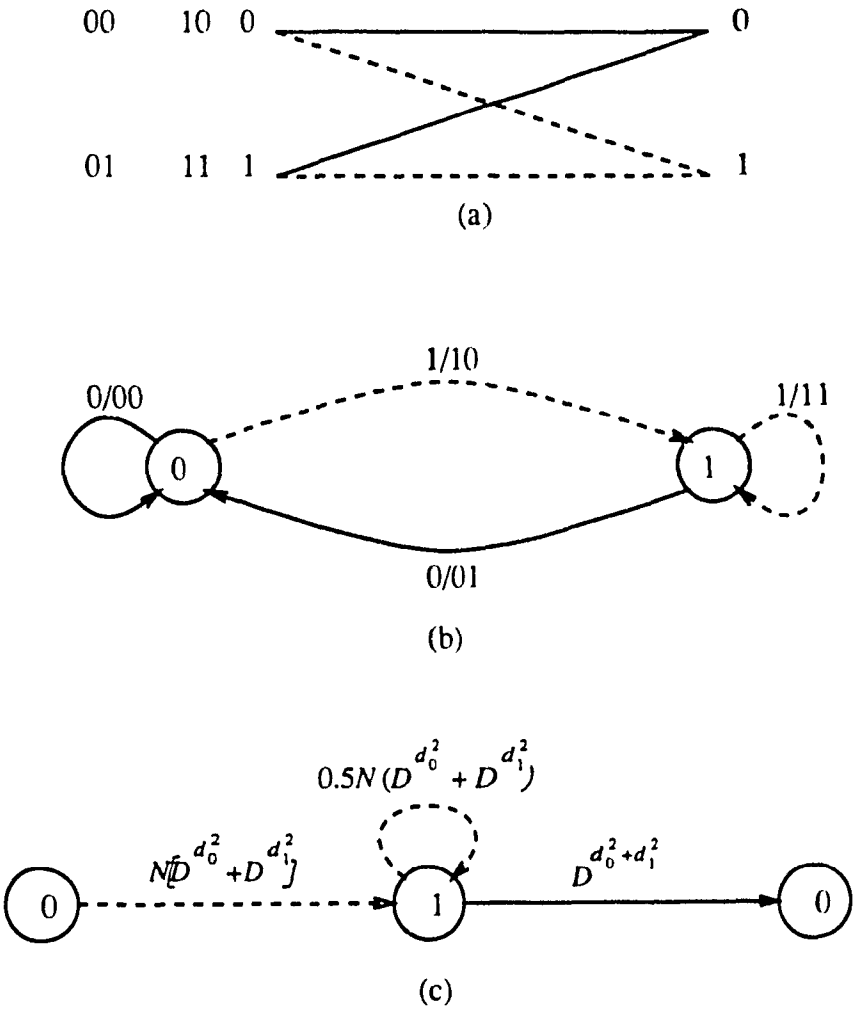

Fig. 3.2 - The linear encoder of the inphase (quadrature) component of the linear QPOM scheme.
(a) trellis diagram, (b) state diagram, (c) modified state diagram.

waveform based on the mapping rules of Table 3.1.

As we can see the memory of the linear QPOM scheme is well defined and can be appropriately used at the receiver. Therefore, based on this model a maximum likelihood sequence estimation receiver can be used to demodulate the transmitted signal. Furthermore, given that $s_I(\tau)$ and $s_Q(\tau)$ are statistically independent, the receiver can treat each component independently from the other without affecting the performance of the overall system.

Table 3.1
Channel Signal Mapping for the Components of the Linear QPOM Scheme

Mapper input	Mapper output
00	$-s_0(\tau)$
01	$-s_1(\tau)$
10	$+s_1(\tau)$
11	$+s_0(\tau)$

A convenient way to represent the set of signals $\{s_i(\tau), i = 0, \ldots, 3\}$ is to use a set of J orthonormal waveforms, with the jth waveform denoted by $\phi_j(\tau)$. Thus the signal $s_i(\tau)$ can be written as

$$s_i(\tau) = \sum_{j=0}^{J-1} s_{ij}\phi_j(\tau), \quad i = 0, \ldots, 3, \tag{3.4}$$

where

$$\int_0^T \phi_j(\tau)\phi_l(\tau)d\tau = \begin{cases} 1 & j = l \\ 0 & j \neq l. \end{cases} \tag{3.5}$$

This representation is useful for the error probability analysis where the performance will depend only on the coefficient $\{s_{ij}\}$ and the power spectral density of the noise and will

be completely independent of the actual waveforms chosen for the set $\{\phi_j(\tau)\}$.

For the set of signals $\{s_i(\tau)\}$, we notice that

$$\int_0^T s_0(t)s_1(t)dt = \int_0^T (p^2(t) - p^2(t-T))dt = 0. \tag{3.6}$$

This means that $s_0(\tau)$ and $s_1(\tau)$ are orthogonal. Note that $s_2(\tau)$ and $s_3(\tau)$ are antipodal signals to $s_0(\tau)$ and $s_1(\tau)$, respectively. Hence, a 2-dimensional orthonormal basis $(\phi_0(\tau), \phi_1(\tau))$ can be used to represent the *four* signals of Eq. (3.3). This orthonormal basis is easily obtained from $s_0(\tau)$ and $s_1(\tau)$ as:

$$\phi_0(\tau) = \frac{s_0(\tau)}{\sqrt{E_0}}, \qquad E_0 = \int_0^T s_0^2(\tau)d\tau \tag{3.7}$$

$$\phi_1(\tau) = \frac{s_1(\tau)}{\sqrt{E_1}}, \qquad E_1 = \int_0^T s_1^2(\tau)d\tau, \tag{3.8}$$

where E_i is the energy of the waveform $s_i(\tau)$. The energy E_i can be expressed in terms of the bit energy E_b as follows;

$$E_0 = (1+\gamma)E_b \tag{3.9}$$

$$E_1 = (1-\gamma)E_b, \tag{3.10}$$

where γ is a coefficient depending on the double-interval overlapping pulse shape $p(t)$ and is given by

$$\gamma = \frac{2}{E_b}\int_0^T p(t)p(t-T)dt. \tag{3.11}$$

Once an orthonormal basis $\{\phi_j(\tau)\}$ has been adopted, each waveform $\{s_i(\tau), i = 0, \ldots, 3\}$ is completely determined by the vector of its coefficients in the signal space $(\phi_0(\tau), \phi_1(\tau))$. This vector is a 2-element vector defined as;

$$\underline{s}_i = (s_{i0}, s_{i1}), \tag{3.12}$$

where

$$s_{ij} = \int_0^T s_i(\tau)\phi_j(\tau)d\tau, \qquad j = 0, 1.$$

The vector $\underline{s}_i$ can be seen as a point in a 2-dimensional geometric space, called signal space, with 2 perpendicular axes labeled ϕ_0, ϕ_1 or s_0, s_1 as shown in Fig. 3.3. The choice of the set $\{\phi_i(\tau)\}$ depends on the actual signals $\{s_i(\tau)\}$.

The transmitted QPOM signal is now well defined by two vectors, one vector representing the in-phase component and the other representing the quadrature component.

3.1.1. MLSE Receiver for Linear QPOM Signals

So far we have considered the representation of the signal waveforms $\{s_i(\tau)\}$ by the corresponding signal vectors $\{\underline{s}_i\}$. It is also straightforward to recover the vectors from the waveforms. Fig. 3.4a shows the block diagram of the QPOM system in an AWGN channel. The MLSE receiver structure for QPOM signals is shown in Fig. 3.4b. Consider a noise-free environment, the received signal $r(t)$ first passes through the coherent quadrature demodulator which produces the in-phase and quadrature components $s_I(t)$ and $s_Q(t)$, where ideal coherent detection is assumed. The two components are then converted into the vectors $\underline{s}_I$ and $\underline{s}_Q$, respectively, by a bank of two matched filters with impulse responses $\{\phi_i(T - t)\}$. Each vector is then used by a Viterbi processor to

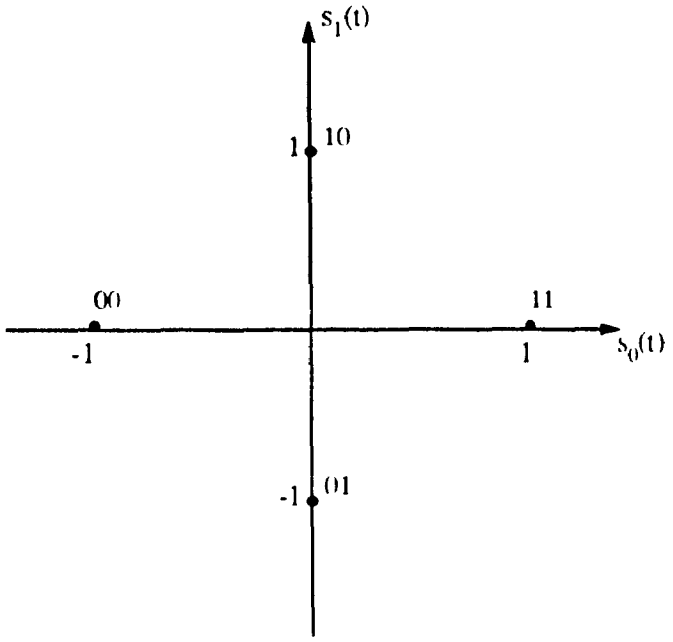

Fig. 3.3 - Signal constellations of the inphase (quadrature) component of the linear QPOM scheme.

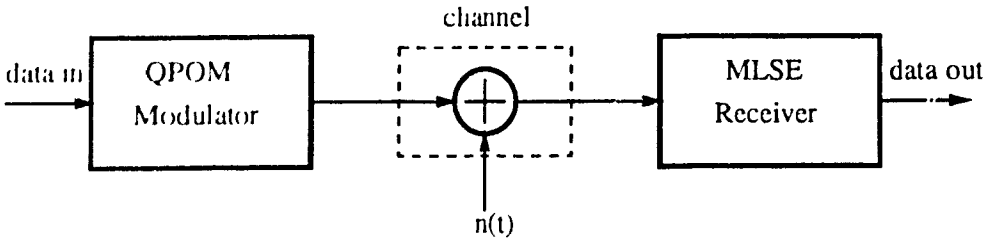

Fig. 3.4a - The block diagram of a QPOM system in an AWGN channel

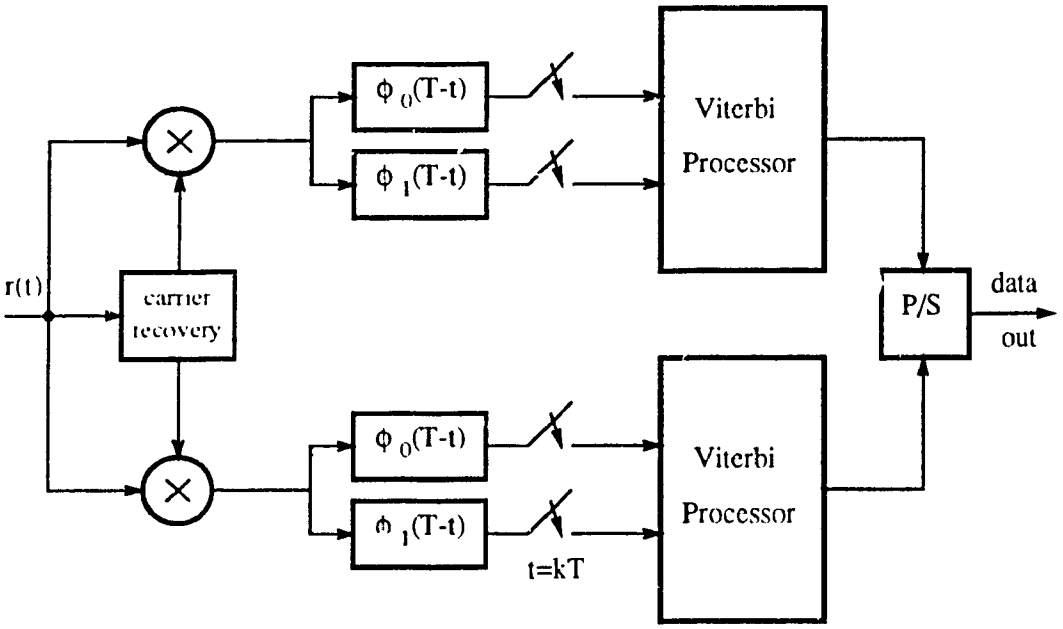

Fig. 3.4b - The MLSE receiver of linear QPOM signals.

reconstruct the error free transmitted data. The operation of the Viterbi processor is based on the trellis diagram of the QPOM encoder and the mapping rules of Table 3.1. A serial-to-parallel device is then used to reconstruct the original data.

Now consider the case when the signal $s(t)$ is transmitted over the Additive White Gaussian Noise (AWGN) channel, the received signal can be written as:

$$r(t) = s(t) + n(t), \tag{3.13}$$

where $n(t)$ is the band pass AWGN process represented by

$$n(t) = n_c(t)cos\,2\pi f_c t + n_s(t)sin\,2\pi f_c t, \tag{3.14}$$

and $n_c(t)$ and $n_s(t)$ are independent, identically distributed (i.i.d) Gaussian random processes with zero-mean and a variance of $N_0/2$. The received signal can be rewritten as:

$$r(t) = \left[s_I(t) + n_c(t)\right]\cos 2\pi f_c t + \left[s_Q(t) + n_s(t)\right]\sin 2\pi f_c t \tag{3.15}$$

The first task of an optimum receiver will be to extract the pair of waveforms $(s_I(t), s_Q(t))$, which can be done by down-converting the received signal to baseband. However, due to the noise introduced by the channel, the obtained pair of waveforms becomes $(r_I(t), r_Q(t))$, where

$$r_I(t) = s_I(t) + n_c(t) \tag{3.16a}$$

$$r_Q(t) = s_Q(t) + n_s(t). \tag{3.16b}$$

Since the two components $s_I(t)$ and $s_Q(t)$ are statistically independent, $r_I(t)$ and $r_Q(t)$ are also statistically independent. Passed through the bank of matched filters, these components are converted into $\underline{r}_I$ and $\underline{r}_Q$, respectively, where

$$\underline{r}_I = \underline{s}_I + \underline{n}_I, \tag{3.17}$$

$$\underline{r}_Q = \underline{s}_Q + \underline{n}_Q. \tag{3.18}$$

The elements of the vector $\underline{n}_I$ ($\underline{n}_Q$) are i.i.d zero-mean Gaussian random variables with variance $N_0/2$, and the vectors $\underline{s}_I$ and $\underline{s}_Q$ take the form of (3.12). Each vector is then passed through a Viterbi processor which performs maximum likelihood sequence estimation based on the trellis structure of the encoder and the mapping rules of Table 3.1. The output of the decoder is taken as the estimate of the transmitted data.

Consider the case of maximum likelihood sequence estimation, where each one of N possible data sequences corresponds to transmitting a distinct signal, with each distinct signal represented by a discrete J-element vector. The set of possible transmitted signals can be denoted as the sequence of N-vectors

$$\mathbf{s} = \{\underline{s}_0, \underline{s}_1, \ldots, \underline{s}_{N-1}\}. \tag{3.19}$$

The corresponding signal at the output of the discrete time channel is denoted by the sequence of N-vectors $\mathbf{r}$,

$$\mathbf{r} = \{\underline{r}_0, \underline{r}_1, \ldots, \underline{r}_{N-1}\}. \tag{3.20}$$

Then the choice of the MLSE receiver is the set of signals for which the a posteriori probability $P\{\mathbf{r} \mid \mathbf{s}\}$ is the largest [27]. When all the signals are transmitted with equal probability, this is equivalent to choosing the set of signals which maximizes the conditional probability density function (p.d.f)

$$p(\mathbf{r} \mid \mathbf{s}) = \prod_{n=0}^{N-1} p(\underline{r}_n \mid \underline{s}_n), \tag{3.21}$$

where $p(\underline{r}_n \mid \underline{s}_n)$ is the conditional probability density function of the vector $\underline{r}_n$ given the vector $\underline{s}_n$ is transmitted. For a given $\underline{s}_n$, the elements of the received vector are i.i.d

Gáussian random variables with mean s_{ni} and variance $N_0/2$, i.e.,

$$p(\underline{r}_n \mid \underline{s}_n) = \frac{1}{\left(\pi N_0\right)^{N/2}} \exp\left[\frac{-\| \underline{r}_n - \underline{s}_n \|^2}{N_0}\right]. \tag{3.22}$$

By combining the last two equations and then taking the natural log of the resulting equation, the maximum likelihood decoder is equivalent to one which selects the set of vectors for which the following metric

$$m(\mathbf{r}, \mathbf{s}) = -\sum_{n=0}^{N-1} \| \underline{r}_n - \underline{s}_n \|^2$$

is maximum.

3.1.2. Performance Analysis

Although exact derivation of the minimum attainable error probability is difficult, it is relatively easy to obtain a useful upper bound. To derive the upper bound on the average bit error probability of this detection scheme, we use a union bound similar to that used for upper-bounding the performance of convolutional codes [24]. The upper bound on P_b is the sum of all weighted pairwise error probabilities. The pairwise error probability denoted as $P\{\mathbf{s} \rightarrow \hat{\mathbf{s}}\}$ represents the probability of choosing the sequence of vectors $\hat{\mathbf{s}} = \{\underline{\hat{s}}_0, \underline{\hat{s}}_1, \ldots, \underline{\hat{s}}_{N-1}\}$ instead of the transmitted sequence of vectors $\mathbf{s} = \{\underline{s}_0, \underline{s}_1, \ldots, \underline{s}_{N-1}\}$. The MLSE decoder will decide in favor of $\hat{\mathbf{s}}$ if and only if:

$$m(\mathbf{r}, \hat{\mathbf{s}}) \geq m(\mathbf{r}, \mathbf{s}).$$

Hence, the pairwise error probability can be written as:

$$P(\mathbf{s} \rightarrow \hat{\mathbf{s}}) = P\left[\sum_{n=0}^{N-1} (\| \underline{r}_n - \underline{s}_n \|^2 - \| \underline{r}_n - \underline{\hat{s}}_n \|^2) \geq 0\right]$$

$$= P\left[\sum_{n=0}^{N-1} y_n \geq 0\right], \tag{3.23}$$

and y_n is a random variable defined as

$$y_n = \| \underline{r}_n - \underline{s}_n \|^2 - \| \underline{r}_n - \underline{\hat{s}}_n \|^2.$$

The random variable y_n can be rewritten as:

$$y_n = \sum_{i=0}^{J-1} \left[2n_i(\hat{s}_{ni} - s_{ni}) - (\hat{s}_{ni} - s_{ni})^2 \right]$$

$$= 2\sum_{i=0}^{J-1} n_i(\hat{s}_{ni} - s_{ni}) - \| \underline{\hat{s}}_n - \underline{s}_n \|^2, \tag{3.24}$$

where $\hat{s}_{ni}$ is the ith element of the vector $\underline{\hat{s}}_n$ and s_{ni} is the ith element of the vector $\underline{s}_n$. Since the components $\{n_i, i = 0, \ldots, N-1\}$ are i.i.d Gaussian random variables, then the process y_n is a Gaussian random variable with mean

$$\mu_{y_n} = - \| \underline{\hat{s}}_n - \underline{s}_n \|^2,$$

and variance

$$\sigma^2_{y_n} = 2N_0 \| \underline{\hat{s}}_n - \underline{s}_n \|^2.$$

Consequently, the process $\sum_{n=0}^{N-1} y_n$ is also Gaussian random variable with mean

$$\mu = - \sum_{n=0}^{N-1} \| \underline{\hat{s}}_n - \underline{s}_n \|^2,$$

and variance

$$\sigma^2 = 2N_0 \sum_{n=0}^{N-1} \| \underline{\hat{s}}_n - \underline{s}_n \|^2.$$

Let us define the variable $D^2(\mathbf{s}, \hat{\mathbf{s}})$ as [29]:

$$D^2(\mathbf{s}, \hat{\mathbf{s}}) = \sum_{n=0}^{N-1} \| \underline{\hat{s}}_n - \underline{s}_n \|^2. \tag{3.25}$$

It is easy to see that $D^2(\mathbf{s}, \hat{\mathbf{s}})$ represents the squared Euclidean distance between the two sequences s and ŝ. Therefore, The pairwise error probability can be rewritten as

$$P\{\mathbf{s} \to \hat{\mathbf{s}}\} = \frac{1}{2} erfc \left[\left[\frac{D^2(\mathbf{s}, \hat{\mathbf{s}})}{4N_0} \right]^{1/2} \right]$$

$$= \frac{1}{2} erfc \left[\left[\frac{d^2(\mathbf{s}, \hat{\mathbf{s}})}{4} \frac{E_b}{N_0} \right]^{1/2} \right], \tag{3.26}$$

where $d^2(\mathbf{s}, \hat{\mathbf{s}})$ is called the *normalized squared Euclidean distance* between the two sequences s and ŝ and defined as

$$d^2(\mathbf{s}, \hat{\mathbf{s}}) = \frac{1}{E_b} \sum_{n=0}^{N-1} \| \underline{\hat{s}}_n - \underline{s}_n \|^2. \tag{3.27}$$

From now on we will represent $d^2(\mathbf{s}, \hat{\mathbf{s}})$ by d^2 for the sake of simplicity.

For a given trellis diagram, there are many possible paths with different Euclidean distances from the correct path that merge with it at the same node. Therefore, an upper bound on the first-event error probability P_e is obtained by summing the error probability of Eq. (3.26) over all possible distances,

$$P_e \le \frac{1}{2} \sum_{d=d_{min}}^{+\infty} a_d erfc \left[\left[\frac{d^2}{4} \frac{E_b}{N_0} \right]^{1/2} \right], \tag{3.28}$$

where a_d denotes the number of paths having a distance d^2 from the correct path and merging with the correct path for the first time. The expression in (3.28) is an upper bound because the events which result in the pairwise error probabilities are not disjoint [24].

In order to find the average symbol error probability, the pairwise error probability needs to be multiplied by the number of uncorrectly decoded information symbols during that error event. By doing so, an upper bound on the average symbol error probability is given by:

$$P_s \le \frac{1}{2} \sum_{d=d_{\min}}^{+\infty} a_d v_d \, erfc\left[\left[\frac{d^2}{4}\frac{E_b}{N_0}\right]^{1/2}\right], \tag{3.29}$$

where v_d corresponds to the number of erroneous symbols associated with a specific error event. Consider the following inequality:

$$erfc(\sqrt{x+y}) \le erfc(\sqrt{x})\, e^{-y}, \quad x, y > 0, \tag{3.30}$$

and suppose that $x = d_{\min}^2 E_b/4N_0$ and $y = (d^2 - d_{\min}^2)E_b/4N_0$, then the upper bound on the average symbol error probability can be rewritten in the following form:

$$P_s \le \frac{1}{2} erfc\left[\left[\frac{d_{\min}^2}{4}\frac{E_b}{N_0}\right]^{1/2}\right] e^{d_{\min}^2 E_b/4N_0} \sum_{d=d_{\min}}^{+\infty} a_d v_d e^{-d^2 E_b/4N_0}, \tag{3.31}$$

where $d_{\min}^2$ represents the minimum normalized squared Euclidean distance of the QPOM encoder [24]. Eq. (3.31) can be expressed in terms of a function denoted by $T(D, N)$,

$$P_s \le \frac{1}{2} erfc\left[\left[\frac{d_{\min}^2}{4}\frac{E_b}{N_0}\right]^{1/2}\right] e^{d_{\min}^2 E_b/4N_0} \frac{\partial}{\partial N} T(D, N)\Big|_{\substack{D = e^{-E_b/4N_0} \\ N = 1}}, \tag{3.32}$$

where

$$T(D,N) = \sum_{d=d_{\min}}^{+\infty} a_d D^{d^2} N^{v_d} \tag{3.33}$$

represents the transfer function of the encoder [24]. This function describes the weight distribution, or the weight spectrum, of the incorrect paths and the number of symbol errors on these paths.

The upper bound on the average bit error probability is obtained by dividing Eq. (3.32) by k, where k is the number of bits in a transmitted symbol,

$$P_b \le \frac{1}{2k} erfc\left[\left[\frac{d_{\min}^2}{4}\frac{E_b}{N_0}\right]^{1/2}\right] e^{d_{\min}^2 E_b/4N_0} \frac{\partial}{\partial N} T(D,N)\Big|_{\substack{D = e^{-E_b/4N_0} \\ N = 1}} \tag{3.34}$$

The above equation represents a general form for the upper bound on the performance of a system with memory, where the memory has been identified by a linear encoder. In order to analyze the performance of a particular system, the transfer function need to be known or at least approximated.

3.1.3. Performance of Linear QPOM Signals

Consider the case of the linear QPOM scheme. Since the in-phase and quadrature components of the transmitted signal are statistically independent with equal probability, the probability of error of the system can be written as:

$$P_b = \frac{1}{2}(P_I + P_Q) = P_I = P_Q, \tag{3.35}$$

where P_I and P_Q represent the probability of error of the in-phase and quadrature components, respectively. In this case it is sufficient to consider only one component in analyzing the performance.

In general, coded modulation schemes are nonlinear and the assumption of transmitting the all-zero code word cannot be used in the evaluation of the error bound of Eq. (3.32). Instead, every possible code word should be considered as a transmitted one [41]. This requires an error evaluation algorithm which has a computational complexity increasing with $2^{2\nu}$, where ν is the memory length of the encoder.

According to [42], it is possible to reduce the computational complexity of the error bound if the encoder of the modulation scheme has a Uniform Euclidean Profile (UEP) property. In this case the error bound can be found with a computational complexity increasing with 2^{ν}, the same as linear convolutional codes. This approach can be applied to modulation schemes with the following properties:

1) The modulation scheme consists of a binary (linear) convolutional code followed by a memoryless modulator (mapper).

2) The weight profile of the signal subset $\mathbf{A}_i$ for a given error event $\mathbf{e}$ is not a function of the subset under consideration.

Consider the in-phase component $s_I(t)$. The trellis diagram of its linear encoder is shown in Fig. 3.2a. Now consider the signal set of the linear encoder $\mathbf{A} = \{0, 1, 2, 3\}$ and its two subsets $\mathbf{A}_0 = \{0, 2\}$ and $\mathbf{A}_1 = \{1, 3\}$. The weight profile of these subsets with respect to all possible values of the error event $\mathbf{e}$ can be obtained using the following expression [42]

$$F(\mathbf{A}_i, \mathbf{e}, D) = \sum a_\alpha D^\alpha, \tag{3.36}$$

where a_α is the number of channel signals in the subset $\mathbf{A}_i$ that have a square Euclidean distance α with respect to $\mathbf{e}$. The Euclidean weight α is defined as the squared Euclidean distance between $\mathbf{s} \in \mathbf{A}_i$ and $\mathbf{s} + \mathbf{s}_e$, where $\mathbf{s}_e$ is the channel signal corresponding to the error vector $\mathbf{e}$. Table 3.2 shows the results for both subsets $\mathbf{A}_0$ and $\mathbf{A}_1$. It is observed that these subsets have the same weight profiles with respect to $\mathbf{e}$. Therefore, the in-phase

component of the QPOM scheme satisfies both conditions, and the transfer function of the encoder can be obtained following the same procedure used in [42]. The modified state diagram is shown in Fig. 3.2c. Its branches are labeled as $(1/2^k)N^{v_d}F(\mathbf{A}_0, \mathbf{e}, D)$. The transfer function is now obtained by solving the state equations of this state diagram as outlined in [42], that is,

$$T(D,N) = \frac{X_o}{X_i}, \tag{3.37}$$

where

$$X_o = D^{d_0^2+d_1^2} X_1$$

$$X_1 = ND^{d_0^2+d_1^2} X_i + 0.5N(D^{4d_0^2} + D^{4d_1^2})X_1.$$

Solving these equations, the transfer function becomes:

$$T(D,N) = \frac{ND^{2(d_0^2+d_1^2)}}{1 - 0.5ND^{4d_0^2} - 0.5ND^{4d_1^2}}, \tag{3.38}$$

where

$$d_0^2 = \frac{1}{E_b} \int_0^T s_0^2(\tau)d\tau = 1 + \gamma$$

and

$$d_1^2 = \frac{1}{E_b} \int_0^T s_1^2(\tau)d\tau = 1 - \gamma$$

with

$$\gamma = \frac{2}{E_b} \int_0^T p(\tau)p(\tau - T)d\tau. \tag{3.39}$$

The minimum Euclidean distance of the code can be obtained from the transfer function as follows [43]:

$$d_{\min}^2 = \lim_{D \to 0} \frac{dT(D, N)/dD}{T(D, N)/D} \Big| N = 1 \quad = 4. \tag{3.40}$$

Taking the derivative of Eq. (3.38) and then combining it with Eq. (3.34), the upper bound on P_b for linear QPOM signals becomes:

$$P_b \le \frac{1}{2} erfc\left[\sqrt{E_b/N_0}\right] \frac{1}{\left[1 - 0.5e^{-(1+\gamma)E_b/N_0} - 0.5e^{-(1-\gamma)E_b/N_0}\right]^2}. \tag{3.41}$$

Table 3.2
Weight Profile of Subsets with Respect to **e**
for Linear QPOM Schemes

Subset of Channel Signal	**e**	Weight Profile
$\mathbf{A}_0$	00	2
$\mathbf{A}_0$	01	$2D^{d_0^2+d_1^2}$
$\mathbf{A}_0$	10	$2D^{d_0^2+d_1^2}$
$\mathbf{A}_0$	11	$D^{4d_0^2} + D^{4d_1^2}$
$\mathbf{A}_1$	00	2
$\mathbf{A}_1$	01	$2D^{d_0^2+d_1^2}$
$\mathbf{A}_1$	10	$2D^{d_0^2+d_1^2}$
$\mathbf{A}_1$	11	$D^{4d_0^2} + D^{4d_1^2}$

At high signal-to-noise ratio E_b/N_0, the coefficient multiplying the complementary error function in Eq. (3.41) converges to one. In this situation the upper bound on the

average bit error probability becomes

$$P_b \leq \frac{1}{2} erfc\left[\sqrt{E_b/N_0}\right],$$

which is equivalent to the performance of ideal coherent QPSK. Therefore, it is possible to improve the performance of quadrature pulse overlapping modulated signals simply by using the memory introduced by the overlapping pulse. Fig. 3.5 shows a plot of this upper bound along with the performance of ideal coherent QPSK. Simulation results are also given to verify the tightness of the upper bound. The pulse shape used for the simulation results is $p(t) = (1 + cos(\pi t/T))/2$. The effect of the double-interval overlapping pulse on the performance is negligible especially at high E_b/N_0. Therefore, one can select the appropriate pulse shape for a compact spectrum without worrying about the performance.

We have see in Chapter 2 that by spreading the pulse shape over more than *two symbol* intervals, QPOM signals with more compact spectra are obtained. Consider the case when the pulse shape is defined over the interval $[-KT, KT]$, i.e.,

$$p(t) = p(-t), \qquad |t| \leq KT$$

$$p(t) = 0, \qquad |t| \geq KT.$$

Over one symbol interval, the two components of the transmitted become:

$$s_I(t) = \sum_{i=0}^{2K-1} A_{n-i} p(t - (n + i - K + 1)T)$$

$$s_Q(t) = \sum_{i=0}^{2K-1} B_{n-i} p(t - (n + i - K + 1)T)$$

It is observed that the in-phase component becomes a function of $\{a_n, a_{n-1}, \ldots, a_{n-2K+1}\}$, and the quadrature component becomes a function of

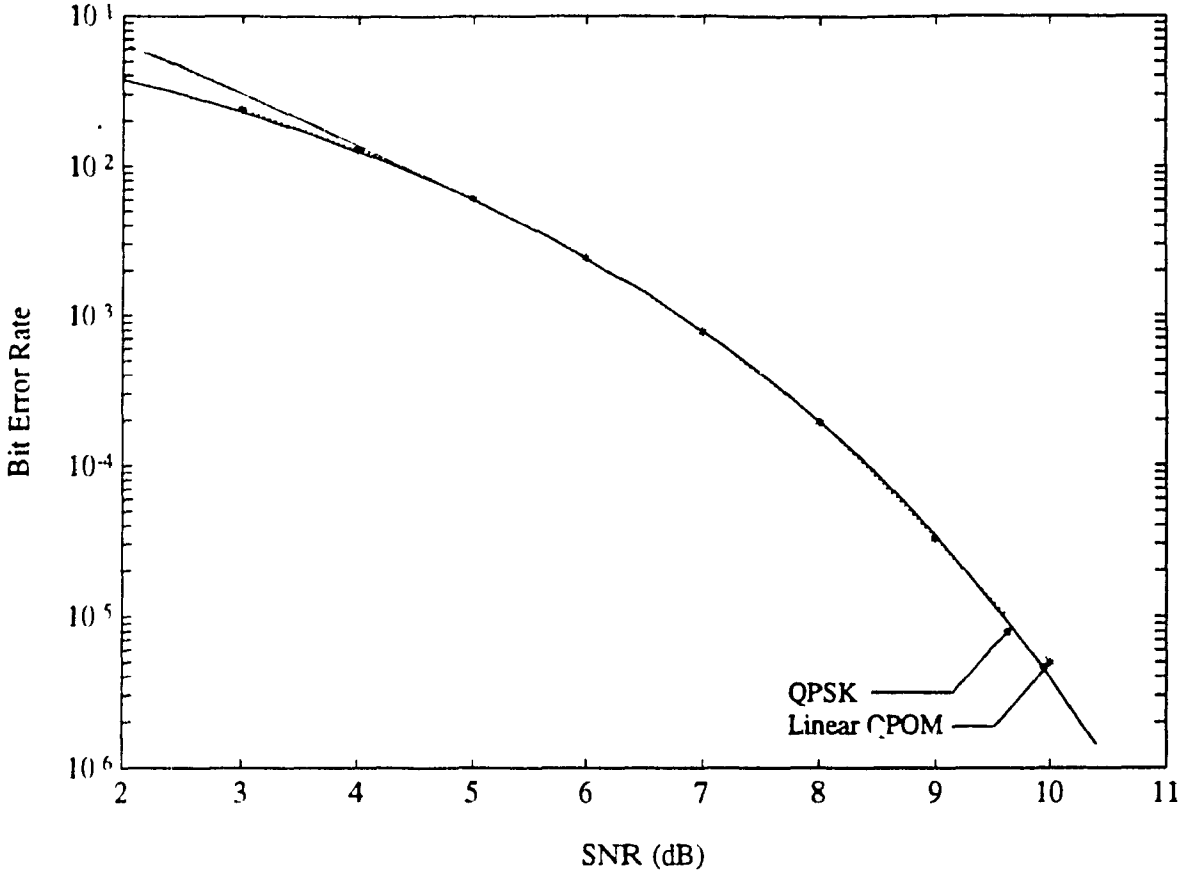

Fig. 3.5 – Performance of linear QPOM signals in AWGN channels.

$\{b_n, b_{n-1}, \ldots, b_{n-2K+1}\}$. In such a situation, the QPOM encoder of each component will have a total of 2^{2K-1} states.

Following the same procedure used for double interval pulse shapes, it is easy to show that the minimum squared Euclidean distance of each component is given by:

$$d^2_{\min} = \frac{2}{E_b} \sum_{i=0}^{K-1} \int_0^T p^2(t - iT)dt = 4,$$

which is equivalent to Eq. (3.40). Therefore, the performance of QPOM signals using this kind of pulse shapes is comparable to that of ideal coherent QPSK.

The results of this section indicate that the performance of linear QPOM signals is asymptotically independent of the length of the pulse shape. However the complexity of the receiver increases exponentially with $2K$. In other words a compromise between spectrum shaping and complexity is needed.

3.1.4. Performance of Linear Offset-QPOM signals

The only difference between Offset-QPOM and QPOM is that a time delay of $T_d = T/2$ seconds is introduced at the quadrature side of the modulator. As discussed in Chapter 2, the advantage of this time delay is apparent only when the transmitted signal undergoes nonlinear channels.

When the quadrature component of the transmitted signal is delayed by $T/2$ seconds, $s(t)$ becomes

$$s(t) = \sum_{n=-\infty}^{+\infty} A_n p(t - nT)\cos 2\pi f_c t + \sum_{n=-\infty}^{+\infty} B_n p(t - nT - T/2)\sin 2\pi f_c t, \quad (3.42)$$

where A_n, B_n are as defined in Eqs. (2.14a, b). Over one symbol interval

$nT \le t \le (n+1)T$, the signal s(t) can be rewritten as:

$$s(t) = s'_I(t)\cos 2\pi f_c t + s'_Q(t)\sin 2\pi f_c t, \tag{3.43}$$

where

$$s'_I(t) = s_I(t)$$

and

$$s'_Q(t) = s_Q(t + T - T/2) + s_Q(t - T/2).$$

Linear Offset-QPOM signals can be easily obtained from the block diagram of Fig. 3.2 by a simple modification. The obtained block diagram is shown in Fig. 3.6. The time delay T_d does not affect the operation of the linear encoder (block B_Q). Therefore, the demodulation of Offset-QPOM signals is expected to be similar to that of QPOM signals with the same complexity. The optimum MLSE receiver is similar to the one given in Fig. 3.4 with the exception of the sampling instants of the quadrature component ($kT + T_d$ instead of kT), which should take into account the time delay introduced at the modulator.

We can then conclude that the performance of Offset-QPOM signals is equivalent to that of QPOM signals. This means that the time delay has no effect on the performance of linear QPOM signals as well.

For most applications using nonlinear amplification for high power efficiency, constant envelope signals are desirable. In the following section we consider the performance of constant envelope, power-efficient QPOM signals over the AWGN channel. As discussed in Chapter 2, an ideal hard-limiter is used after the QPOM scheme to provide an output modulated signal with constant envelope.

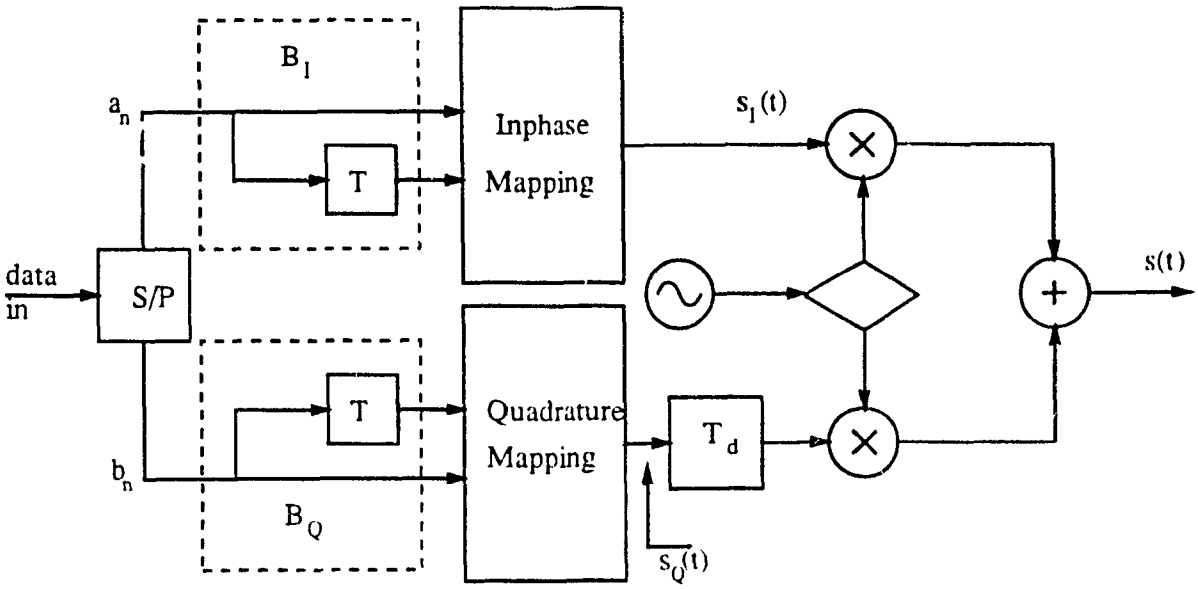

Fig. 3.6 - The new configuration of linear Offset-QPOM schemes.

3.2. NONLINEAR QPOM SCHEMES

3.2.1. Hard-Limited QPOM signals

Consider the block diagram of Fig. 2.6, the hard-limited QPOM transmitted signal $z(t)$ is given by:

$$z(t) = z_I(t)\cos 2\pi f_c t + z_Q(t)\sin 2\pi f_c t, \tag{3.44}$$

where $z_I(t)$ and $z_Q(t)$ are in-phase and quadrature equivalent baseband components of the hard-limited QPOM signal with

$$z_I(t) = \frac{s_I(t)}{\left[s_I^2(t) + s_Q^2(t)\right]^{1/2}}, \tag{3.45a}$$

and

$$z_Q(t) = \frac{s_Q(t)}{\left[s_I^2(t) + s_Q^2(t)\right]^{1/2}}. \tag{3.45b}$$

The signals $s_I(t)$ and $s_Q(t)$ are as defined in (3.2).

The above equations indicate that for any change in $s_I(t)$ (or $s_Q(t)$), $z_I(t)$ and $z_Q(t)$ are affected. Therefore, hard-limiting introduces crosstalk between the in-phase and quadrature components of the transmitted signal, i.e., the two components of the transmitted signal are no longer independent. In this case each component $z_I(t)$ or $z_Q(t)$ becomes a function of $\{a_n, b_n, a_{n-1}, b_{n-1}\}$. Depending on the values of these bits, eight different waveforms are possible for each component of the transmitted signal. The first *four* of these waveforms are given by:

$$z_0(\tau) = \frac{1}{\sqrt{2}}, \qquad 0 \le \tau \le T, \tag{3.46a}$$

$$z_1(\tau) = \frac{s_0(\tau)}{\left[s_0^2(\tau) + s_1^2(\tau)\right]^{1/2}}, \qquad 0 \le \tau \le T, \tag{3.46b}$$

$$z_2(\tau) = \frac{s_1(\tau)}{\left[s_0^2(\tau) + s_1^2(\tau)\right]^{1/2}}, \qquad 0 \le \tau \le T, \tag{3.46c}$$

and

$$z_3(\tau) = \begin{cases} \dfrac{1}{\sqrt{2}}, & 0 \le \tau \le T/2 \\ -\dfrac{1}{\sqrt{2}}, & T/2 \le \tau \le T. \end{cases} \tag{3.46d}$$

The remaining *four* waveforms are antipodal to those given above. As an illustrative example, Fig. 3.7 shows the plots of these waveforms for the double-interval overlapping raised cosine pulse shape $0.5(1 + \cos\pi t/T)$. Table 3.3 gives the relationship between the set $\{a_n, b_n, a_{n-1}, b_{n-1}\}$ and the transmitted pair of waveforms $(z_I(t), z_Q(t))$. This indicates that it is possible to model the hard-limited QPOM scheme by two separate blocks as shown in Fig. 3.8. The first block (called the QPOM encoder) generates the set $\{a_n, b_n, a_{n-1}, b_{n-1}\}$, and the second block (called the QPOM memoryless modulator) maps this set to the corresponding pair of waveforms. We notice that this new configuration does not contain a hard-limiter and overlapping pulse shapes, because all these devices have been incorporated into the equivalent system. The trellis diagram of the QPOM encoder is given in Fig. 3.9. This trellis diagram has 4 states and is fully connected. The possible outputs of the encoder are defined by the set A = (0, 1, . . ., 15), which is partitioned into four disjoint subsets as shown in Fig. 3.9.

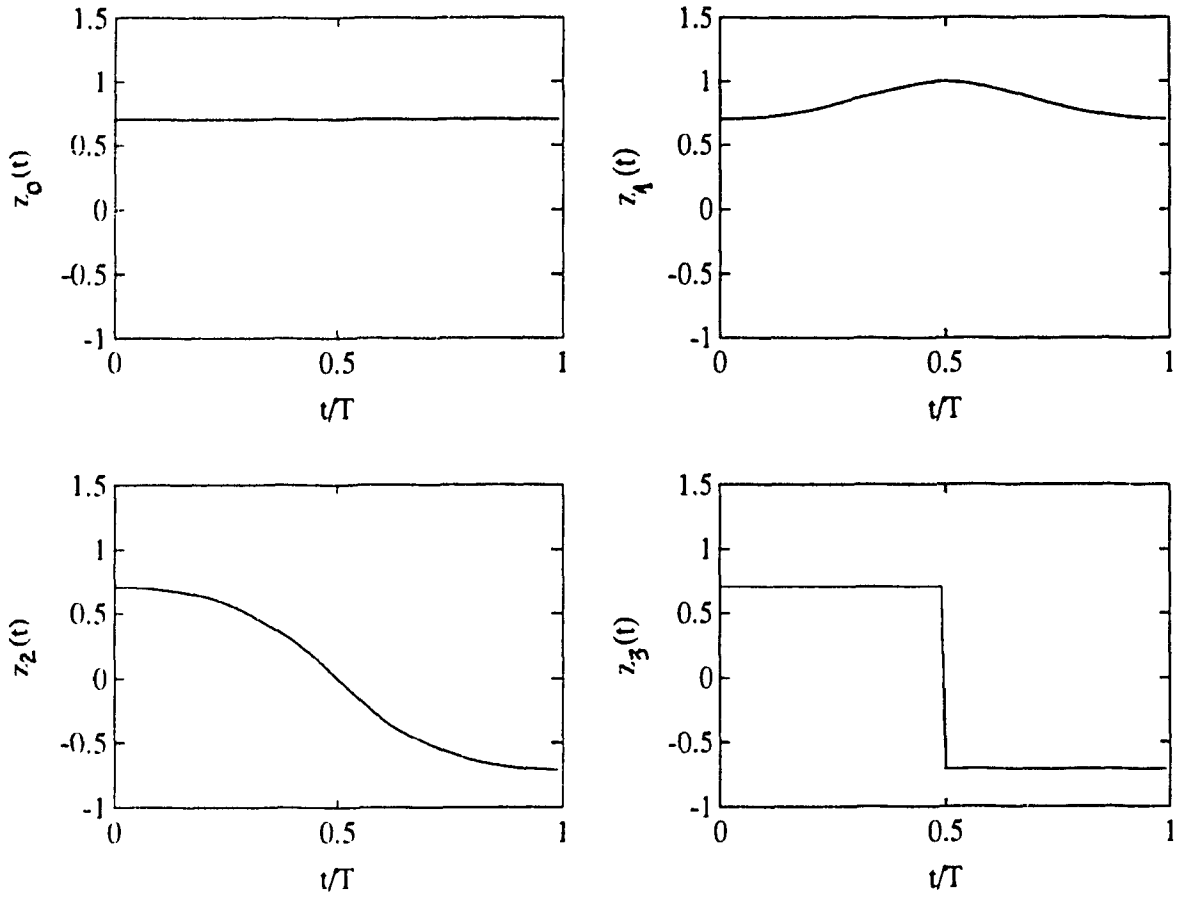

Fig. 3.7 – Example of transmitted pulses for the hard-limited QPOM schemes

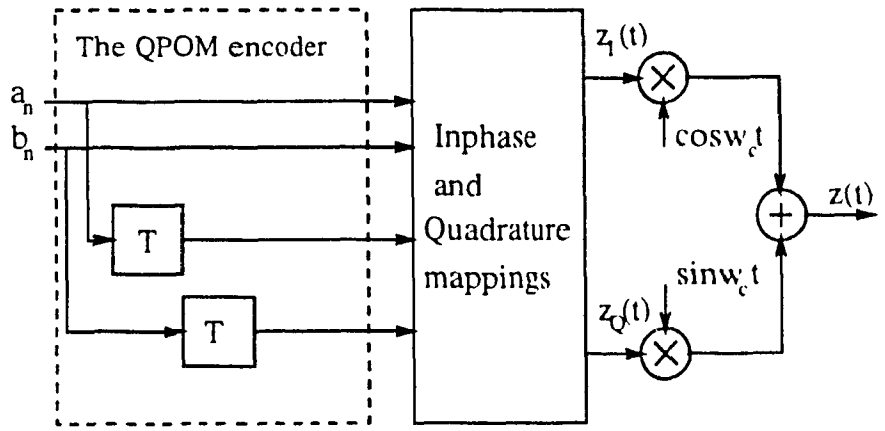

Fig. 3.8 - The new configuration of hard-limited QPOM schemes.

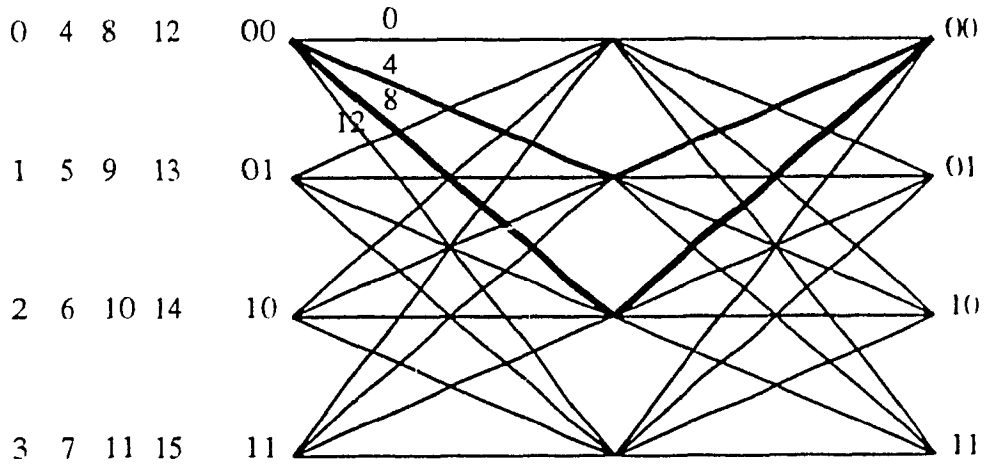

Fig. 3.9 - The trellis diagram of the hard-limited QPOM encoder.

It can be seen from Eqs. (3.46a, b, c, d) that the four waveforms are linearly independent. Therefore, an orthonormal basis $(\phi_0(\tau), \phi_1(\tau), \phi_2(\tau), \phi_3(\tau))$ can be found (e.g., using the Gram-Schmidt procedure). Accordingly, the waveform $\{z_i(\tau)\}$ can be written as:

$$z_i(\tau) = \sum_{j=0}^{3} z_{ij}\phi_j(\tau), \quad i = 0, \ldots, 3. \tag{3.47}$$

The waveform $z_i(\tau)$ can then be represented by the vector of its coefficients in the signal space $(\phi_0(\tau), \phi_1(\tau), \phi_2(\tau), \phi_3(\tau))$. This vector is a 4-element vector denoted as $\underline{z}_{Ii}$ (if $z_i(\tau)$ represents $z_I(t)$) or $\underline{z}_{Qi}$ (if $z_i(\tau)$ represents $z_Q(t)$), and defined as:

$$\underline{z}_{Ii} \text{ or } \underline{z}_{Qi} = (z_{i0}, z_{i1}, z_{i2}, z_{i3}), \tag{3.48a}$$

where

$$z_{il} = \int_0^T z_i(\tau)\phi_l(\tau)d\tau, \qquad l = 0, \ldots, 3. \tag{3.48b}$$

The optimum MLSE receiver of hard-limited QPOM signals needs to treat both components $z_I(t)$ and $z_Q(t)$ at the same time. The only way to do that is to combine the two vectors $\underline{z}_{Ii}$ and $\underline{z}_{Qi}$. In this case the ith transmitted pair of waveforms $(z_I(t), z_Q(t))$ can be represented by a unique augmented vector $\underline{z}_i$ defined as:

$$\underline{z}_i = (\underline{z}_{Ii}, \underline{z}_{Qj}) = (z_{i0}, z_{i1}, z_{i2}, z_{i3}, z_{i4}, z_{i5}, z_{i6}, z_{i7}), \tag{3.50}$$

$$z_{ij} = \begin{cases} \displaystyle\int_0^T z_I(t)\phi_j(t)dt, & j = 0, \ldots, 3 \\ \\ \displaystyle\int_0^T z_Q(t)\phi_{j-4}(t)dt, & j = 4, \ldots, 7. \end{cases}$$

We can see that by using this vector representation, the MLSE receiver will see the two components of the received signal as one entity to be estimated.

Table 3.3
Mapping Rules for Hard-Limited QPOM Schemes

Dec.	Symbol $a_n b_n \; a_{n-1} b_{n-1}$	Transmitted signals $(s_I(t), s_Q(t))$
0	00 00	$(-z_0(t), -z_0(t))$
1	00 01	$(-z_1(t), -z_2(t))$
2	00 10	$(-z_2(t), -z_1(t))$
3	00 11	$(-z_3(t), -z_3(t))$
4	01 00	$(-z_1(t), +z_2(t))$
5	01 01	$(-z_0(t), +z_0(t))$
6	01 10	$(-z_3(t), +z_3(t))$
7	01 11	$(-z_2(t), +z_1(t))$
8	10 00	$(+z_2(t), -z_1(t))$
9	10 01	$(+z_3(t), -z_3(t))$
10	10 10	$(+z_0(t), -z_0(t))$
11	10 11	$(+z_1(t), -z_2(t))$
12	11 00	$(+z_3(t), +z_3(t))$
13	11 01	$(+z_2(t), +z_1(t))$
14	11 10	$(+z_1(t), +z_2(t))$
15	11 11	$(+z_0(t), +z_0(t))$

3.2.2. Performance of Hard-Limited QPOM Signals

The MLSE receiver for hard-limited QPOM signals is shown in Fig. 3.10. The received signal is down-converted to baseband, then each component is passed through a bank of *four* matched filters with impulse response $\{\phi_i(T-t)\}$ and sampled every T seconds giving the elements of the augmented vector $\underline{z}_i$. This vector is then used by the Viterbi processor to estimate the transmitted data. Compared to linear QPOM schemes, only one Viterbi processor is needed but here the number of states is doubled.

In analyzing the performance of hard-limited QPOM signals we consider the trellis diagram of Fig. 3.9 and Table 3.3. Using Eq. (3.36), the weight profile of the hard-limited

QPOM scheme is calculated. These analysis showed that the weight profile is the same for all possible subsets $\mathbf{A}_i$. The results with respect to all possible values of the error event $\mathbf{e}$ are given in Appendix A. These results show that the hard-limited QPOM scheme satisfies the properties 1 and 2, which makes it a modulation scheme with EUP. Hence, its transfer function can be obtained using the modified state diagram of Fig. 3.11. Using Appendix A, the branch labels of this error state diagram are obtained as:

$$t_1 = 0.5(D^{\alpha_3} + D^{\alpha_4}), \qquad t_2 = D^{\alpha_2},$$

$$t_3 = 0.5N(D^{\alpha_3} + D^{\alpha_4}), \qquad t_4 = ND^{\alpha_2}$$

$$t_5 = 0.5N(D^{\alpha_1} + D^{\alpha_5}), \qquad t_6 = ND^{\alpha_0}.$$

The transfer function is given by Eq. (3.37), where

$$X_0 = 0.5(D^{\alpha_1} + D^{\alpha_4})X_1 + 0.5(D^{\alpha_3} + D^{\alpha_4})X_2 + D^{\alpha_2}X_3$$

$$X_1 = 0.5N(D^{\alpha_3} + D^{\alpha_4})X_i + ND^{\alpha_2}X_1 + ND^{\alpha_2}X_2 + 0.5N(D^{\alpha_1} + D^{\alpha_5})X_3$$

$$X_2 = 0.5N(D^{\alpha_3} + D^{\alpha_4})X_i + ND^{\alpha_2}X_1 + ND^{\alpha_2}X_2 + 0.5N(D^{\alpha_1} + D^{\alpha_5})X_3$$

$$X_3 = ND^{\alpha_2}X_i + 0.5N(D^{\alpha_1} + D^{\alpha_5})X_1 + 0.5N(D^{\alpha_1} + D^{\alpha_5})X_2 + ND^{\alpha_0}X_3,$$

and α_i represents the squared Euclidean distance between two pairs of waveforms $(z_i(\tau), z_j(\tau))$ and $(z_k(\tau), z_l(\tau))$. The distance α_i is normalized to the bit energy E_b. The bit energy is obtained by considering all possible pair of waveforms. This yields,

$$E_b = T/2,$$

and

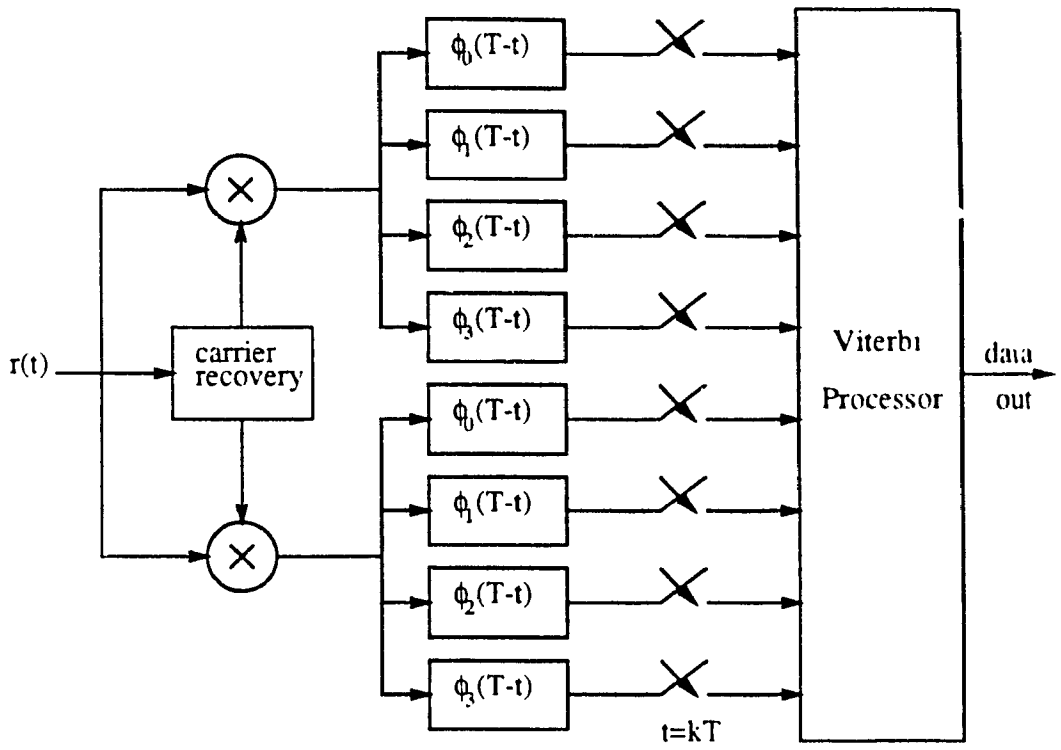

Fig. 3.10 - The MLSE receiver for hard-limited QPOM signals.

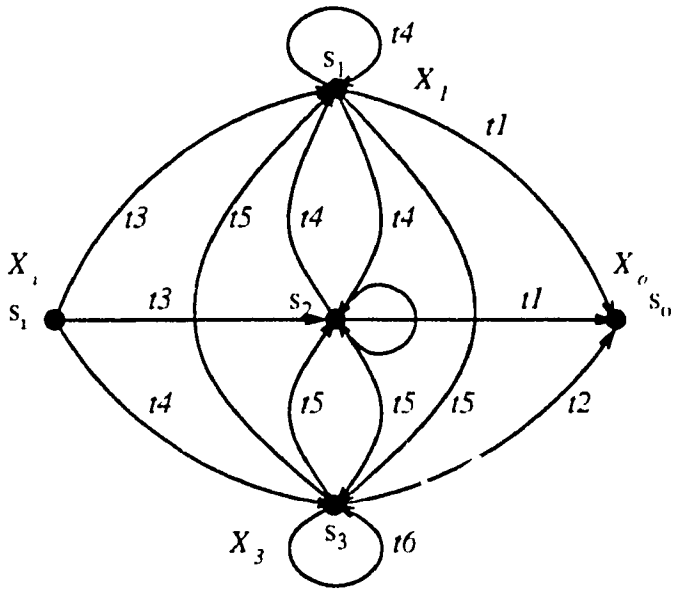

Fig 3.11 - Modified state diagram for computing the transfer function of hard-limited QPOM schemes.

$$\begin{aligned} \alpha_0 &= 8, \qquad \alpha_1 = 4(1+\beta_0), \qquad \alpha_3 = 4(1-\beta_0), \\ \alpha_2 &= 4, \qquad \alpha_5 = 4(1+\beta_1), \qquad \alpha_4 = 4(1-\beta_1), \end{aligned} \tag{3.51}$$

with β_0 and β_1 two coefficients depending on the baseband pulse shape $p(t)$, and are given by:

$$\beta_0 = \frac{1}{T} \int_0^T \frac{p(t)}{\left[p^2(t) + p^2(t-T)\right]^{1/2}} dt, \tag{3.52a}$$

$$\beta_1 = \frac{1}{T} \int_0^{T/2} \frac{p(t) - p(t-T)}{\left[p^2(t) + p^2(t-T)\right]^{1/2}} dt, \tag{3.52b}$$

respectively. Solving the state equations, the transfer function becomes [38, 45]:

$$T(D,N) = \frac{W_0(D)N + W_1(D)N^2}{1 - Q_0(D)N - Q_1(D)N^2}, \tag{3.53}$$

where

$$W_0(D) = 0.5D^{2\alpha_3} + 0.5D^{2\alpha_4} + D^{\alpha_3+\alpha_4} + D^{2\alpha_2},$$

$$W_1(D) = D^{\alpha_1+\alpha_2+\alpha_3} + D^{\alpha_2+\alpha_3+\alpha_5} + D^{\alpha_1+\alpha_2+\alpha_4} + D^{\alpha_2+\alpha_4+\alpha_5}$$

$$- D^{\alpha_0+\alpha_3+\alpha_4} - 0.5D^{\alpha_0+2\alpha_3} - 0.5D^{\alpha_0+2\alpha_4} - 2D^{3\alpha_2},$$

$$Q_0(D) = D^{\alpha_0} + 2D^{\alpha_2},$$

and

$$Q_1(D) = 0.5D^{2\alpha_1} + 0.5D^{2\alpha_5} + D^{\alpha_1+\alpha_5} - 2D^{\alpha_0+\alpha_2}.$$

The minimum normalized squared Euclidean distance of the code is obtained from the

transfer function using Eq. (3.40), which is

$$d_{\min}^2 = 8(1-\beta_m), \tag{3.54}$$

where β_m represents the maximum between β_0 and β_1.

Combining Eqs. (3.34), (3.53) and (3.54), the upper bound on the average bit error probability is obtained as:

$$P_b \le \frac{1}{2} erfc\left[\left[2(1-\beta_m)E_b/N_0\right]^{1/2}\right]\psi(E_b/N_0, \beta_m), \tag{3.55}$$

where the function $\psi(E_b/N_0, \beta_m)$ is given by:

$$\psi(E_b/N_0, \beta_m) = D^{d_{\min}^2} \frac{W_0(D)(1+Q_1(D)) + W_1(D)(2-Q_0(D))}{2\left[1-Q_0(D)-Q_1(D)\right]^2}$$

with $D = e^{-E_b/4N_0}$.

It is noted that at high signal-to-noise ratio, the function $\psi(E_b/N_0, \beta_m)$ converges to a constant C. In this situation, the upper bound on P_b becomes:

$$P_b \le \frac{C}{2} erfc\left[\left[2(1-\beta_m)E_b/N_0\right]^{1/2}\right], \tag{3.56}$$

where

$$C = \begin{cases} C = 1.00, & \beta_m = 0.5 \\ C = 0.25, & \beta_m \neq 0.5. \end{cases}$$

When $\beta_m = 0.5$, Eq. (3.55) becomes

$$P_b \le \frac{1}{2} erfc\left[\sqrt{E_b/N_0}\right] \frac{1 + 0.5e^{-E_b/N_0}}{\left[1 - e^{-2E_b/N_0} - 2e^{-E_b/N_0}\right]^2}, \tag{3.57}$$

which at high signal-to-noise ratio converges to the performance of ideal coherent QPSK,

$$P_b \le \frac{1}{2} erfc\left[\sqrt{E_b/N_0}\right], \quad E_b/N_0 \gg 1. \tag{3.58}$$

Now consider the expression of the two coefficients β_0 and β_1. They can be rewritten as follows:

$$\beta_0 = \frac{1}{T} \int_0^{T/2} \frac{p(t) + p(t-T)}{\left[p^2(t) + p^2(t-T)\right]^{1/2}} dt \tag{3.59a}$$

$$\beta_1 = \frac{1}{T} \int_0^{T/2} \frac{p(t) - p(t-T)}{\left[p^2(t) + p^2(t-T)\right]^{1/2}} dt. \tag{3.59b}$$

It is observed from the above equations that if $p(t)$ is a *single-interval* pulse shape, i.e.,

$$p(t-T) = 0, \quad t \le T/2$$

then the two coefficients β_0 and β_1 become equal to 0.5, and the performance of the hard-limited QPOM scheme reduces to that of ideal coherent QPSK at high signal-to-noise ratio.

Consider the case of *double-interval* overlapping pulse shapes satisfying the conditions in (2.21). It is easy to show that if $1 \ge p(t) \ge 0 \ \forall\, t$, then

$$p(t) + p(t-T) \ge \left[p^2(t) + p^2(t-T)\right]^{1/2}$$

Hence, we conclude that

$$\left.\begin{array}{l}\beta_0 \ge 0.5 \\ \beta_1 \le 0.5\end{array}\right| \rightarrow \beta_m = \beta_0 \ge 0.5. \tag{3.60}$$

This indicates that the performance of hard-limited QPOM scheme can reach that of ideal coherent QPSK without exceeding it. Table 3.4 gives some double-interval overlapping pulse shapes and their corresponding coefficients β_m. As this Table shows, it is possible to select a double-interval pulse shape $p(t)$ which has a coefficient β_m as close to 0.5 as possible and introduces a compact spectrum.

Table 3.4
Example of Some Double-Interval Overlapping Pulse Shapes and their Coefficients β_m

Pulse shape $p(t)$	The coefficient β_m
$cos(\pi t/2T)$	0.6366
$\cos^2(\pi t/2T)$	0.59017
$\cos^4(\pi t/2T)$	0.55151

Fig. 3.12 gives the upper bound on P_b of hard-limited QPOM signals using the pulse shapes of Table 3.4. Also indicated in this figure is the performance of ideal coherent QPSK. We notice that as β_m approaches 0.5, the performance of the QPOM scheme approaches that of ideal coherent QPSK at high signal-to-noise ratios. Therefore, by an appropriate choice of the pulse shape $p(t)$ we can obtain a transmitted QPOM signal with a compact spectrum and a performance similar to that of ideal coherent QPSK.

Now let us consider hard-limited Offset-QPOM signals. The performance of these signals can be analyzed following the same procedure used for QPOM signals. However, due to the crosstalk that now exists between the two components of the transmitted signal, the analogy that has been used in linear channels cannot be applied here, and the time delay need to be considered from the start. The advantage of this time delay is apparent in the power spectral density of the hard-limited QPOM scheme. Because of this time delay, hard-limited Offset-QPOM signals exhibit a much lower spectral

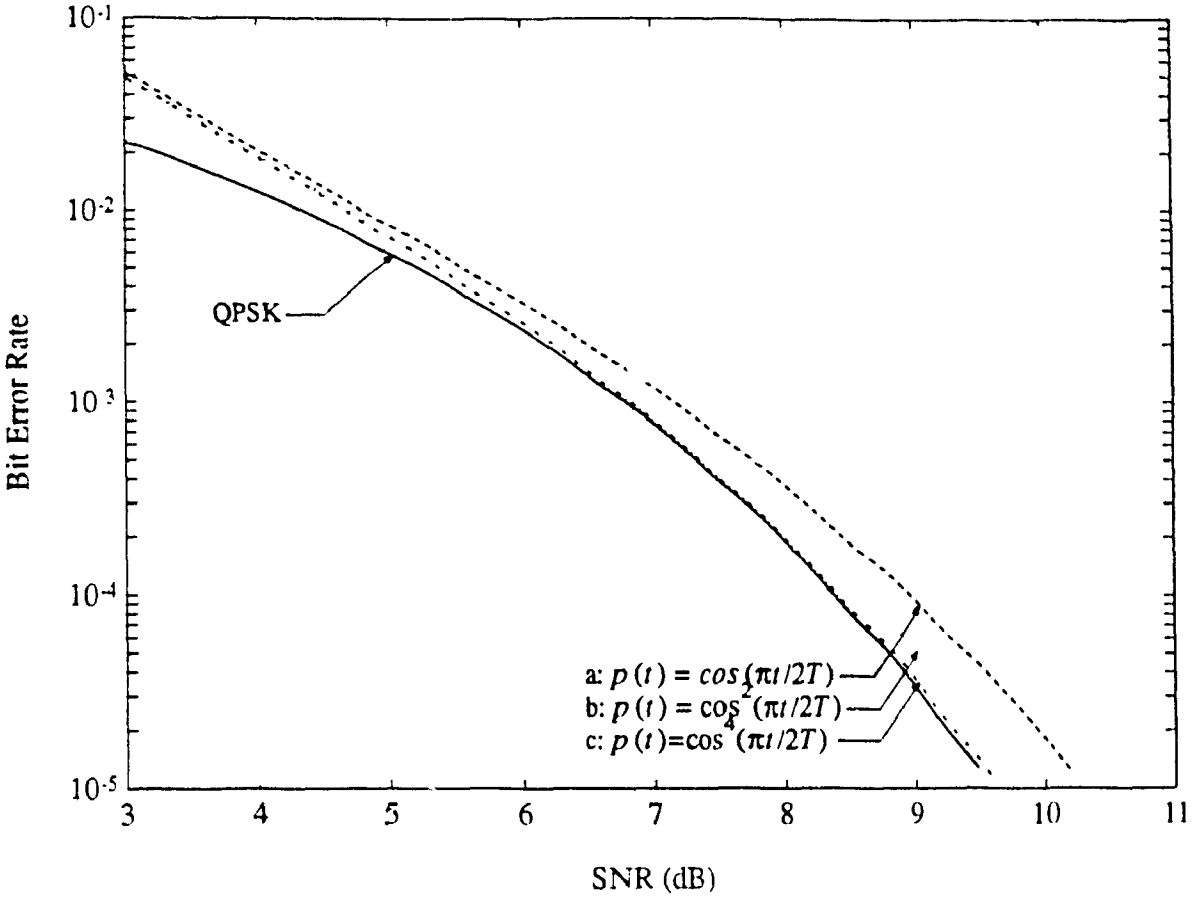

Fig. 3.12 – Performance of hard-limited QPOM signals as a function of the transmitted pulse shape in AWGN channels.

regrowth than QPOM signals when they undergo nonlinear amplifications [32]. Therefore, from spectral point of view hard-limited Offset-QPOM scheme is more attractive. In the next section we will study the effect of the hard-limiter and the time delay on the performance of Offset-QPOM signals.

3.2.3. Performance of Hard-Limited Offset-QPOM signals

Consider the Offset-QPOM transmitted signal $s(t)$ defined in (3.43). Within the symbol interval $[nT, (n+1)T]$, the components of this signal can be rewritten as:

$$s'_I(t) = A_n p(t - nT) + A_{n-1} p(t - (n-1)T),$$

$$s'_Q = B_n p(t - (n+1/2)T) + B_{n-1} p(t - (n-1/2)T) + B_{n-2} p(t - (n-3/2)T).$$

When the signal $s(t)$ is passed through a hard-limiter, the two components $z_I(t)$ and $z_Q(t)$ of the obtained signal become a nonlinear function of $s_I(t)$ and $s_Q(t)$ as indicated in (3.45). In this case the effect of the time delay cannot be removed and should be considered in describing hard-limited Offset-QPOM signals. The two components $z_I(t)$ and $z_Q(t)$ are now functions of the set $\{a_n, b_n, a_{n-1}, b_{n-1}, b_{n-2}\}$. As it was done in the previous section, we present the relation between this set and the transmitted pair of waveforms in a table form as shown in Table 3.5. The 16 elements $z_i(\tau)$, $v_i(\tau)$, $i = 0, 1, \ldots, 7$ are related to the elements $s_j(\tau)$, $j = 0, 1$ as follows:

$$z_0(\tau) = \begin{cases} \dfrac{s_1(\tau)}{\left[s_1^2(\tau) + s_1^2(\tau + T/2)\right]^{1/2}} & 0 \le \tau \le T/2 \\ \dfrac{s_1(\tau)}{\left[s_1^2(\tau) + s_1^2(\tau - T/2)\right]^{1/2}} & T/2 \le \tau \le T \end{cases} \tag{3.61a}$$

Table 3.5
Mapping Rules for Hard-Limited Offset-QPOM Schemes

Dec.	Symbol $a_n b_n\ a_{n-1} b_{n-1}\ b_{n-2}$	Transmitted signals $(z_I(t), z_Q(t))$
0	00 00 0	$(-z_0(t), -v_0(t))$
1	00 00 1	$(-z_1(t), -v_1(t))$
2	00 01 0	$(-z_2(t), -v_2(t))$
3	00 01 1	$(-z_3(t), -v_3(t))$
4	00 10 0	$(-z_4(t), -v_4(t))$
5	00 10 1	$(-z_5(t), -v_5(t))$
6	00 11 0	$(-z_6(t), -v_6(t))$
7	00 11 1	$(-z_7(t), -v_7(t))$
8	01 00 0	$(-z_3(t), +v_3(t))$
9	01 00 1	$(-z_2(t), +v_2(t))$
10	01 01 0	$(-z_1(t), +v_1(t))$
11	01 01 1	$(-z_0(t), +v_0(t))$
12	01 10 0	$(-z_7(t), +v_7(t))$
13	01 10 1	$(-z_6(t), +v_6(t))$
14	01 11 0	$(-z_5(t), +v_5(t))$
15	01 11 1	$(-z_4(t), +v_4(t))$
16	10 00 0	$(+z_4(t), -v_4(t))$
17	10 00 1	$(+z_5(t), -v_5(t))$
18	10 01 0	$(+z_6(t), -v_6(t))$
19	10 01 1	$(+z_7(t), -v_7(t))$
20	10 10 0	$(+z_0(t), -v_0(t))$
21	10 10 1	$(+z_1(t), -v_1(t))$
22	10 11 0	$(+z_2(t), -v_2(t))$
23	10 11 1	$(+z_3(t), -v_3(t))$
24	11 00 0	$(+z_7(t), +v_7(t))$
25	11 00 1	$(+z_6(t), +v_6(t))$
26	11 01 0	$(+z_5(t), +v_5(t))$
27	11 01 1	$(+z_4(t), +v_4(t))$
28	11 10 0	$(+z_3(t), +v_3(t))$
29	11 10 1	$(+z_2(t), +v_2(t))$
30	11 11 0	$(+z_1(t), +v_1(t))$
31	11 11 1	$(+z_0(t), +v_0(t))$

$$z_1(\tau) = \begin{cases} \dfrac{s_1(\tau)}{\left[s_1^2(\tau) + s_2^2(\tau+T/2)\right]^{1/2}} & 0 \le \tau \le T/2 \\ \dfrac{s_1(\tau)}{\left[s_1^2(\tau) + s_1^2(\tau-T/2)\right]^{1/2}} & T/2 \le \tau \le T \end{cases} \tag{3.61b}$$

$$z_2(\tau) = \begin{cases} \dfrac{s_1(\tau)}{\left[s_1^2(\tau) + s_1^2(\tau+T/2)\right]^{1/2}} & 0 \le \tau \le T/2 \\ \dfrac{s_1(\tau)}{\left[s_1^2(\tau) + s_2^2(\tau-T/2)\right]^{1/2}} & T/2 \le \tau \le T \end{cases} \tag{3.61c}$$

$$z_3(\tau) = \begin{cases} \dfrac{s_1(\tau)}{\left[s_1^2(\tau) + s_2^2(\tau+T/2)\right]^{1/2}} & 0 \le \tau \le T/2 \\ \dfrac{s_1(\tau)}{\left[s_1^2(\tau) + s_2^2(\tau-T/2)\right]^{1/2}} & T/2 \le \tau \le T \end{cases} \tag{3.61d}$$

$$z_4(\tau) = \begin{cases} \dfrac{s_2(\tau)}{\left[s_2^2(\tau) + s_1^2(\tau+T/2)\right]^{1/2}} & 0 \le \tau \le T/2 \\ \dfrac{s_2(\tau)}{\left[s_2^2(\tau) + s_1^2(\tau-T/2)\right]^{1/2}} & T/2 \le \tau \le T \end{cases} \tag{3.61e}$$

$$z_5(\tau) = \begin{cases} \dfrac{s_2(\tau)}{\left[s_2^2(\tau) + s_2^2(\tau+T/2)\right]^{1/2}} & 0 \le \tau \le T/2 \\ \dfrac{s_2(\tau)}{\left[s_2^2(\tau) + s_1^2(\tau-T/2)\right]^{1/2}} & T/2 \le \tau \le T \end{cases} \tag{3.61f}$$

$$z_6(\tau) = \begin{cases} \dfrac{s_2(\tau)}{\left[s_2^2(\tau) + s_1^2(\tau+T/2)\right]^{1/2}} & 0 \le \tau \le T/2 \\ \dfrac{s_2(\tau)}{\left[s_2^2(\tau) + s_2^2(\tau-T/2)\right]^{1/2}} & T/2 \le \tau \le T \end{cases} \tag{3.61g}$$

$$z_7(\tau) = \begin{cases} \dfrac{s_2(\tau)}{\left[s_2^2(\tau) + s_2^2(\tau+T/2)\right]^{1/2}} & 0 \le \tau \le T/2 \\ \dfrac{s_2(\tau)}{\left[s_2^2(\tau) + s_2^2(\tau-T/2)\right]^{1/2}} & T/2 \le \tau \le T \end{cases} \tag{3.61h}$$

$$v_0(\tau) = \begin{cases} \dfrac{s_1(\tau+T/2)}{\left[s_1^2(\tau) + s_1^2(\tau+T/2)\right]^{1/2}} & 0 \le \tau \le T/2 \\ \dfrac{s_1(\tau+T/2)}{\left[s_1^2(\tau) + s_1^2(\tau-T/2)\right]^{1/2}} & T/2 \le \tau \le T \end{cases} \tag{3.62a}$$

$$v_1(\tau) = \begin{cases} \dfrac{-s_2(\tau+T/2)}{\left[s_1^2(\tau) + s_2^2(\tau+T/2)\right]^{1/2}} & 0 \le \tau \le T/2 \\ \dfrac{s_1(\tau-T/2)}{\left[s_1^2(\tau) + s_1^2(\tau-T/2)\right]^{1/2}} & T/2 \le \tau \le T \end{cases} \tag{3.62b}$$

$$v_2(\tau) = \begin{cases} \dfrac{s_1(\tau+T/2)}{\left[s_1^2(\tau) + s_1^2(\tau+T/2)\right]^{1/2}} & 0 \le \tau \le T/2 \\ \dfrac{s_2(\tau-T/2)}{\left[s_1^2(\tau) + s_2^2(\tau-T/2)\right]^{1/2}} & T/2 \le \tau \le T \end{cases} \tag{3.62c}$$

$$v_3(\tau) = \begin{cases} \dfrac{-s_2(\tau+T/2)}{\left[s_1^2(\tau) + s_2^2(\tau+T/2)\right]^{1/2}} & 0 \le \tau \le T/2 \\ \dfrac{s_2(\tau-T/2)}{\left[s_1^2(\tau) + s_2^2(\tau-T/2)\right]^{1/2}} & T/2 \le \tau \le T \end{cases} \tag{3.62d}$$

$$v_4(\tau) = \begin{cases} \dfrac{s_1(\tau+/2)}{\left[s_2^2(\tau) + s_1^2(\tau+T/2)\right]^{1/2}} & 0 \le \tau \le T/2 \\ \dfrac{s_1(\tau-T/2)}{\left[s_2^2(\tau) + s_1^2(\tau-T/2)\right]^{1/2}} & T/2 \le \tau \le T \end{cases} \tag{3.62e}$$

$$v_5(\tau) = \begin{cases} \dfrac{-s_2(\tau+T/2)}{\left[s_2^2(\tau) + s_2^2(\tau+T/2)\right]^{1/2}} & 0 \le \tau \le T/2 \\ \dfrac{s_1(\tau-T/2)}{\left[s_2^2(\tau) + s_1^2(\tau-T/2)\right]^{1/2}} & T/2 \le \tau \le T \end{cases} \tag{3.62f}$$

$$v_6(\tau) = \begin{cases} \dfrac{s_1(\tau+T/2)}{\left[s_2^2(\tau) + s_1^2(\tau+T/2)\right]^{1/2}} & 0 \le \tau \le T/2 \\ \dfrac{s_2(\tau-T/2)}{\left[s_2^2(\tau) + s_2^2(\tau-T/2)\right]^{1/2}} & T/2 \le \tau \le T \end{cases} \tag{3.62g}$$

$$v_7(\tau) = \begin{cases} \dfrac{-s_2(\tau+T/2)}{\left[s_2^2(\tau) + s_2^2(\tau+T/2)\right]^{1/2}} & 0 \le \tau \le T/2 \\ \dfrac{s_2(\tau-T/2)}{\left[s_2^2(\tau) + s_2^2(\tau-T/2)\right]^{1/2}} & T/2 \le \tau \le T. \end{cases} \tag{3.62h}$$

These waveforms are shown in Fig. 3.13a and Fig. 3.13b for the overlapping pulse shape $p(t) = 0.5(1 + \cos\pi t/T)$.

We notice that the hard-limited Offset-QPOM scheme has a structure similar to that of hard-limited QPOM scheme. Therefore, it is possible to model it by two separate blocks as it was done for the hard-limited QPOM scheme. The block diagram of the new representation is shown in Fig. 3.14, and the trellis diagram of its encoder is shown in

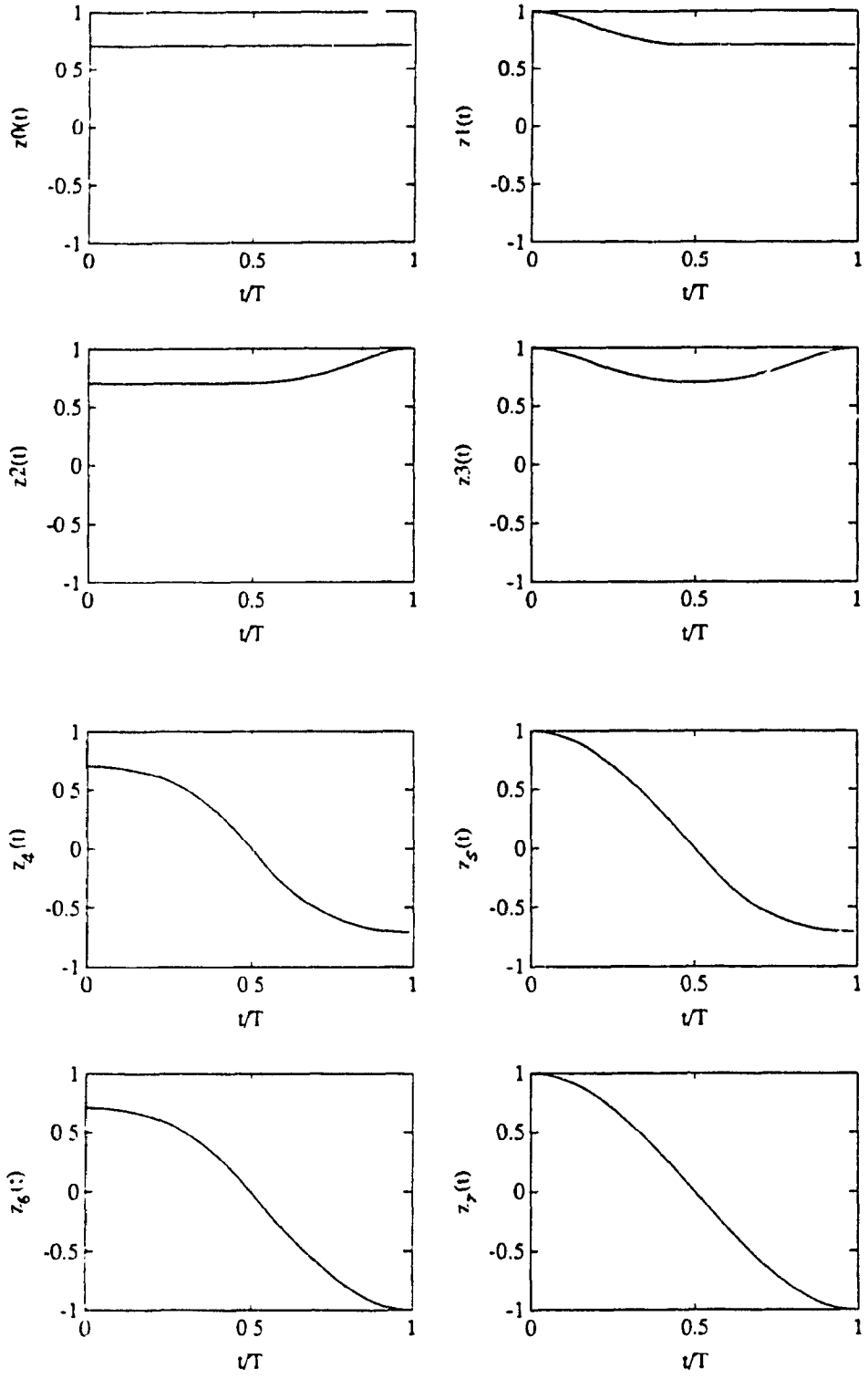

Fig. 3.13a – Example of transmitted pulses for hard-limited Offset-QPOM signals (in-phase component).

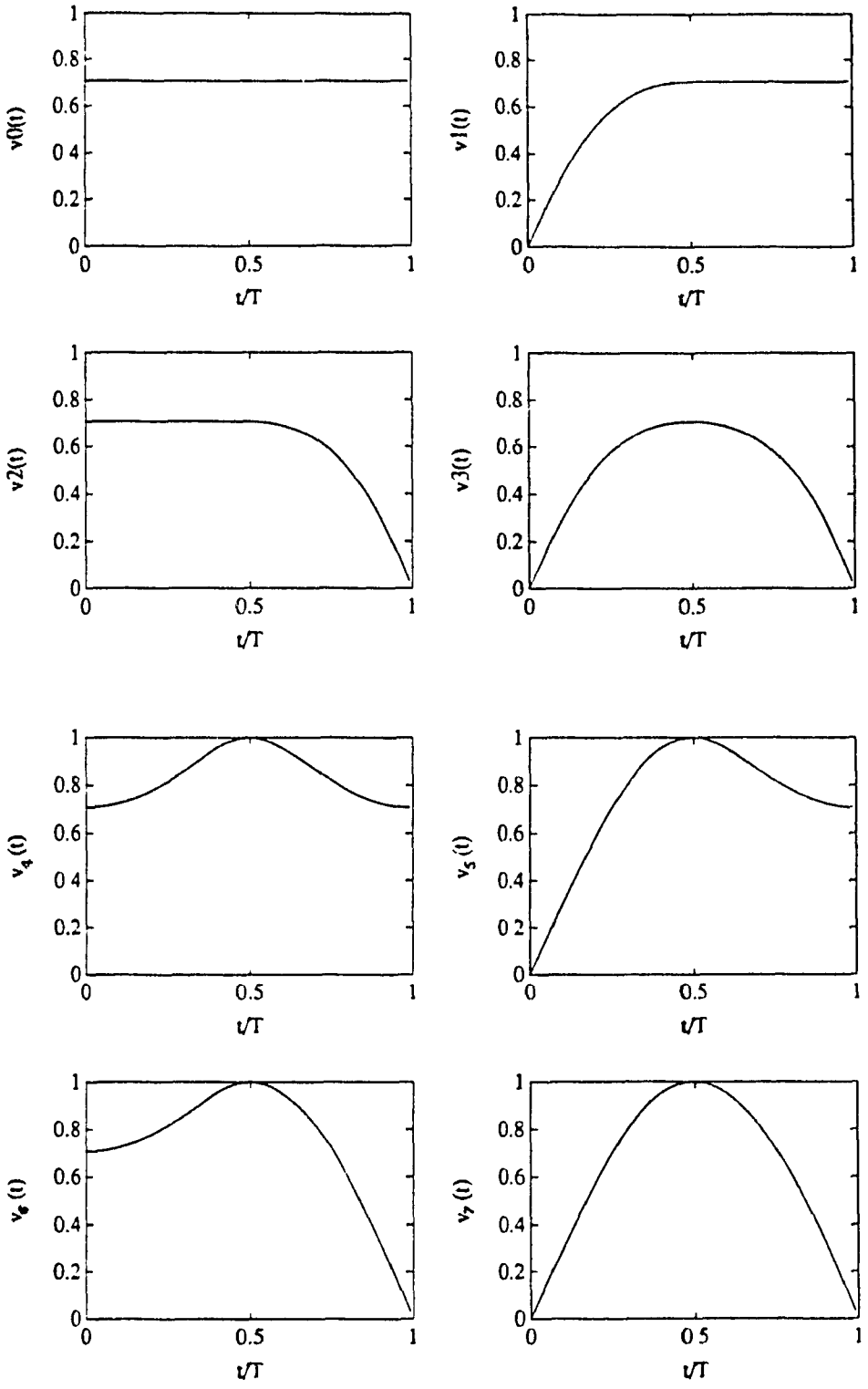

Fig. 3.13b – Example of transmitted pulses for hard-limited Offset-QPOM signals (quadrature component).

Fig. 3.15. The number of states of this encoder is double that of the QPOM scheme, which will have as effect to increase the complexity of the optimum MLSE receiver. The MLSE receiver is then obtained by first finding two orthonormal basis, the first for the set of waveforms $\{z_i(\tau)\}$, and the second for the set of waveforms $\{v_i(\tau)\}$. From Eqs. (3.61, 62), we notice that:

$$z_0(\tau) + z_3(\tau) = z_1(\tau) + z_2(\tau),$$

$$z_4(\tau) + z_7(\tau) = z_5(\tau) + z_6(\tau),$$

$$v_0(\tau) + v_3(\tau) = v_1(\tau) + v_2(\tau),$$

$$v_4(\tau) + v_7(\tau) = v_5(\tau) + v_6(\tau),$$

indicating that these waveforms are linearly dependent. Therefore, only 6 orthonormal waveforms are needed for each basis. The pair of waveforms $(z_I(t), z_Q(t))$ is then represented by an augmented vector $\underline{z}$ of 12-elements. The first 6-elements of this vector are obtained by passing the in-phase component through a bank of 6 matched filters to the first basis, and the last 6-elements are obtained by passing the quadrature component through 6 matched filters to the second basis as shown in Fig. 3.16.

To analyze the performance of hard-limited Offset-QPOM signals, we consider the trellis diagram of Fig. 3.15. This encoder has 8 subsets $\{\mathbf{A}_i, i = 0, \ldots, 7\}$, with each subset having *four* elements. To check the linearity of this encoder, we have computed the weight profile of these subsets for every error event $\mathbf{e}$. As it is indicated in Table 3.6, for the error event $\mathbf{e} = 00011$ the subsets $\{\mathbf{A}_i\}$ have different weight profiles. This means that the weight profile is a function of the subset of channel signals under consideration. In such a situation, the method introduced in [42] cannot be applied.

One way to derive an upper bound on P_b is to consider the method of pairwise error states [41] which involves all possible correct paths (not only the all-zero path). The

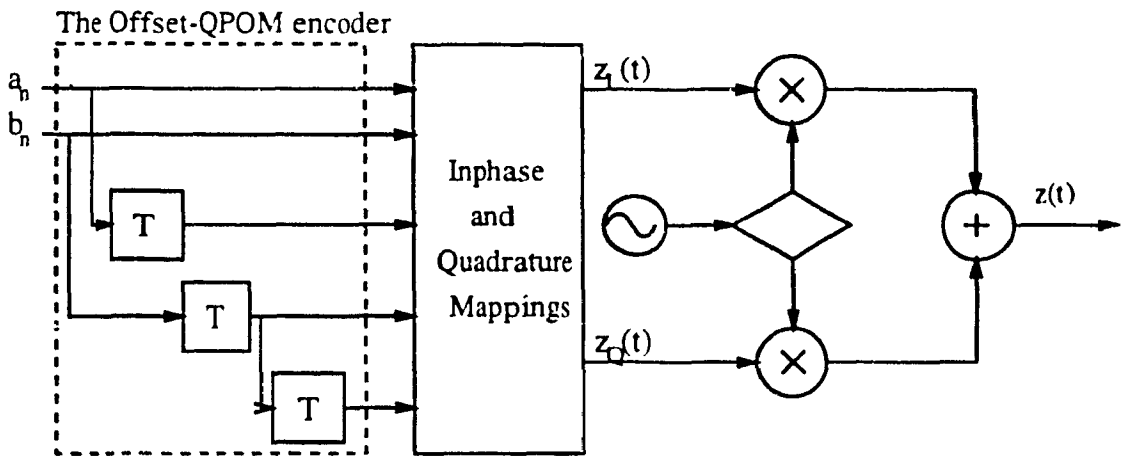

Fig. 3.14 - The new configuration of hard-limited Offset-QPOM schemes.

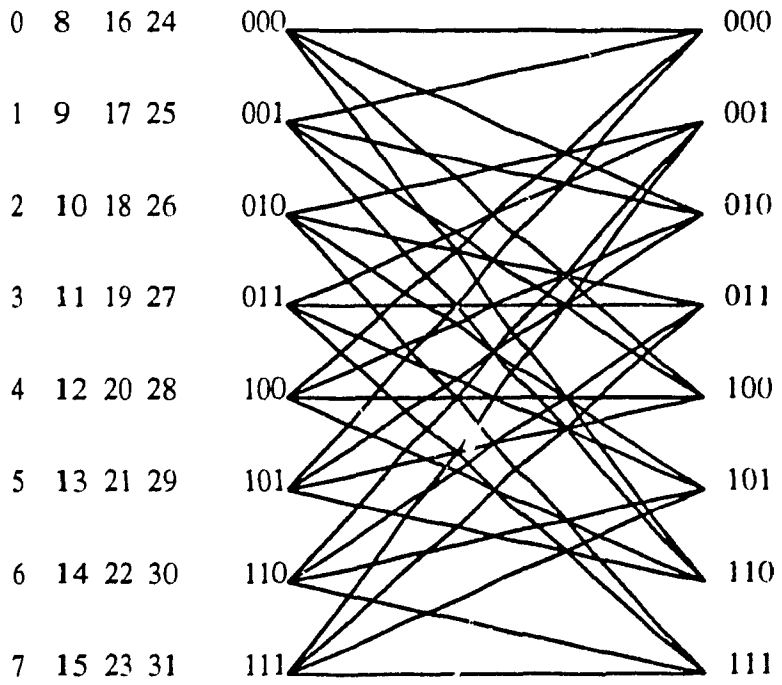

Fig. 3.15 - The trellis diagram of the hard-limited Offset-QPOM encoder

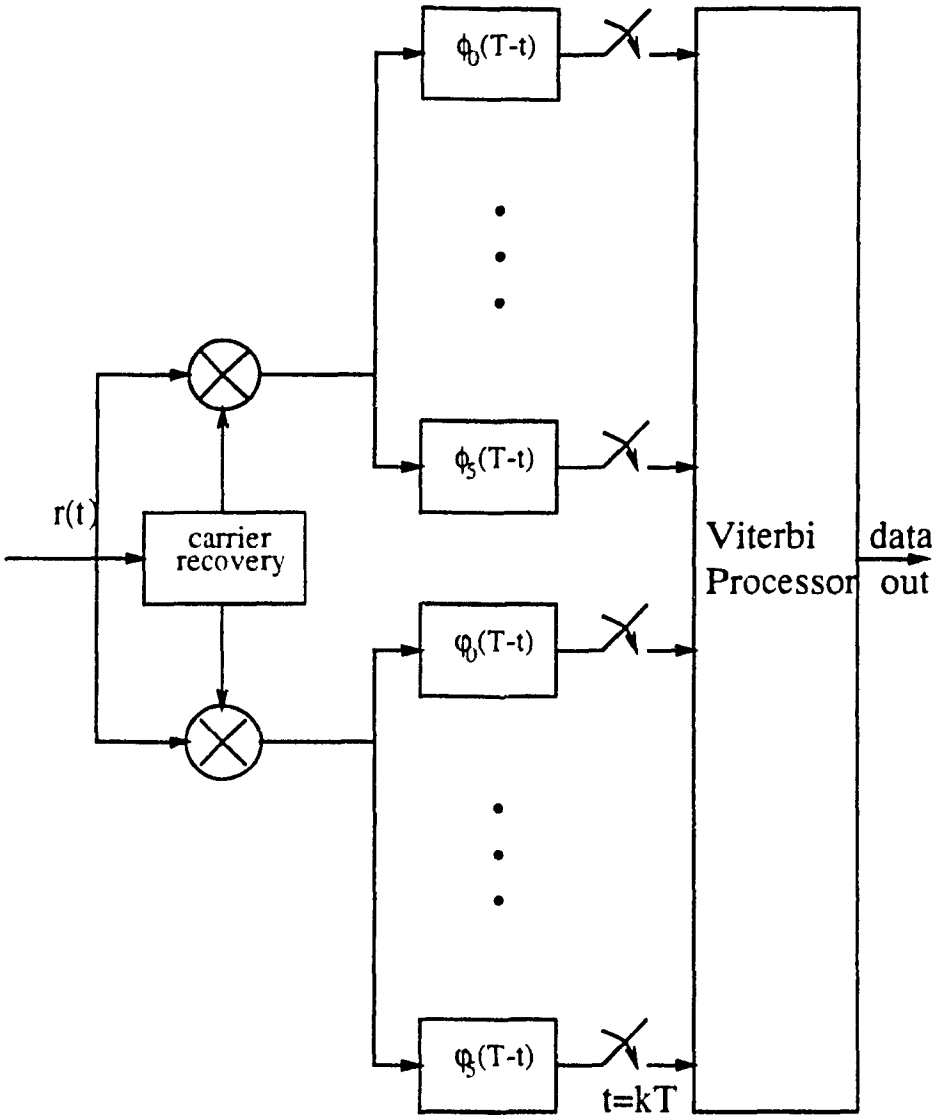

Fig. 3.16 - The MLSE receiver of hard-limited Offset-QPOM signals.

Table 3.6
Hard-limited Offset-QPOM
Weight Profile of Subsets with Respect to 00011
($p(t) = 0.5(1 + \cos\pi t/T)$)

Subset of Channel Signal	Weight Profile
A_0	$2D^{3.52} + 2D^{5.18}$
A_1	$2D^{2.69} + 2D^{4.35}$
A_2	$2D^{2.69} + 2D^{4.35}$
A_3	$2D^{5.18} + 2D^{3.52}$
A_4	$2D^{5.18} + 2D^{3.52}$
A_5	$2D^{4.35} + 2D^{2.69}$
A_6	$2D^{4.35} + 2D^{2.69}$
A_7	$2D^{5.18} + 2D^{3.52}$

modified state diagram then becomes an expanded set of states, namely 2^6 states. As we can see, in order to derive the transfer function for this system, we need to solve a system of 64 equations. This computation is quite complicated or may be impossible to do (analytically).

In order to avoid this computational complexity, we consider the weight profile distribution of the code. By using the worst weight profile for each error event **e**, it is possible to approximate the transfer function from a state diagram containing only *eight* states. With this assumption, the method of [42] can be applied, and a good approximation for the upper bound on P_b can be obtained.

Using Eq. (3.34), the upper bound on P_b is computed. The partial derivative of $T(D, N)$ is numerically computed using Appendix B. Fig. 3.17 [39] shows the performance of hard-limited Offset-QPOM signals for the pulse shape

$p(t)=0.5(1+\cos(\pi t/T))$. As observed from this figure, this scheme has a similar performance compared to hard-limited QPOM scheme. As a result we can say that the only effect of the time delay on the hard-limited Offset-QPOM scheme is in increasing the complexity of the demodulator.

3.3. DISCUSSION

A maximum likelihood sequence estimation receiver for both linear and hard-limited QPOM signals was introduced. This receiver was obtained after decomposing the QPOM scheme into an encoder followed by a memoryless modulator. The memory was presented in a way that could be optimally exploited by the receiver. The performance in AWGN channels was analyzed using an upper bound technique and then verified by computer simulations. It was shown that the performance of these schemes can be expressed as a function of the transmitted pulse shape $p(t)$. Therefore, it is now possible to select double-interval overlapping pulse shapes for a compact spectrum and a good performance simultaneously. The performance of Offset-QPOM signals was also analyzed and discussed. The time delay T_d did not affect the performance of the linear scheme. However, in nonlinear channels, this time delay introduced more correlation into the signal and a more complex receiver was required. It was shown that by properly choosing the pulse shape $p(t)$, we can achieve the performance of ideal coherent QPSK (interference free system). This indicates that the memory has been used affectively in optimizing the MLSE receiver.

Throughout this chapter we have seen that the memory of QPOM schemes can be modeled as an encoder. The trellis diagram of this encoder does not have parallel paths from one state to the next. This feature is very important when the signal is transmitted over fading channels. This issue will be discussed in the next chapter.

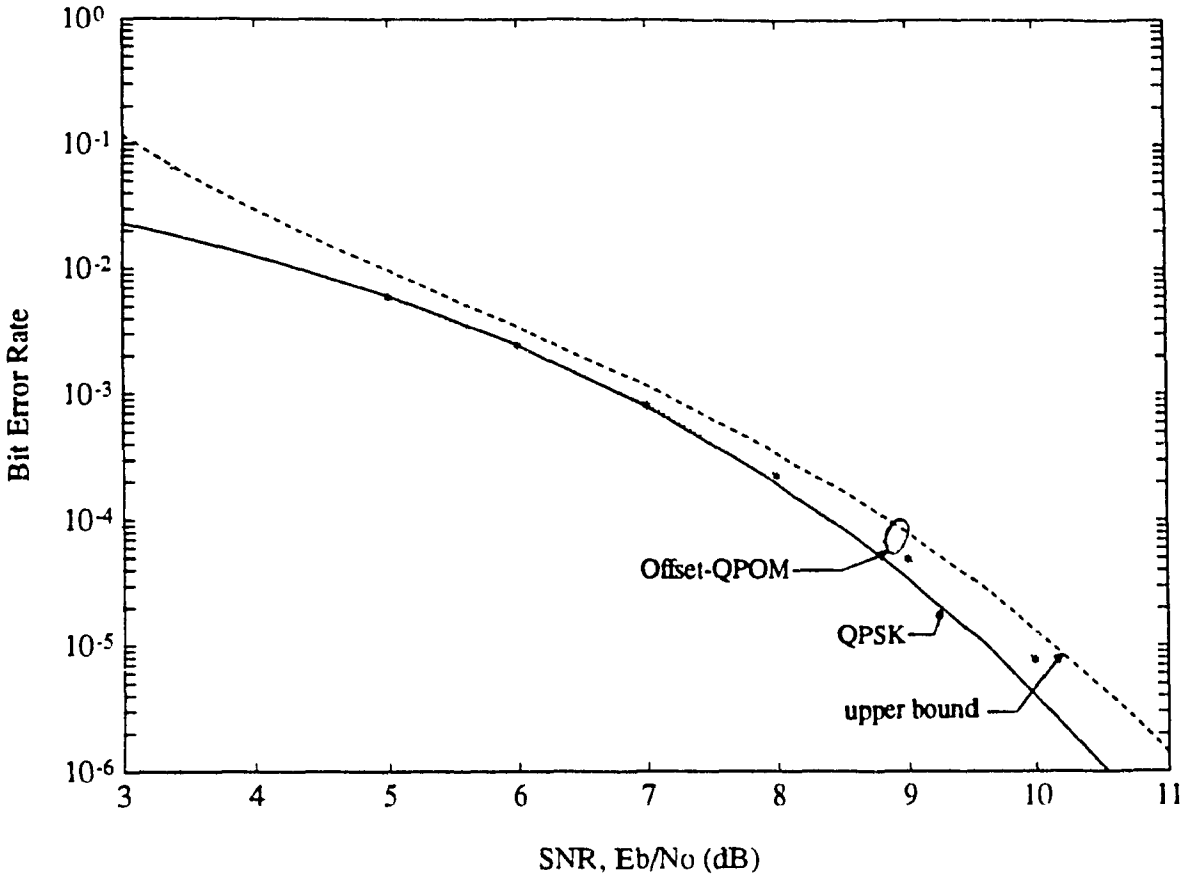

Fig. 3.17 – Performance of hard-limited Offset-QPOM signals in AWGN channels

CHAPTER IV

PERFORMANCE OF QUADRATURE PULSE-OVERLAPPING MODULATED SIGNALS IN FADING CHANNELS

Our objective in this Chapter is to treat the performance of quadrature pulse-overlapping modulated signals over fading channels. The new representation of QPOM schemes introduced in Chapter 3 is suitable for fading channels applications. With this representation, QPOM schemes are expected to perform better than conventional QPSK and will be within the range of some coded schemes of the same net throughput of 2 bits/symbol. We start this Chapter with a brief description about the physical behavior of the fading channel, then a statistical model for this channel will be developed. The performance analysis of the QPOM scheme is carried out in a general form in such a way that it can be applied to both linear and nonlinear QPOM schemes. To better evaluate the QPOM scheme, its performance is compared to conventional QPSK and some coded schemes such as 4-state 8PSK TCM schemes.

4.1. FADING CHANNEL MODEL

In digital communication the most frequently assumed model for a transmission channel is the Additive White Gaussian Noise (AWGN) channel model. However, for many communication systems the AWGN channel is a poor model, and one has to resort to more precise and complicated models. One type of non-Gaussian model which frequently occurs in practice is the *fading channel*. Examples of such a fading channel are the mobile satellite and indoor communication channels. These channels have been studied and used extensively in the literature [24, 51-55].

Fading mostly occurs when the receiving antenna of a given receiver picks up multipath reflections and diffraction from surrounding objects. Which causes a time varying behavior in the receiving signal energy, which is called fading. While there are other degradations such as time varying dispersion, we will consider only the most basic and common model.

Two kinds of fadings, *short–term* and *long–term* fading are often considered in fading channels. In short-term fading the changes in channel characteristics occur within a time scale that ranges from fraction of a second to several seconds. While in long-term fading the variations of the channel characteristics are in the range of minutes, tens of minutes, hours or even more. These variations often related to solar or meteorological influences [24]. Both kinds of variations are of course continually in process. However, the distinction between them is extremely useful for engineering because, for most fading channels, only the short-term fading variation affects the details of the received waveform structure and the inter-relationships of errors within a message; while the long-term variations determine in effect the availability of the channel.

A widely used model for the channels which suffer from short-term fading is linear time-varying filter model of the channel [24]. To fully characterize this propagation, it is necessary to obtain the time-varying impulse response. This has been done by some investigators, using either pulse transmission or pseudorandom binary modulation [51-55]. Important features of the impulse response are the number of different paths and the time delay spread between them and the rate of variation of the impulse response.

If a delta function is applied at the input of the channel, at time t, an output $h(t, \tau)$ at time $t + \tau$ is obtained. In the case of n distinct propagation paths of gain a_i and delay τ_i, we have

$$h(\tau, t) = \sum_{i=1}^{n} a_i(t)\delta(\tau - \tau_i). \tag{4.1}$$

The corresponding equivalent low-pass transfer function of the channel is obtained as:

$$H(f,t) = \int_0^T h(\tau,t)e^{-j2\pi f_c \tau} d\tau, \tag{4.2}$$

which is the Fourier transform of $h(\tau, t)$ relative to its τ-dependence.

Considering $H(f,t)$ as a complex Wide-Sense Stationary (WSS) process [55], it can be characterized by its covariance function defined as:

$$R(\Delta f, \Delta t) = \frac{1}{2} E\left[H(f,t)H^*(f+\Delta f, t+\Delta t)\right], \tag{4.3}$$

if $R(\Delta f, \Delta t)$ is negligible for $|\Delta t| > T_M$ and $|\Delta f| > B_D$, the channel is said to have a fading bandwidth (Doppler spread), B_D, time spread, T_M, and coherence bandwidth $1/T_M$ [55].

The fading channel is characterized by its coherence bandwidth. If the coherence bandwidth of the fading channel is smaller than the signal bandwidth, the signal components with frequency separation greater than the coherence bandwidth are affected differently by the channel. In this case the fading is said to be *frequency-selective* fading. On the other hand, if the coherence bandwidth is large in comparison to the bandwidth of the transmitted signal, the channel is said to be *frequency-nonselective* or flat fading. In other words all of the frequency components in the transmitted signal undergo the same attenuation and phase shift through the channel. This kind of fading is the most common fading channel and is used throughout the rest of the thesis.

When the channel is modeled as flat fading, its impulse response becomes

$$h(\tau, t) = a(t)\,\delta(\tau)$$

with

$$a(t) = a_I(t) + ja_Q(t). \tag{4.4}$$

Then, the received signal at the output of the channel is related to the transmitted signal $s(t)$ as:

$$r(t) = a(t)s(t) + n(t). \tag{4.5}$$

Central limit theorem arguments lead to the conclusion that [27, 55] the in-phase and quadrature components of $a(t)$ are statistically independent Gaussian random processes characterized by their autocorrelation function or their power spectral density, with bandwidth B_D.

4.1.1. Rayleigh Fading Channels

When the received signal consists of a large number of scattered signals of approximately the same group path, with phases differing from one another by random fractions of a wavelength, the two processes $a_I(t)$ and $a_Q(t)$ become zero-mean Gaussian processes. Thus, the fading envelope defined as:

$$a = [a_I^2 + a_Q^2]^{1/2}, \tag{4.6}$$

has a *Rayleigh* distribution with probability density function (p.d.f)

$$p(a) = \frac{a}{\sigma_a^2} e^{-a^2/2\sigma_a^2}, \tag{4.7}$$

where σ_a^2 represents the variance of the constitute Gaussian random process. The average energy of the fading envelope is related to σ_a^2 as:

$$E[a^2] = 2\sigma_a^2. \tag{4.8}$$

The phase of the random process a is uniformly distributed with p.d.f

$$p(\phi_a) = 1/2\pi, \qquad 0 \le \phi \le 2\pi.$$

4.1.2. Rician Fading Channels

When there is a single dominant, nonfading component in the received signal along with a diffused multipath fading process, $a(t)$ can no longer be modeled as a zero-mean Gaussian process. This occurs when there are fixed scatterers or signal reflectors in the medium, in addition to randomly moving scatterers. In such a case studies showed that the envelope of the fading channel is *Rician* distributed, with p.d.f [29]

$$p(a) = 2a(1 + K)e^{-(K + a^2(1 + K))} I_0(2a\sqrt{K(K + 1)}), \tag{4.9}$$

where $I_0(\,.\,)$ is the zero-order modified Bessel function of the first kind, and K is the ratio of the energy of direct component to the energy of the diffused multipath one. In this case the phase is no longer uniformly distributed, but rather is more concentrated around that of the nonfading component. It is important to notice that for $K = 0$, the above model becomes that of a Rayleigh fading channel.

4.2. PERFORMANCE OF QPOM SIGNALS IN FADING CHANNELS

Quadrature pulse overlapping modulation schemes can be seen as coded schemes even though no extra redundancy has been used. As discussed in Chapter 3, the coding structure of these schemes is mainly due to the overlapping pulse shape and the cross correlation caused by the hard-limiter. Coded schemes can be used for transmission of reliable digital information over bandwidth limited fading channels. When combined with interleaving/de-interleaving of sufficient depth, these schemes can provide good coding gains compared to the uncoded ones [29].

The general block diagram of a QPOM system on a fading channel is shown in Fig. 4.1. The input bits are encoded by the QPOM encoder, interleaved and then mapped to the transmitted in-phase and quadrature waveforms. Passed through the channel, the

transmitted signal is faded and corrupted by AWGN. At the receiver, the signal is down-converted to baseband, transformed into a vector, and then de-interleaved. This vector is used by the Viterbi processor to estimate the transmitted information. Further improvement in the performance of the system can be achieved using an estimate of the channel in the decoding process.

Consider the block diagram of Fig. 4.1, the received signal can be written as:

$$r(t) = \mathrm{Re}\{a(t)Z(t)\} + n(t), \tag{4.10}$$

where $Z(t)$ is the equivalent complex signal of z(t), $a(t)$ is a complex fading process, and n(t) is the bandpass additive white Gaussian channel defined as:

$$n(t) = n_c(t)\cos 2\pi f_c t + n_s(t)\sin 2\pi f_c t,$$

and $n_c(t)$, $n_s(t)$ are i.i.d Gaussian random variables with zero mean and variance $N_0/2$.

We assume that the channel fading is sufficiently slow so that the phase shift can be estimated from the received signal without error. In that case ideal coherent detection of the received signal can be achieved. Under this assumption the received signal can be rewritten as:

$$\begin{aligned} r(t) &= |a(t)|z(t) + n(t) \\ &= \left[|a(t)|z_I(t) + n_c(t)\right]\cos 2\pi f_c t + \left[|a(t)|z_Q(t) + n_s(t)\right]\sin 2\pi f_c t. \end{aligned} \tag{4.11}$$

The task of an optimum receiver will be to extract the pair of waveforms $(z_I(t), z_Q(t))$, which can be done by down-converting the received signal to baseband. However, due to the noise introduced by the channel, the obtained pair of waveforms becomes $(r_I(t), r_Q(t))$, where

$$r_I(t) = |a(t)|z_I(t) + n_c(t) \tag{4.12a}$$

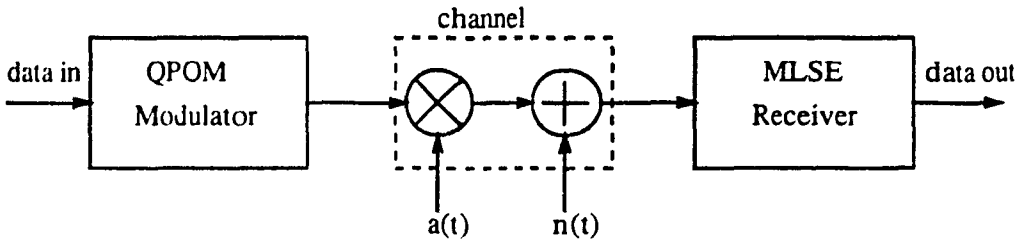

Fig. 4.1 - The block diagram of a QPOM system in a fading channel.

and

$$r_Q(t) = |a(t)| z_Q(t) + n_s(t). \tag{4.12b}$$

If the channel is slow enough in such a way that $|a(t)|$ remains constant over one symbol interval, then the received signal can be represented by the following vector

$$\underline{r}_k = a_k \underline{z}_k + \underline{n}_k, \qquad t = kT. \tag{4.13}$$

The elements of $\underline{n}_k$ are i.i.d zero-mean Gaussian random variables with variance $N_0/2$, $\underline{z}_k$ is the vector corresponding to the transmitted pair of waveforms $(z_I(t), z_Q(t))$ at time kT, and a_k is the amplitude of the fading channel. It is assumed that ideal interleaving/deinterleaving is employed to destroy the memory of the fading channel. This allows us to consider the samples of the fading amplitude, statistically independent.

From Eq. (4.3) we notice that the received signal is a function of the fading amplitude. Therefore, the implementation of the MLSE receiver will depend on the availability of the fading amplitude. Let's represent the transmitted signals by the sequence of N-vectors,

$$\mathbf{z} = \{\underline{z}_0, \underline{z}_1, \ldots, \underline{z}_{N-1}\}, \tag{4.14}$$

the corresponding signal at the output of the discrete time channel by the sequence of N-vectors $\mathbf{r}$, and the channel state information by the N-element vector,

$$\boldsymbol{\rho} = \{\rho_0, \rho_1, \ldots, \rho_{N-1}\}. \tag{4.15}$$

When this vector is extracted from the received signal, the MLSE receiver will use it in the benefit of improving the performance of the system [29].

4.2.1. Ideal Channel State Information

The assumption of ideal channel state information is to consider that the side information random variable ρ_k is equal to the fading amplitude a_k. Thus, since the elements of $\underline{n}_k$ are i.i.d Gaussian random variables the metric can be written as [29]:

$$m(\mathbf{r}, \mathbf{z}, \rho) = -\sum_{n=0}^{N-1} \| \underline{r}_n - a_n \underline{z}_n \|^2, \tag{4.16}$$

where a_n is assumed to be known. Substituting Eq. (4.16) into Eq. (3.23) and conditioning on a the conditional pairwise error probability is obtained as

$$P(\mathbf{z} \to \underline{\hat{\mathbf{z}}} \mid \mathbf{a}) \le \frac{1}{2} erfc\left[\left[d_{\mathbf{a}}^2(\mathbf{z}, \hat{\mathbf{z}}) E_b / 4N_0\right]^{1/2}\right]. \tag{4.17}$$

Applying the Chernoff bound [23], the above equation can approximated by

$$P\{\mathbf{z} \to \underline{\hat{\mathbf{z}}} \mid \mathbf{a}\} \le \frac{1}{2} \exp\left[-d_{\mathbf{a}}^2(\mathbf{z}, \hat{\mathbf{z}}) E_b / 4N_0\right]$$

$$\le \frac{1}{2} D^{d_{\mathbf{a}}^2(\mathbf{z}, \hat{\mathbf{z}})}, \quad D = e^{-E_b/4N_0}, \tag{4.18}$$

where

$$d_{\mathbf{a}}^2(\mathbf{z}, \hat{\mathbf{z}}) = \frac{1}{E_b} \sum_{n=0}^{N-1} a_n^2 \| \underline{z}_n - \underline{\hat{z}}_n \|^2$$

represents the square of the normalized weighted Euclidean distance between the two sequences $\mathbf{z}$ and $\hat{\mathbf{z}}$. The pairwise error probability is then obtained by averaging Eq. (4.18) over the random variable $\mathbf{a}$, i.e.,

$$P\{\mathbf{z} \to \underline{\hat{\mathbf{z}}}\} = E\{P\{\mathbf{z} \to \hat{\mathbf{z}} \mid \mathbf{a}\}\}. \tag{4.19}$$

An upper bound on the bit error probability is then obtained as [29]:

$$P_b \le \sum_{\mathbf{z},\hat{\mathbf{z}} \in C} \sum a(\mathbf{z}, \hat{\mathbf{z}}) P(\mathbf{z}) P\{\mathbf{z} \to \hat{\mathbf{z}}\}$$

$$\le \frac{1}{2k} \frac{\partial}{\partial N} T(\bar{D}, N) \Big|_{N=1}, \tag{4.20}$$

where $P(\mathbf{z})$ is a priori probability of transmitting $\mathbf{z}$, C is the set of all valid sequences, $a(\mathbf{z}, \hat{\mathbf{z}})$ represents the number of bit errors that occur when the sequence $\hat{\mathbf{z}}$ is detected instead of the sequence $\mathbf{z}$, and $T(\bar{D}, N)$ is the transfer function of the scheme encoder obtained from the state diagram whose branch label gains are modified to include the effect of the fading channel. In this case we simply replace D^{d^2} by $\bar{D}$ (the average of D^{d^2} over the random variable $\mathbf{a}$).

When the fading channel is modeled as Rayleigh fading, the multiplicative gain of the received signal is a random variable with probability density function

$$p_{\mathbf{a}}(a) = 2ae^{-a^2}, \tag{4.21}$$

and a mean-square value of unity, i.e., $E\{\mathbf{a}^2\} = 1$. A normalized Rayleigh density function is chosen so that the measured signal energy at the receiver represents the average signal energy per channel symbol, E.

The evaluation of $\bar{D}$ is then obtained as:

$$\bar{D} = \int_0^\infty 2ae^{-a^2} e^{-a^2 \| \underline{z}_n - \underline{\hat{z}}_n \|^2 / 4N_0} da.$$

Evaluating this integral, $\bar{D}$ becomes

$$\bar{D} = \left[1 + \frac{\| \underline{z}_n - \underline{\hat{z}}_n \|^2}{4N_0} \right]^{-1}. \tag{4.22}$$

An upper bound on the average bit error probability is then obtained by combining Eqs. (4.20) and (4.22),

$$P_b \le \sum_{\mathbf{z},\,\hat{\mathbf{z}}\in C} \sum a(\mathbf{z},\hat{\mathbf{z}})P(\mathbf{z}) \prod_{n\in\eta} \left[1 + \frac{\| \underline{z}_n - \underline{\hat{z}}_n \|^2}{4N_0}\right]^{-1}, \tag{4.23}$$

where η is the set of n for which $\underline{z}_n \neq \underline{\hat{z}}_n$.

4.2.2. No Channel State Information

When no channel state information is available, the MLSE receiver will base its decisions on the following metric [29]

$$m(\mathbf{r},\mathbf{z}) = -\sum_{n=0}^{N-1} \| \mathbf{r}_n - \mathbf{z}_n \|^2. \tag{4.24}$$

Using Eq. (3.26), the pairwise error probability can be written as

$$P\{\mathbf{z} \to \hat{\mathbf{z}} \mid \mathbf{a}\} = \frac{1}{2} erfc\left[-\mu/\sigma\sqrt{2}\right]$$

$$\le \frac{1}{2}\exp\left[-\mu^2/2\sigma^2\right], \tag{4.25}$$

where

$$\mu = \sum_{n=0}^{N-1} (\| \underline{z}_n \|^2 - \| \underline{\hat{z}}_n \|^2)$$

$$- \sum_{n=0}^{N-1} a_n (\| \underline{z}_n - \underline{\hat{z}}_n \|^2 + \| \underline{z}_n \|^2 - \| \underline{\hat{z}}_n \|^2), \tag{4.26a}$$

and

$$\sigma^2 = 2N_0 \sum_{n=0}^{N-1} \| \underline{z}_n - \underline{\hat{z}}_n \|^2. \tag{4.26b}$$

We notice that averaging Eq. (4.25) over the random variable a is quite complicated, and a closed form for the pairwise error probability seems to be impossible to obtain. Eq. (4.25) can be rewritten in terms of a variable λ (Chernoff parameter) as:

$$P\{\mathbf{z} \rightarrow \hat{\mathbf{z}} \mid \mathbf{a}\} = \frac{1}{2}\exp\left[\frac{\sigma}{2}\lambda^2 + \mu\lambda\right]. \tag{4.27}$$

It is easy to show that optimizing Eq. (4.27) with respect to λ yields Eq. (4.25). Therefore, we can average Eq. (4.27) over the random variable a and then optimize the obtained result with respect to λ.

Rearranging terms in Eq. (4.27) and averaging over the random variable a, we get

$$P\{\mathbf{z} \rightarrow \hat{\mathbf{z}}\} = \frac{1}{2}\prod_{n\in\eta} \exp\left[N_0\lambda^2 \| \underline{z}_n - \underline{\hat{z}}_n \|^2 + \lambda(\| \underline{z}_n \|^2 - \| \underline{\hat{z}}_n \|^2)\right]$$

$$E_{a_n}\left\{\exp\left[-\lambda a_n(\| \underline{z}_n \|^2 - \| \underline{\hat{z}}_n \|^2 + \| \underline{z}_n - \underline{\hat{z}}_n \|^2)\right]\right\}, \tag{4.28}$$

where $E_{a_n}\{\,.\,\}$ represents the statistical average over the p.d.f of the random variable a_n. Therefore, an upper bound on the average bit error probability for the no channel state information case can be obtained using Eq. (4.20) with

$$\overline{D} = D^{\lambda^2 d^2(\mathbf{z},\,\hat{\mathbf{z}}) + \lambda(d^2(\mathbf{z},\,0) - d^2(\hat{\mathbf{z}},\,0))} E_a\left\{D^{-\lambda(d^2(\mathbf{z},\,\hat{\mathbf{z}}) + d^2(\mathbf{z},\,0) - d^2(\hat{\mathbf{z}},\,0))}\right\}, \tag{4.29}$$

where

$$d^2(\mathbf{z}, \hat{\mathbf{z}}) = \sum_{n\in\eta} \| \underline{z}_n - \underline{\hat{z}}_n \|^2. \tag{4.30}$$

For a Rayleigh fading channel, $\overline{D}$ can be derived as,

$$\bar{D} = D^{\lambda^2 d^2(\underline{z},\hat{\underline{z}}) + \lambda(d^2(\underline{z},0) - d^2(\hat{\underline{z}},0))} \prod_{n\in\eta} \left[1 - \frac{\sqrt{\pi}}{2}\zeta e^{\zeta^2/4} erfc\,(\zeta/2)\right], \tag{4.31}$$

where

$$\zeta = \lambda(\|\underline{z}_n - \hat{\underline{z}}_n\|^2 + \|\underline{z}_n\|^2 - \|\hat{\underline{z}}_n\|^2). \tag{4.32}$$

Using the following asymptotic expansion for $erfc\,(x)$,

$$erfc\,(x) \approx \frac{e^{-x^2}}{\sqrt{\pi}x}\left[1 - 1/2x^2\right], \tag{4.33}$$

and replacing λ by λ/N_0, $\bar{D}$ becomes

$$\bar{D} = 2D^{\lambda^2 d^2(\mathbf{z},\hat{\mathbf{z}}) + \lambda(d^2(\mathbf{z},0) - d^2(\hat{\mathbf{z}},0))} \prod_{n\in\eta} (1/\zeta^2). \tag{4.34}$$

The upper bound on P_b is obtained by first combining Eqs. (4.20) and (4.34), and then optimizing with respect to the parameter λ.

4.2.3. Indicating Parameters in a Fading Channel

Consider the upper bound on P_b given by (4.23). This upper bound consists of a sum of many terms, where each term is inversely proportional to the product of the squared branch distances along each error event path. However, at high signal-to-noise ratio, the upper bound on P_b is dominated by the term in the summation which has the smallest number of elements in η. This number represents the length of the shortest error event path, called L, and the upper bound on P_b becomes

$$P_b \leq \frac{a_d}{\beta^2\left(E_b/N_0\right)^L}, \tag{4.35}$$

where

$$\beta^2 = \prod_{n \in \eta} \left(\frac{\| \underline{z}_n - \underline{\hat{z}}_n \|^2}{4E_b} \right) \tag{4.36}$$

is a constant that depends on the distance structure of the code, and a_d indicates the number of paths of length L. The parameters a_d, β^2 and L can be used as indicating parameters for the evaluation of the performance of a given system. Based on these parameters, it is possible to get a good estimation for the performance. For example, trellis diagrams without parallel paths from one state to the next perform better in fading channels than the ones with parallel paths. Because parallel paths are known to be optimum for Additive White Gaussian Noise (AWGN) channels, where the performance of the system depends only on the minimum squared Euclidean distance along the trellis and not the length of the error event path [27]. Furthermore, when we have parallel paths the length of the shortest error event path is *one*.

We have seen in Chapter 3 that the quadrature pulse-overlapping modulation scheme can be decomposed into an encoder followed by a memoryless modulator. Furthermore, the trellis diagram of the QPOM encoder (example, Fig. 3.9) does not contain parallel paths from one state to the next. In fact, the length of the shortest error event path through the trellis is 2. Meaning that when ideal interleaving/de-interleaving is assumed, this scheme has a time diversity of $L = 2$ (if the all-zero path is taken as a reference path, any path leaving the all-zero path will merge into it for the first time at least after 2 state transitions, the path defined by the states 00, 10, 00 in Fig. 3.9 is such example). Therefore, using the new representation of the QPOM scheme, its performance over fading channels is expected to improve with respect to ideal coherent QPSK due to the structure of the QPOM trellis diagram.

4.3. PERFORMANCE OF QPOM SIGNALS IN RAYLEIGH FADING CHANNELS

In analyzing the performance of these signals, we consider the representation that has been discussed in Chapter 3, where the QPOM scheme is modeled as an encoder followed by a memoryless modulator. With the same assumptions of section 4.2, an upper bound on the bit error rate of these signals is obtained by using Eq. (4.20).

4.3.1 Linear QPOM Signals

The new representation of this scheme is shown in Fig. 3.1 and the trellis diagram of its encoder in Fig. 3.2. We assume that the two components of the linear QPOM signal are detected independently using a block diagram similar to the one given in Fig. 3.4. The transfer function $T(\bar{D}, N)$ of one of the components was derived and is given by Eq. (3.38). To be used in Rayleigh fading channels, we just replace $D^{d_i^2}$ by $\bar{D}$ defined by Eq. (4.22).

By doing so, the transfer function becomes:

$$T(\bar{D}, N) = \frac{ND_o^2}{1 - 0.5ND_1 - 0.5ND_2}, \tag{4.37}$$

where

$$D_0 = \left[1 + E_b/2N_0\right]^{-1}, \tag{4.38a}$$

$$D_1 = \left[1 + (1+\gamma)E_b/N_0\right]^{-1}, \tag{4.38b}$$

$$D_2 = \left[1 + (1-\gamma)E_b/N_0\right]^{-1}, \tag{4.38c}$$

and γ is a coefficient depending on the pulse shape $p(t)$ (Eq. 3.39). Taking the partial

derivative of (4.38) with respect to N and then combining it with Eq. (4.20), the upper bound on P_b becomes:

$$P_b \leq \frac{D_0^2}{2\left[1 - 0.5D_1 - 0.5D_2\right]^2}. \tag{4.39}$$

At high signal-to-noise ratio, higher-order terms can be neglected and the upper bound on P_b reduces to

$$P_b \leq 0.5\left[1 + E_b/2N_0\right]^{-2}, \tag{4.40}$$

indicating that the performance of linear QPOM signals is inversely proportional to the square of the signal-to-noise ratio E_b/N_0. Furthermore, we notice that for high E_b/N_0, the effect of the overlapping pulse shape on the performance is negligible. Hence, based on the new configuration of the linear QPOM scheme, it is possible to select bandwidth efficient pulse shapes without affecting the performance of the overall system. Fig. 4.2 shows the performance of this scheme over the Rayleigh fading channel. The simulation results are obtained for the double-interval overlapping raised-cosine pulse shape $(1 + cos(\pi t/T))/2$. We notice that the linear QPOM scheme offers better performance than conventional QPSK. The only drawback of this scheme is that its envelope is not constant.

When constant envelope signals are needed, a hard-limiter is used after the QPOM modulator. This hard-limiter introduces crosstalk between the in-phase and quadrature components of the transmitted signal. It was shown in Chapter 3 that optimum detection is possible only when the two components are treated simultaneously. Based on that discussion the performance of hard-limited QPOM signals in Rayleigh fading channels is analyzed in the following section.

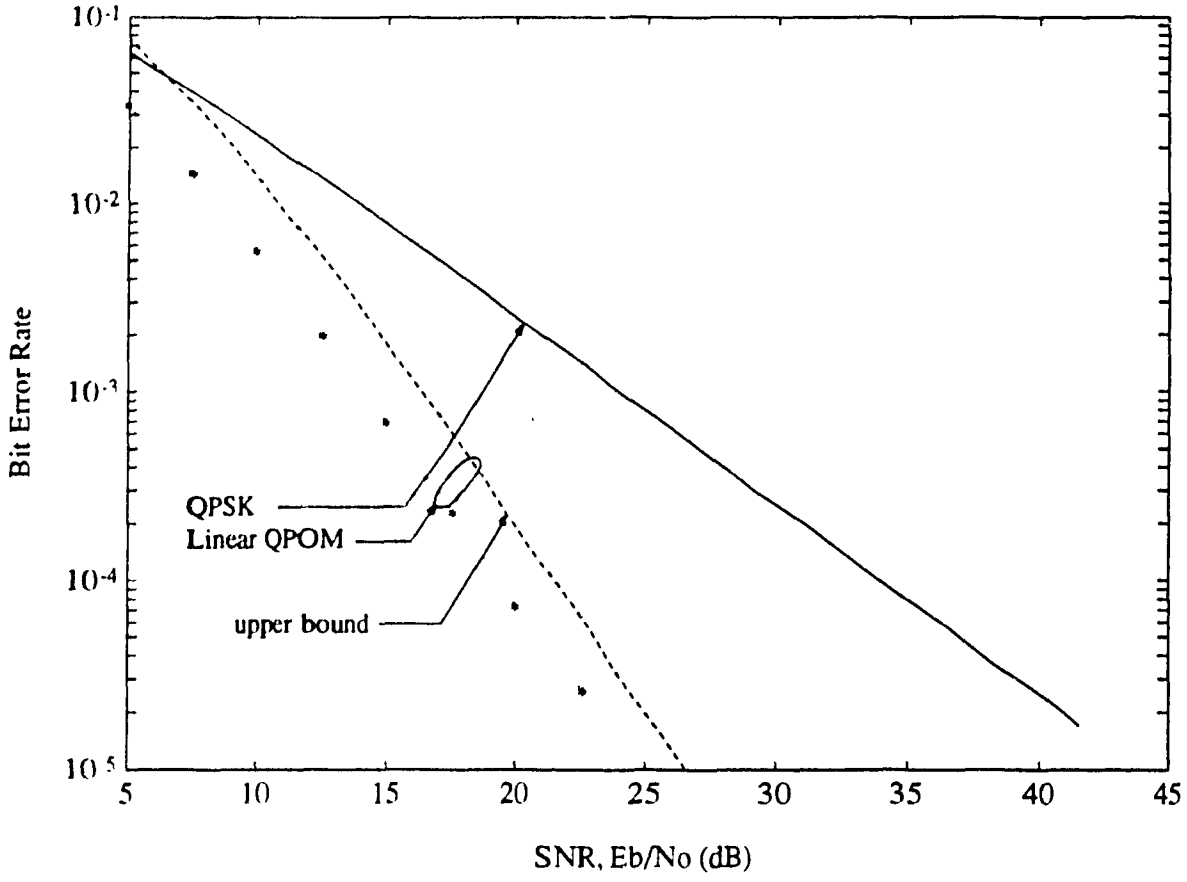

Fig. 4.2 – Performance of linear QPOM signals in Rayleigh fading channels

4.3.2. Performance of Hard-Limited QPOM Signals

Consider the new representation of the hard-limited QPOM scheme given in Fig. 3.8. This configuration represents the memory introduced by the overlapping pulse shape and the cross-correlation caused by the hard-limiter.

Assuming maximum likelihood sequence estimation, these signals are detected using the block diagram of the demodulator shown in Fig. 3.10. The MLSE processor bases its decision on the mapping rules of Table 3.3 and Eq. (4.16) (when the channel state information is available), or Eq. (4.24) otherwise.

The modified transfer function $T(\bar{D}, N)$ is obtained by combining Eq. (3.53) and Eq. (4.22), that is [45],

$$T(\bar{D}, N) = \frac{W_0 N + W_1 N^2}{1 - Q_0 N - Q_1 N^2}, \tag{4.41}$$

where

$$W_0 = 0.5D_3^2 + 0.5D_4^2 + D_3 D_4 + D_2^2,$$

$$W_1 = D_1 D_2 D_3 + D_2 D_3 D_5 + D_1 D_2 D_4 + D_2 D_4 D_5$$

$$- D_0 D_3 D_4 - 0.5D_0 D_4^2 - 0.5D_0 D_3^2 - 2D_2^3,$$

$$Q_0 = D_0 + 2D_2,$$

$$Q_1 = 0.5D_1^2 + 0.5D_5^2 + D_1 D_5 - 2D_0 D_2,$$

and in this case

$$D_0 = \left[1 + 2E_b/N_0\right]^{-1}, \quad D_1 = \left[1 + (1 + \beta_0)E_b/N_0\right]^{-1},$$

$$D_2 = \left[1 + E_b/N_0\right]^{-1}, \quad D_3 = \left[1 + (1-\beta_0)E_b/N_0\right]^{-1},$$

$$D_4 = \left[1 + (1-\beta_1)E_b/N_0\right]^{-1}, \quad D_5 = \left[1 + (1+\beta_1)E_b/N_0\right]^{-1}.$$

The upper bound on the average bit error probability of hard-limited QPOM signals then becomes:

$$P_b \le \frac{W_0(1+Q_1) + W_1(2-Q_0)}{4\left[1-Q_0-Q_1\right]^2} \tag{4.42}$$

The important point to be observed in Eq. (4.42) is that P_b depends on the baseband pulse shape used at the transmitter.

At high signal-to-noise ratios, higher-order terms in the expression of the average bit error probability can be neglected. Hence, Eq. (4.42) can be simplified to:

$$P_b \le 0.25\frac{(2-\beta_0-\beta_1)^2}{(1-\beta_0)^2(1-\beta_1)^2}\left[E_b/N_0\right]^{-2}$$

$$\approx 0.25\frac{(2-\beta_0-\beta_1)^2}{(1-\beta_0-\beta_1)^2}\left[E_b/N_0\right]^{-2}. \tag{4.43}$$

As we can see the variation of β_0 and β_1 does not affect the expression of the upper bound considerably. Therefore, it is possible to select a double-interval overlapping pulse shape which gives a transmitted signal with a compact spectrum and good performance. It is also noted that P_b varies inversely with the square of E_b/N_0. Fig. 4.3 [45] illustrates the performance of the hard-limited QPOM scheme. The simulation results are obtained for the double-interval overlapping pulse shape $(1 + cos(\pi t/T))/2$.

Recall the performance of conventional QPSK in a Rayleigh fading environment

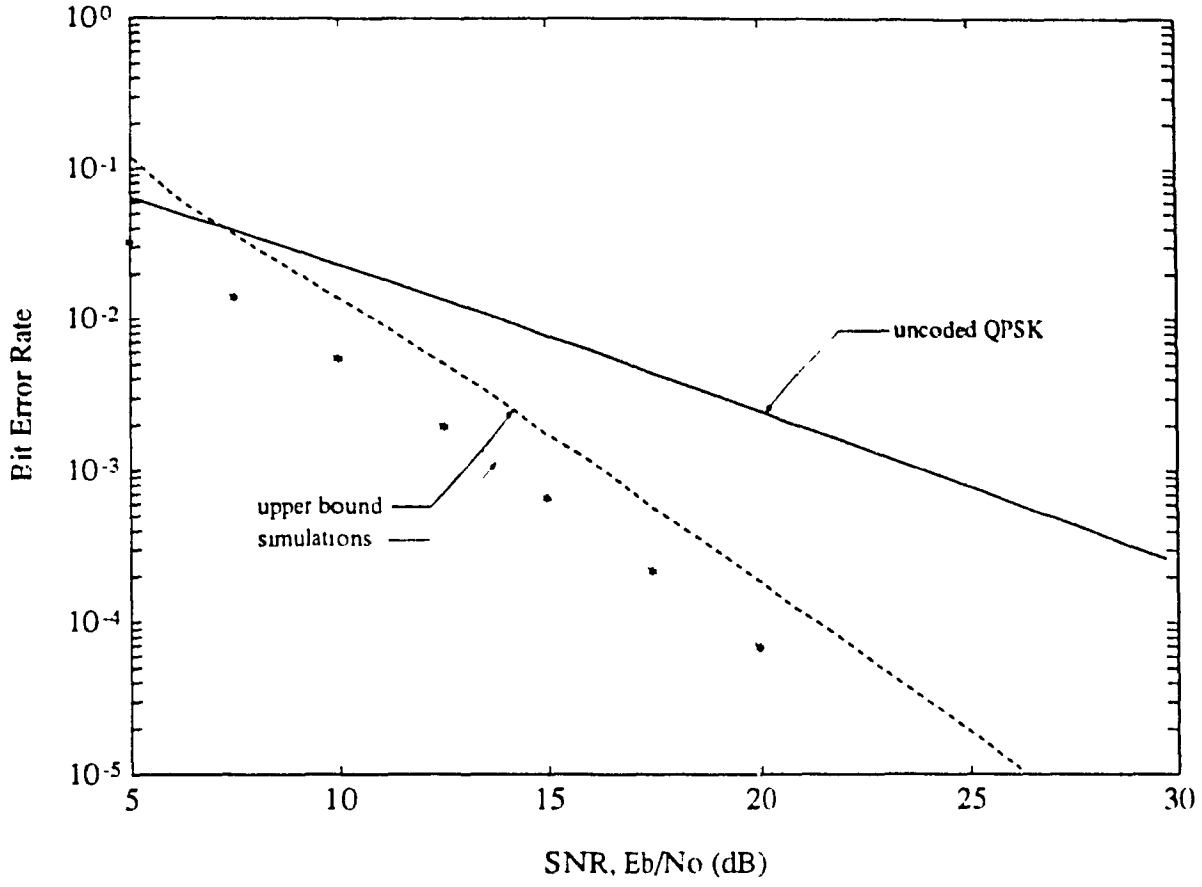

Fig. 4.3 – Performance of QPOM signals in Rayleigh fading channels

given in [24]. Since the QPSK modem is treated as a memoryless channel, channel state information is not required. Based on the same assumption of coherent detection, the probability of bit error for conventional QPSK in a Rayleigh fading environment (also the same for BPSK) is [24, Eq. (7.3.7)]

$$P_b = \frac{1}{2}\left[1 - \left[\frac{E_b/N_0}{1 + E_b/N_0}\right]^{1/2}\right]$$
$$\leq \frac{1}{4E_b/N_0}; \qquad \frac{E_b}{N_0} \gg 1. \tag{4.44}$$

Eq. (4.44) indicates that the error rate of conventional QPSK decreases only inversely with E_b/N_0, while the error rate of QPOM decreases inversely with the square of E_b/N_0 as shown by Eq. (4.43). The results in Fig. 4.3 clearly illustrate the superior performance of this detection scheme in Rayleigh fading channels.

The power spectral density of *hard–limited* QPOM signals can further be improved by introducing a delay of $T/2$ seconds in the baseband quadrature component of the transmitted signal. This delay does not affect the power spectrum of the modulated signal in a linear channel and hence both QPOM and Offset-QPOM spectra have the same shape. However, passing through a nonlinear (saturated) amplifier (or hard-limiter), Offset-QPOM signals exhibit a much lower spectral regrowth than QPOM signals [1]. Therefore, hard-limited Offset-QPOM schemes are more attractive. In the next section, the performance of hard-limited Offset-QPOM signal over the Rayleigh fading channel is analyzed.

4.3.3. Performance of Hard-Limited Offset-QPOM Signals

The trellis diagram of the hard-limited Offset-QPOM encoder is shown in Fig. 3.15. We notice that the shortest error event path of this encoder is of length 2. Therefore, when ideal interleaving/de-interleaving is assumed, this scheme exhibits a time diversity

of $L = 2$. Meaning that at high E_b/N_0, its performance is expected to vary inversely with the square of E_b/N_0 (same as hard-limited QPOM schemes).

An upper bound on the performance of this scheme can be obtained by first computing the squared product of Euclidean distances along the shortest path and then using Eq. (4.20). The squared product distance is easily obtained from the trellis diagram of Fig. 3.15. Eq. (4.20) can then be approximated by [39]

$$P_b \leq 0.25\left[1 + (1 - \beta_m)E_b/N_0\right]^{-2}, \tag{4.45}$$

where β_m is as defined in Chapter 3. We notice that this equation is comparable to (4.43). Both functions vary inversely with the square of E_b/N_0. Therefore, the performance of hard-limited Offset-QPOM is similar to that of QPOM, and choosing between the two schemes will only depend on the complexity and the spectral properties of each scheme. Fig. 4.4 gives the upper bound on P_b for both schemes. As we can see the performance is comparable. At high signal-to-noise ratios, hard-limited Offset-QPOM performs better than QPOM due to the structure of its trellis diagram.

So far we have considered the case of Rayleigh fading channels. In the event when there are fixed scatterers or signal reflectors in the medium, in addition to randomly moving scatterers, which is the usual case of land mobile satellite channels, the channel behaves as a *Rician* fading channel [59-61]. In the next section we present the effect of this kind of channel on the performance of hard-limited QPOM signals by means of computer simulation results.

4.4. PERFORMANCE OF HARD-LIMITED QPOM SIGNALS IN RICIAN FADING CHANNELS

The Rician fading model is based on the fast fading, shadowed mobile satellite communications channel model [60, 61], developed for application in the Canadian

Mobile Satellite Communication (MSAT) program.

The channel is modeled as an AWGN channel with a time varying fading process $\underline{a}$, representing the complex signal gain. This complex signal can be written as

$$\underline{a} = n_0 + e^{(n_1 + \mu_0)} + j\, n_2,$$

where n_0, n_1 and n_2 are three independent Gaussian random variables with zero mean and variance b_0^2, b_0^2 and d_0, respectively. The parameters μ_0, b_0^2 and d_0 determine the degree of shadowing. In our simulation, Light shadowed fading channel is used and the parameters of this channel are given in Table 4.1 [60]. Infinite interleaving/de-interleaving and ideal channel state information are assumed.

The results of our simulation for light shadowed fading channel are given in Fig. 4.5 [45]. The average bit error probability of the hard-limited QPOM scheme as well as ideal coherent QPSK are given as a function of unfaded E_b/N_0. As observed, the QPOM scheme has a better performance than the ideal coherent QPSK, without using any coding schemes. In fact the performance of this scheme is comparable to 4-state 8PSK TCM schemes [67, 68]. Therefore, by using this detection scheme, first, we can avoid the complexity of multi-level schemes and, second, we can transmit modulated signals with more compact spectrum.

Table 4.1
Channel Model Parameters for Light Shadowed Rician Fading Channel

b_0	μ_0	$\sqrt{d_0}$
0.158	0.115	0.115

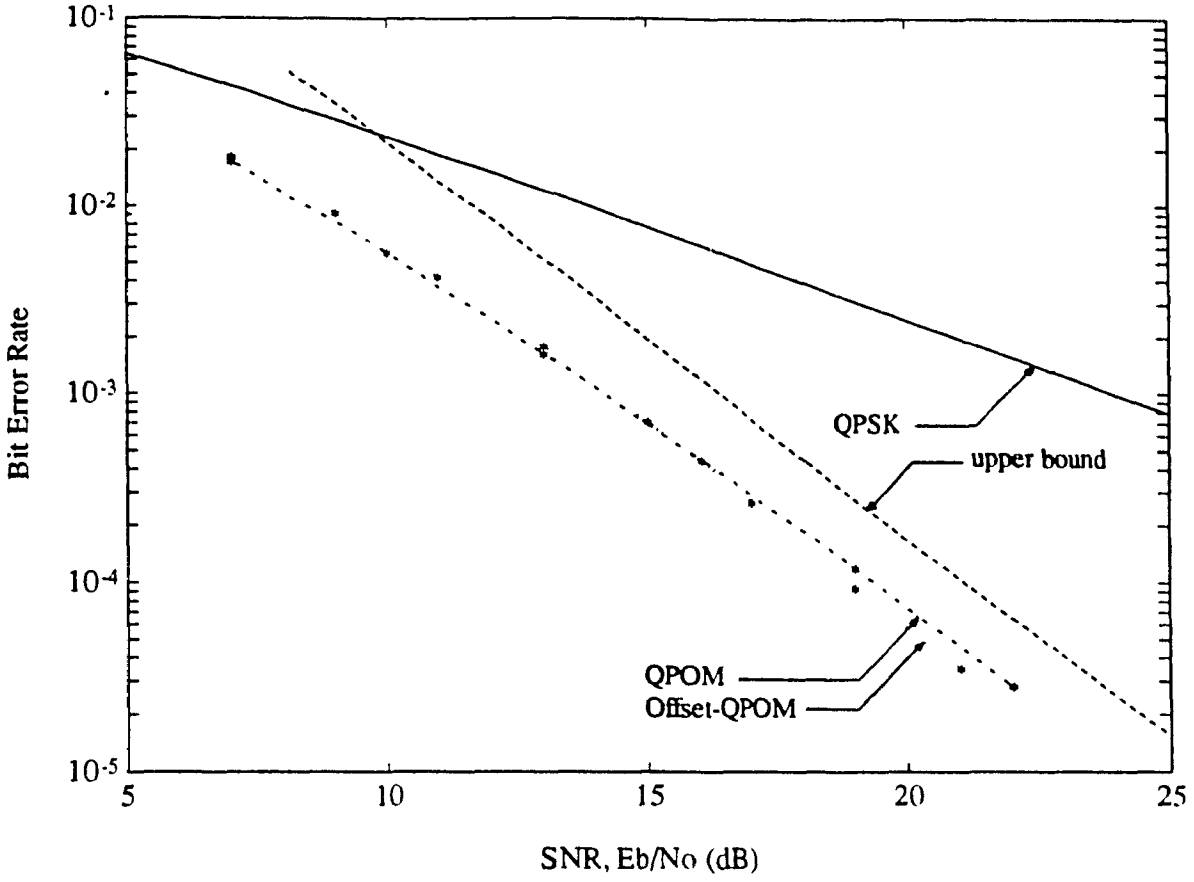

Fig. 4.4 – Performance comparison of hard-limited QPOM and hard-limited Offset-QPOM signals in Rayleigh fading channels.

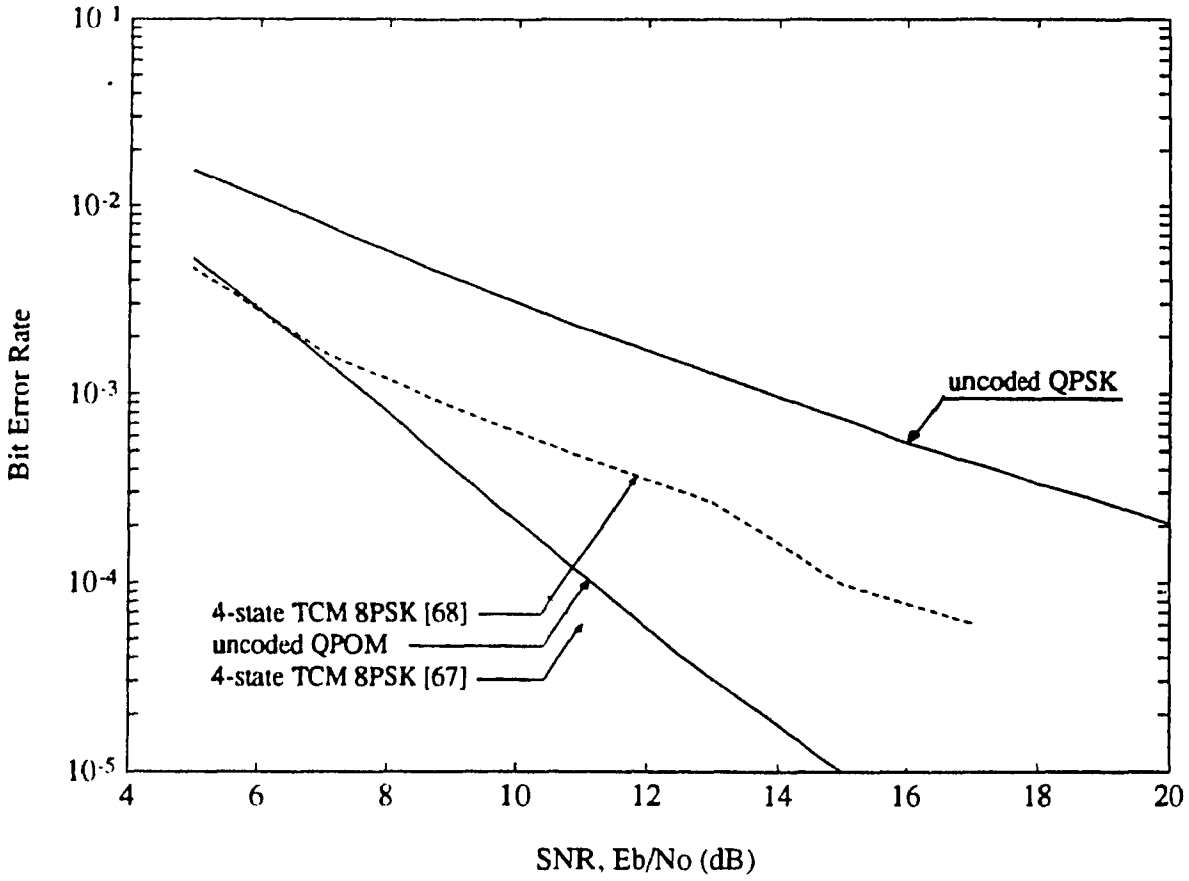

Fig. 4.5 – Performance comparison of hard-limited QPOM signals and 4-state 8PSK TCM in Rician fading channels.

4.5. PERFORMANCE COMPARISONS AND DISCUSSIONS

We have considered the average bit error probability of both QPOM and Offset-QPOM signals over fading channels. We observed that for both schemes, the bit error rate in Rayleigh fading channel decreases inversely with the square of E_b/N_0. It is also indicated that the performance of both schemes depends on the transmitted pulse shape. At high signal-to-noise ratio, the performance of hard-limited Offset-QPOM is better than that of hard-limited QPOM due to the structure of its trellis diagram and its signal constellations. Even though the detection of hard-limited Offset-QPOM signals is more complex, this scheme is still more attractive due to its spectral characteristics.

Trellis-coded modulation (TCM) schemes have recently received attention on mobile fading channels [29, 66-70]. When combined with interleaving, these schemes are known to give better performance in fading channels compared to the uncoded schemes. As was indicated in section 4.2.3, the design of strong TCM schemes is guided by parameters more than just the Euclidean distance [29]. It is shown that the length of the shortest error event path L and the product of branch distances along that path are primary criteria for strong TCM code designed on mobile fading channels. Results [29] showed that at high signal-to-noise ratio E_b/N_0, a code without parallel transitions has a better performance than a code with parallel transitions. The reason for this is that the code without parallel transitions contains more time diversity. This criteria has been used to design good codes for fading channels [29, 50, 67]. Note that in the hard-limited QPOM signals, error correcting coding is not included and the modulation is basically a 4PSK. However the memory caused by the double-interval overlapping baseband pulse shape behaves as an encoder. As previously discussed, the MLSE receiver is constructed by exploiting this inherent *non-redundant* coding structure. Its trellis does not have any parallel transitions. This makes it suitable to combat fading. Figs. 4.5 and 4.6 show the performance comparison of the hard-limited QPOM and some 4-state 8PSK TCM schemes in fading

channels. Code 1 (optimum in an AWGN channel) is a 4-state one with parallel transitions introduced in [68], and code 2 is also a 4-state code but without parallel transitions introduced in [67]. Fig. 4.6 shows that the hard-limited QPOM scheme has a similar performance as Code 2 and both outperform Code 1. This is explained by the fact that the hard-limited QPOM and Code 2 exhibit the same diversity $L = 2$ (represented by the shortest error event path), while Code 1 has a diversity of $L = 1$. As previously stated, larger diversity yields a better performance in fading channels. For $E_b/N_0 \leq 13\ dB$, the hard-limited QPOM outperforms both schemes.

Consider the fact that the hard-limited QPOM is actually a 4PSK scheme while code 2 is a 4-state 8PSK TCM scheme. It can be seen that the hard-limited QPOM scheme is less sensitive to phase error, and both schemes have the same complexity. For these reasons, hard-limited QPOM scheme is a better choice in practice for portable/mobile satellite communication systems.

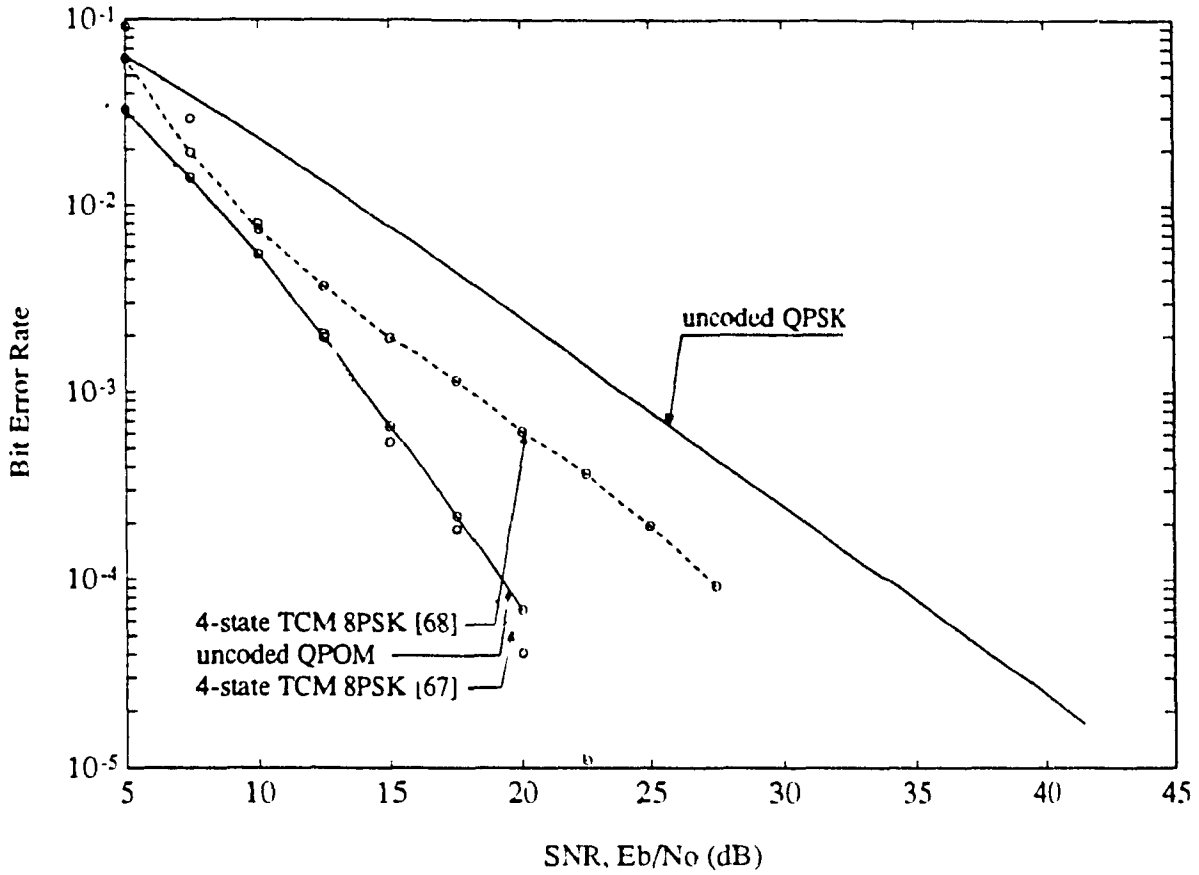

Fig. 4.6 – Performance comparison of hard-limited QPOM signals and 4-state 8PSK TCM in Rayleigh fading channels.

CHAPTER V

CODED QUADRATURE PULSE-OVERLAPPING MODULATED SIGNALS FOR FADING CHANNEL APPLICATIONS

In Chapter 4, we considered the performance of QPOM signals in fading channels. We observed that the new configuration of the QPOM scheme is suitable to fading channel applications. The use of this new configuration has improved the performance of the QPOM scheme considerably compared to ideal QPSK and this is achieved without any extra redundancy.

The performance of the QPOM scheme can further be improved by combining it with coding schemes. This Chapter presents the structure, performance, and realization of combining hard-limited QPOM schemes and convolutional codes for fading channel applications. As a direct result of the structural analysis, we provide solutions to the problem of how to optimize the combined coding-modulation for hard-limited QPOM schemes. The optimization criterion considered is based on maximizing the length of the shortest error event path and the product of the squared branch distances along that error event path for a given external convolutional code.

5.1. BACKGROUND

It is well known that combining coding and modulation improves the performance of the overall system. However, the combination of the two schemes depends on the structure of the modulation scheme. When coding is combined with a modulation scheme with memory, the optimum solution depends on the interaction between the memory of the outer code and that of the modulator. Moreover, this interaction will influence the overall performance of the signal-space code and the possible realizations for the

encoders that can produce it.

When the modulation scheme is divided into two stages: one stage with memory and one stage without memory, combining this modulation scheme with a convolutional code becomes a problem of concatenating two codes. This concatenation will not affect the operation (mapping rules) of the memoryless modulator.

An important characteristic in choosing the convolutional code is to reduce the number of states of the overall (concatenated) encoder. The number of states of the concatenated code is minimum when the output symbol of the convolutional code and the input symbol of the QPOM scheme have the same size. Since the QPOM scheme is a 4-level scheme (2 bits/symbol), the convolutional code of interest is a rate 1/2, convolutional code.

One way of describing a convolutional code is to give its generator matrix [24]. The convolutional code under consideration has the following generators:

$$g_1 = [g_{1,0}, \cdots, g_{1,v}] \tag{5.1a}$$

$$g_2 = [g_{2,0}, \cdots, g_{2,v}], \tag{5.1b}$$

where $g_{i,j}$ is a binary number taking the value 0 or 1 and v represents the total memory of the code. For each input bit a pair of bits are generated. For example, if the input of this code is a_n at time nT, then the output is

$$c_{0n} = \sum_{i=0}^{v} g_{1,i}\, a_{n-i} \tag{5.2a}$$

$$c_{1n} = \sum_{i=0}^{v} g_{2,i}\, a_{n-i}, \tag{5.2b}$$

which can be written as $c_{0n}c_{1n}$ and denoted by c_n. Depending on the values of $g_{i,j}$ and

a_n;

the symbol c_n can take one of the symbol values 00, 01, 10 or 11. In the following section we study the performance and the way of combining these convolutional codes and the hard-limited QPOM scheme.

5.2. DESIGN OF GOOD CODED HARD-LIMITED QPOM SCHEMES

The system under consideration is shown in Fig. 5.1. As we can see the concatenation of the two codes will not affect the operation of the memoryless modulator. The hard-limited QPOM encoder is a rate 2/4 linear encoder and is given in Fig. 3.9. When this encoder is concatenated with the convolutional code having the generators of Eqs. (5.1a, b), the obtained code is also a convolutional code with rate 1/4.

When the output symbol of the external convolutional code is as given by Eqs. (5.2a, b), then from Fig. 3.9 and Table 3.3 the output of the concatenated code (denoted by $cc_n = cc_{0n}cc_{1n}cc_{2n}cc_{3n}$) can be written in terms of c_n as

$$cc_n = c_n c_{n-1}.$$

Therefore, the concatenated code can be seen as two convolutional codes (identical to the external convolutional code) in parallel. The first convolutional code having as input a_n, and the second convolutional code having as input a_{n-1}.

The generators of the concatenated code can be then written as [81]:

$$g_1 = [g_{1,0}, \ldots, g_{1,v}, 0] \tag{5.3a}$$

$$g_2 = [g_{2,0}, \ldots, g_{2,v}, 0] \tag{5.3b}$$

$$g_3 = [0, g_{1,0}, \ldots, g_{1,v}] \tag{5.3c}$$

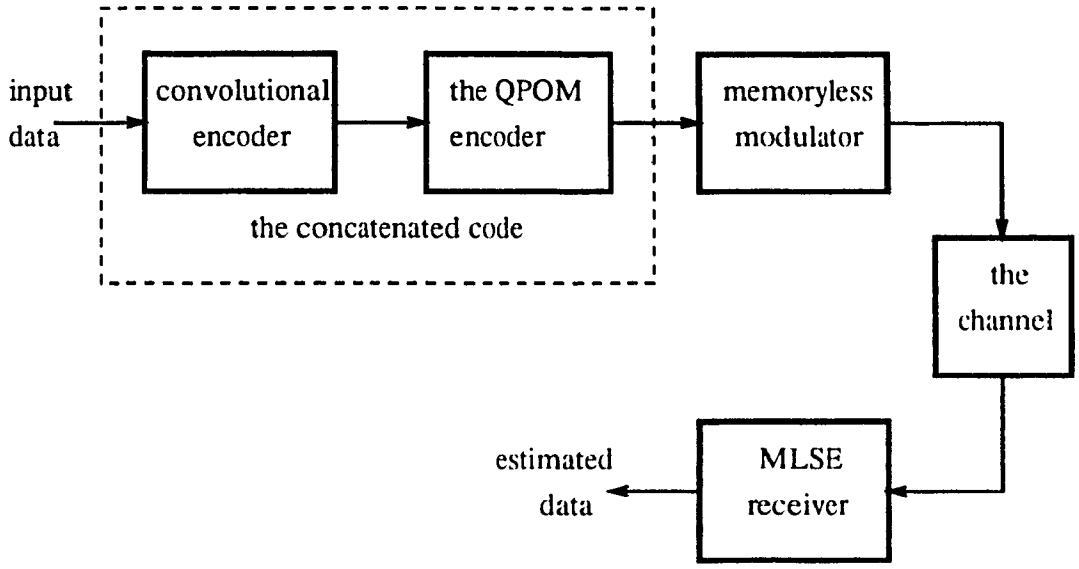

Fig. 5.1 - The block diagram of coded QPOM schemes.

$$g_4 = [0, g_{2,0}, \ldots, g_{2,\nu}]. \tag{5.3d}$$

As we can see the concatenated code is completely defined once the external convolutional code is known.

From Eq. (5.3), we notice that the memory of the original convolutional code has been shifted by one. Therefore, the total memory of the concatenated code is $\nu + 1$. The number of states of this code is then *two* times the number of states of the external convolutional code. Usually, when two codes of ν_1 and ν_2 states are concatenated, the obtained code has a total of $\nu_1\nu_2$ states. Therefore, when the external convolutional code is properly chosen the number of states of the concatenated code can be reduced. In our case the number states has been reduced by a factor of *two*. This reduction in number of states will reduce the complexity of the MLSE receiver without affecting its performance.

The above discussion shows that if the external convolutional code is defined by its trellis diagram, then the trellis diagram of the concatenated code can be constructed easily. Thus making the selection of codes much simpler. This method is used in the following sections to represent the concatenated code.

The convolutional code will reduce the connectivity of the inner trellis (the trellis of the linear encoder alone). The number of branches leaving (or merging into) each state is reduced from *four* to *two*. The next question is how to choose the convolutional code in such a way that the performance of the entire system is optimized. To answer this question, we start with 2-state convolutional codes.

5.2.1. Rate 1/2, 2-State Convolutional Codes

Consider the general trellis diagram of a rate 1/2 2-state convolutional code given in Fig. 5.2. The output of the code is defined by the set of symbols $\{c_0, c_1, c_2, c_3\}$. These symbols are distinct and are chosen from the set of symbols {00, 01, 10, 11}. From the

previous discussion, the concatenated code should have a total of 4 states. Fig. 5.3 shows the trellis diagram of the concatenated code. We notice that the output of this code is given as a function of the output of the convolutional code. Therefore, with an appropriate choice of the symbols $\{c_0, c_1, c_2, c_3\}$, we can control the output of the concatenated code in such a way that the performance of the coded scheme is improved.

Consider the performance of a memory scheme in fading channels. In Chapter 4 it was shown that the bit error rate is a function of the length of the shortest error event path and the product of the squared branch distances along that path. These parameters were enough to give a good approximation for the upper bound on P_b. Here, we use these parameters as indicating parameters in designing convolutional codes and help choose its output symbols.

From the trellis diagram of Fig. 5.3, we notice that the shortest error event path is of length 3. This provides an increase by one from the initial encoder. As seen from the figure, L=3 is the maximum achievable time diversity for this 4-state trellis diagram. Therefore, the design of the convolutional code will be based on the selection of the set of symbols $\{c_0, c_1, c_2, c_3\}$.

The Euclidean distance between the output symbols of the hard-limited QPOM encoder varies with the Hamming distance. When the Hamming distance is high the Euclidean distance is also high. This property is used in selecting the output symbols of the convolutional code. When the all-zero path is taken as a reference, the Euclidean product distance along the shortest error event path is a function of the following symbols

$$c_1c_0, \quad c_1c_2, \quad c_0c_2.$$

We start by defining the all zero path of the code. For linear codes, when the code is at state '00' and the input is '0', the output will be the all zero symbol. Hence,

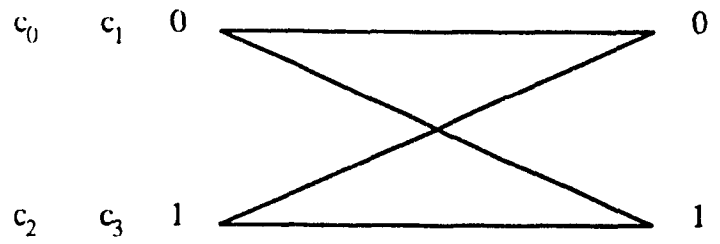

Fig. 5.2 - The general trellis diagram of a rate 1/2, 2-state convolutional code.

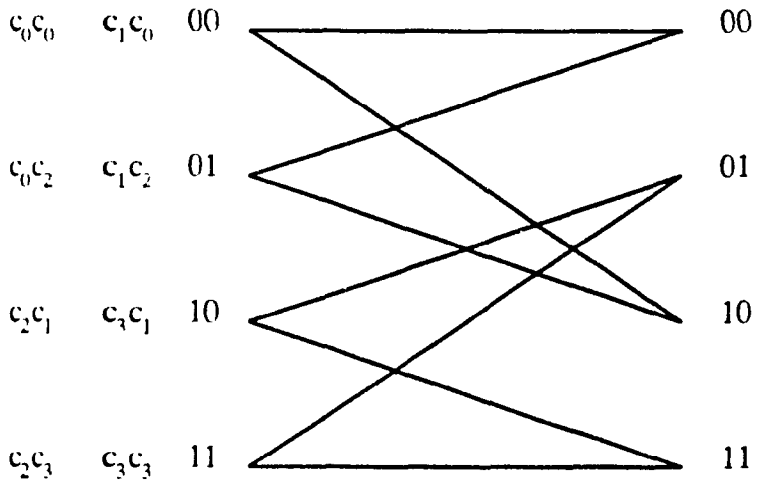

Fig. 5.3 - The trellis diagram of the code resulting from the concatenation of the code of Fig. 5.2 and the QPOM encoder.

$$c_0 = 00.$$

In order to choose the rest of the symbols, we have to analyze the expression of the product β^2 and at the same time keep a balanced convolutional encoder. This last property ensures that no state is relatively weaker (or stronger) than others seen from the Euclidean distance distribution.

Consider the first subset of the trellis diagram of the QPOM encoder:

$$A_0 = \{0, 4, 8, 12\}.$$

After concatenation the first subset of the obtained code must be $\{0, 4\}$, $\{0, 8\}$, or $\{0, 12\}$. It is easy to show that if this subset is $\{0, 12\}$, the obtained code has a UEP otherwise the code is nonlinear. From Appendix A, we notice that the weight profile of the QPOM encoder is a function of at most two distances. When the code is nonlinear, depending on the reference subset the weight profile becomes a function of only one of the distances. If we consider all possible states, the minimum distance of the code will be a function of the minimum of the two distances. Therefore for this particular case, the convolutional code resulting in a nonlinear concatenated code is not an optimum code.

The first subset of the concatenated code then should be $\{0, 12\}$,
that is,

$$c_1 = 11.$$

The two other symbols c_2 and c_3 are easily defined, which gives the convolutional codes of Table 5.1.

Table 5.1
2-State Convolutional Codes for Hard-Limited QPOM Schemes

Code	c_0	c_1	c_2	c_3
code 1	00	11	01	10
code 2	00	11	10	01

We notice that only two codes are selected for the hard-limited QPOM schemes. Compared to QPSK, we can say that a good code for the QPSK scheme is not necessarily good for the hard-limited QPOM scheme. This is due to the interaction between the memory of the QPOM scheme and the convolutional code.

By analyzing the concatenation of the codes of Table 5.1 and the hard-limited QPOM encoder, it is found that the two concatenated codes have the same transfer function. In other words they all have the same performance.

Consider the concatenation of code 1 and the hard-limited QPOM encoder. The trellis diagram of the obtained code is shown in Fig. 5.4. The modified transfer function of this code can be derived by writing the state equations and then using Eq. (3.37). By doing so we get:

$$T(\bar{D}, N) = \frac{0.25ND^{\alpha_2}(D^{\alpha_1} + D^{\alpha_5})(D^{\alpha_3} + D^{\alpha_4})}{1 - ND^{\alpha_2} - 0.25N(D^{\alpha_1} + D^{\alpha_5})^2}, \tag{5.4}$$

where in this case

$$\begin{aligned} &\alpha_0 = 4, \qquad \alpha_1 = 2(1 + \beta_0), \qquad \alpha_3 = 2(1 - \beta_0), \\ &\alpha_2 = 2, \qquad \alpha_5 = 2(1 + \beta_1), \qquad \alpha_4 = 2(1 - \beta_1). \end{aligned} \tag{5.5}$$

The normalized squared Euclidean distance of this scheme is given by

$$d^2_{\min} = 2(3 + \beta_1 - \beta_0).$$

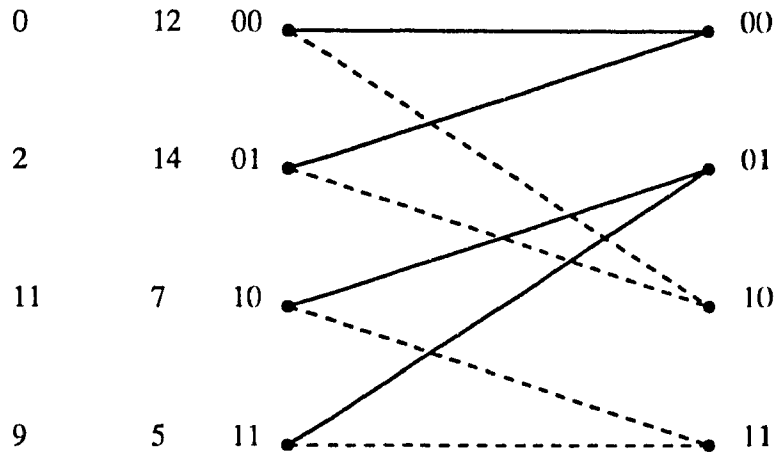

Fig. 5.4 - The trellis diagram of the code resulting from the concatenation of code 1 and the QPOM encoder.

We notice that the performance is dependent on the pulse shape $p(t)$. By a proper choice of $p(t)$, both β_0 and β_1 become close to 0.5 and a coding gain up to 1.76 dB over uncoded BPSK under AWGN conditions can be achieved, which is comparable to 2-state coded QPSK. However, the complexity of 2-state coded QPSK is less than that of coded hard-limited QPOM.

Over Rayleigh fading channels, an upper bound on the average bit error probability of this system is easily obtained using (4.20),

$$P_b \le \frac{0.125D_2(D_1 + D_5)(D_3 + D_4)}{\left[1 - D_2 - 0.25(D_1 + D_5)^2\right]^2}, \tag{5.6}$$

with

$$D_i = \left[1 + \alpha_i E_b/4N_0\right]^{-1}.$$

At high signal-to-noise ratio, the upper bound on P_b can be approximated by

$$P_b \le 0.125D_2D_3D_5 \approx \frac{1}{(1-\beta_0)(1+\beta_1)}\left[\frac{E_b}{N_0}\right]^{-3}, \quad \frac{E_b}{N_0} \gg 1, \tag{5.7}$$

where β_0 and β_1 are given by (3.52a, b), respectively, and are functions of the pulse shape $p(t)$. From Fig. 5.5 [81], we notice that this coded scheme outperforms the uncoded QPOM by about 3 dB at a bit error rate of 10^{-4}. However, comparing it to the 4-state convolutionally coded QPSK (the two schemes have the same number of states), it is seen that the performance is about 1 dB worse. This dB difference can be reduced by choosing the appropriate pulse shape, for which β_0 and β_1 are close to 0.5.

Further improvement in the performance of convolutionally coded QPOM can be achieved by increasing the number of states of the convolutional code.

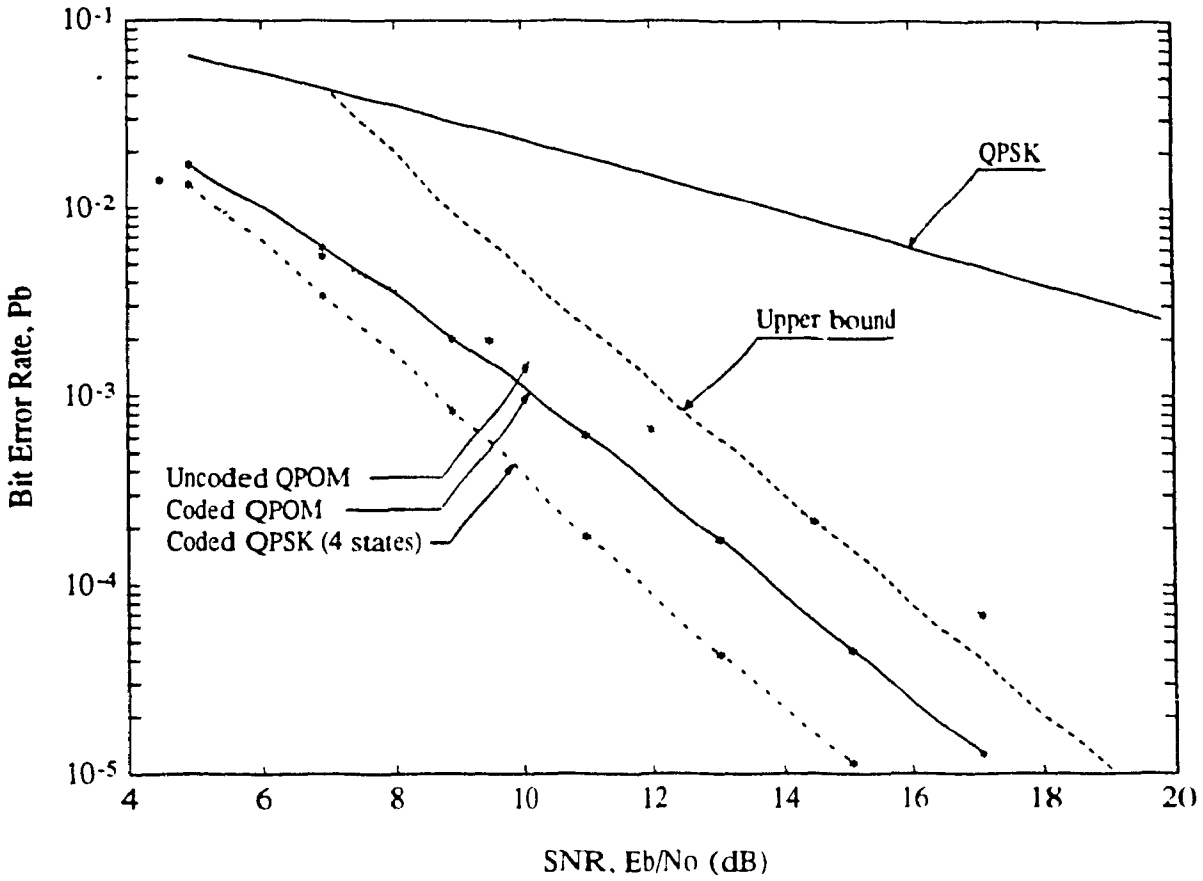

Fig. 5.5 – Performance of coded QPOM schemes in Rayleigh fading channels 2-state convolutional codes).

In the following, 4-state, rate 1/2 convolutional codes are considered.

5.2.2. Rate 1/2, 4-State Convolutional Codes

A rate 1/2, 4-state convolutional code can also be represented by its trellis diagram as shown in Fig. 5.6. In this figure, c_0, c_1, c_2, c_3, c_4, c_5, c_6, and c_7 represent the output symbols of the code. These symbols are chosen from the set of symbols {00, 01, 10, 11}.

When this code is concatenated with the hard-limited QPOM encoder, the code having the trellis diagram of Fig. 5.7 is obtained. Its possible outputs are expressed in terms of the possible outputs of the external convolutional code. This code has a total of 8 states and the length of the shortest error event path is 4.

In designing the optimum code, we consider the parameters used in section 5.2.1, namely, maximizing the distance between signals leaving the same state, the distance between signals merging into the same state, and the product of the squared branch distances along the shortest error event path.

From Fig. 5.7, we notice that when the all-zero path is taken as a reference, the product distance along the shortest error event path is a function of the following symbols

$$c_1c_0, \quad c_2c_1, \quad c_2c_4, \quad c_0c_2.$$

Assuming that the all zero path is defined by the symbol c_0c_0, i.e.,

$$c_0 = 00,$$

then from the discussion of the previous section concerning the linearity of the concatenated code, the two symbols c_1 and c_2 should have the following values:

$$c_1 = 11, \; c_2 = 11.$$

By doing so we avoid the presence of the distance $2(1-\beta_0)$ (always smaller than or equal to one) in the expression of β^2. The symbol c_4 will take one of two values

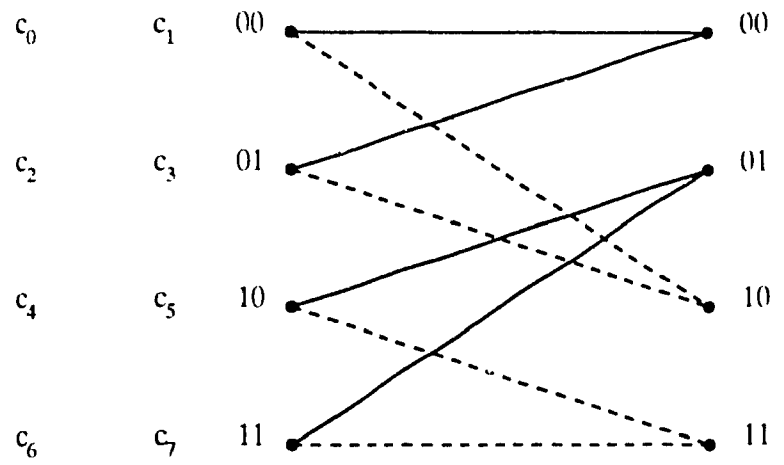

Fig. 5.6 - The trellis diagram of a rate 1/2, 4-state convolutional code.

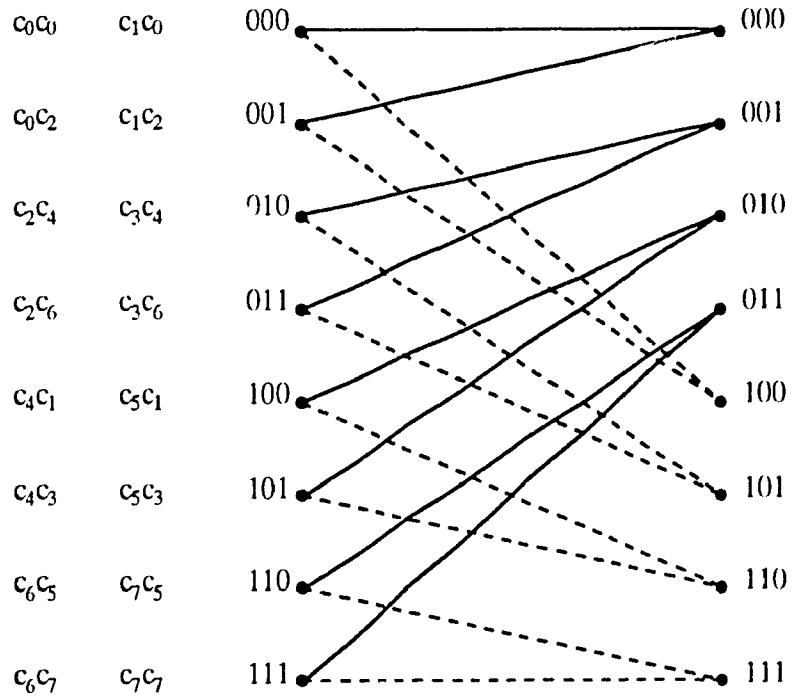

Fig. 5.7 - The trellis diagram of the code resulting from the concatenation of the code of Fig. 5.6 and the QPOM encoder.

$$c_4 = 01 \ \ or \ \ 10.$$

The selection of the rest of the symbols follows easily. This leads to the convolutional codes given in Table 5.2.

The trellis diagram of the code resulting from the concatenation of code 1 and the hard-limited QPOM encoder is given in Fig. 5.8. Its modified transfer function is derived following the procedure used in Chapter 3,

$$T(D,N) = \frac{0.25ND^{2\alpha_2}(D^{\alpha_1} + D^{\alpha_5})^2}{1 - ND^{\alpha_2} - 0.25N(D^{\alpha_3} + D^{\alpha_4})^2 - 0.25N(D^{\alpha_1} + D^{\alpha_5})^2}, \tag{5.8}$$

where α_i are given by Eq. (5.5).

The minimum normalized squared Euclidean distance of this code is given by

$$d^2_{min} = 4(2 + \beta_{min}), \tag{5.9}$$

where

$$\beta_{min} = min(\beta_0, \beta_1).$$

Table 5.2
4-State Convolutional Codes for Hard-Limited QPOM Schemes

Code	c_0	c_1	c_2	c_3	c_4	c_5	c_6	c_7
code 1	00	11	11	00	01	10	10	01
code 2	00	11	11	00	10	01	01	10

In the AWGN channel, the performance of the system is upper bounded by:

$$P_b \le \frac{1}{2} erfc\left[\left[(2 + \beta_{min})E_b/N_0\right]^{1/2}\right]. \tag{5.10}$$

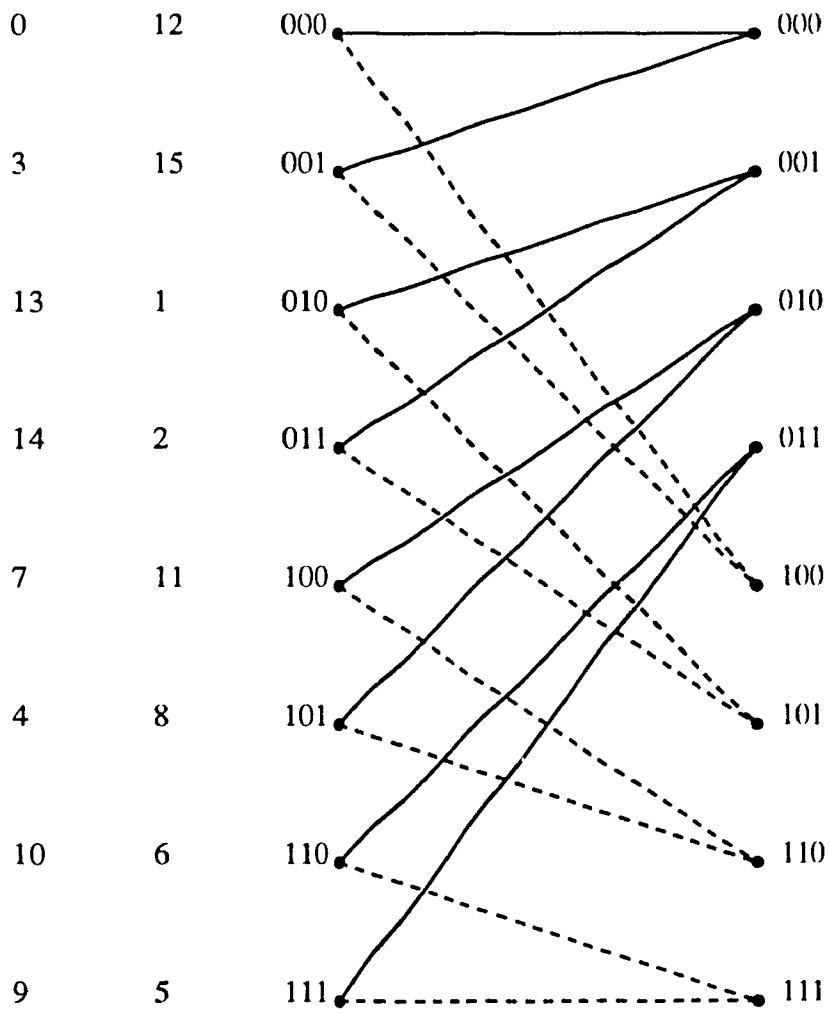

Fig. 5.8 - The trellis diagram of the code resulting from the concatenation of code 1 and the QPOM encoder.

Compared to uncoded BPSK, a coding gain of $10log(2 + \beta_{min})$ dB is achieved. Since $\beta_{min} \leq 0.5$, the maximum coding gain obtained with this scheme is 3.98 dB which is comparable to that of 4-state coded QPSK. This justifies once more the results of Chapter 3, where the performance in AWGN channels is a function of the distance between set points and completely independent of the structure of the trellis diagram of the code.

Over fading channels, the structure of the trellis diagram is important. Consider the Rayleigh fading channel, an upper bound on the average bit error probability of the system is given by:

$$P_b \leq \frac{0.125D_2^2(D_1 + D_5)^2}{\left[1 - D_2 - 0.25(D_3 + D_4)^2 - 0.25(D_1 + D_5)^2\right]^2}, \tag{5.11}$$

which at high signal-to-noise ratio can be approximated as:

$$P_b \leq \frac{8(\alpha_1 + \alpha_5)^2}{(\alpha_1\alpha_5)^2}\left[\frac{E_b}{N_0}\right]^{-4}, \quad \frac{E_b}{N_0} \gg 1 \tag{5.12}$$

We notice that by changing α_1 and α_5, the upper bound on P_b does not change much. Fig. 5.9 gives the performance of this coded scheme. As indicated, more coding gain is obtained compared to the 2-state code. It is observed that coded hard-limited QPOM outperforms 8-state coded QPSK (both schemes have the same complexity).

5.3. DESIGN OF GOOD CODED HARD-LIMITED OFFSET-QPOM SCHEMES

The hard-limited Offset-QPOM encoder is a linear encoder with rate 2/5 as shown in Fig. 3.14. When this code is concatenated with a rate 1/2, convolutional code, the obtained code is also a convolutional code with rate 1/5.

Consider the convolutional code having as output c_n defined by Eq. (5.2).

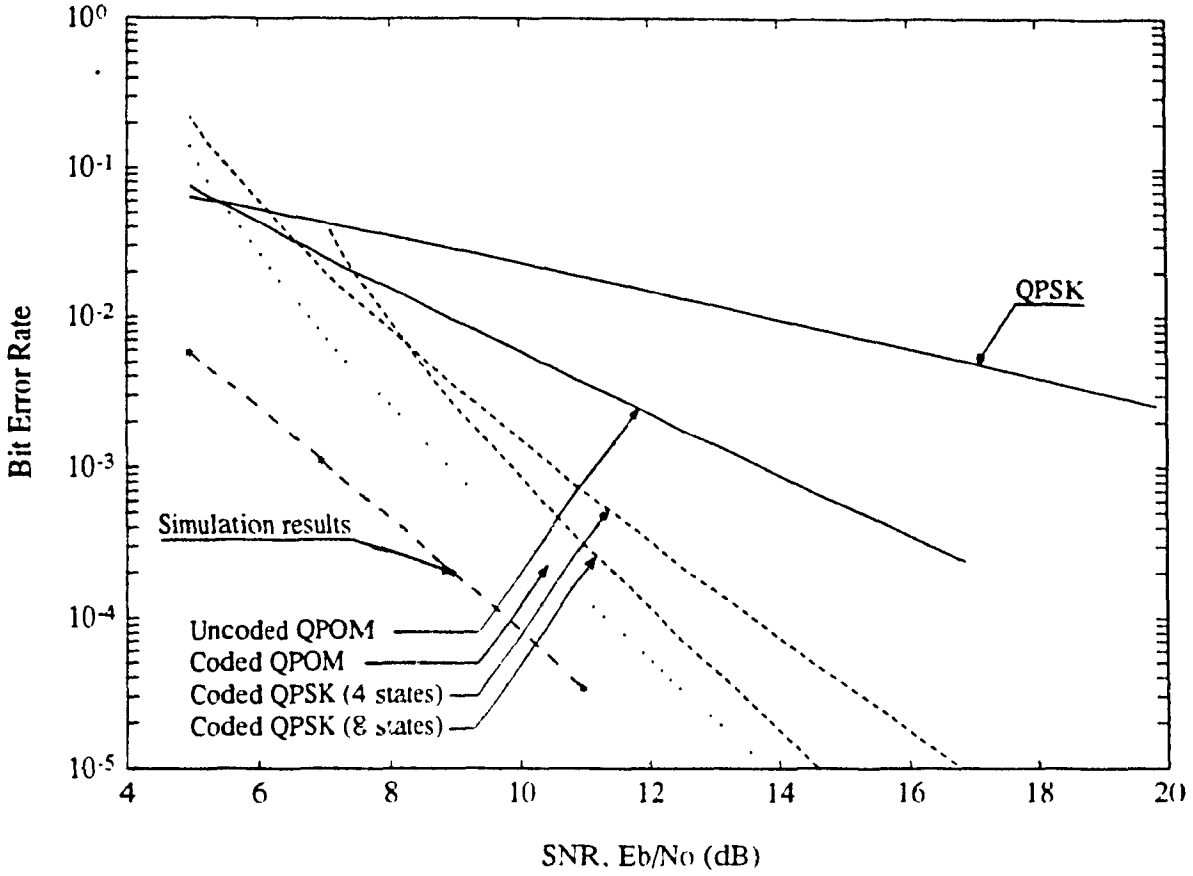

Fig. 5.9 – Performance of coded QPOM schemes in Rayleigh fading channels (4-state convolutional codes).

From Fig. 3.14 and Table 3.5, the output of the concatenated code can be expressed in terms of c_n as:

$$cc_n = c_n c_{n-1} c_{(n-2)l},$$

where $c_{(n-2)l}$ denotes the least significant bit of the symbol c_{n-2}. The trellis diagram of the concatenated code can then be derived from the trellis diagram of the external convolutional code.

The generators of the concatenated code can then be written as:

$$g_1 = [g_{1,0}, \ldots, g_{1,\nu}, 0, 0] \tag{5.13a}$$

$$g_2 = [g_{2,0}, \ldots, g_{2,\nu}, 0, 0] \tag{5.13b}$$

$$g_3 = [0, g_{1,0}, \ldots, g_{1,\nu}, 0] \tag{5.13c}$$

$$g_4 = [0, g_{2,0}, \ldots, g_{2,\nu}, 0] \tag{5.13d}$$

$$g_5 = [0, 0, g_{2,0}, \ldots, g_{2,\nu}]. \tag{5.13e}$$

We can see in this case that the memory of the original convolutional code has been shifted by *two*. The total memory of this code is then $\nu + 2$. Therefore, the number of states of the concatenated code is *four* times the number of states of the external convolutional code. This gives a reduction in the state space by a factor of *two*. This reduction in number of states is similar to the one obtained for the hard-limited QPOM scheme.

In order to be able to design these codes, we consider some particular cases where we have to fix the total memory ν.

5.3.1. Rate 1/2, 2-State Convolutional Codes

The general trellis diagram of a rate 1/2, 2-state convolutional code is given in Fig. 5.2. When this code is concatenated with the hard-limited Offset-QPOM encoder, the

code having the trellis diagram of Fig. 5.10 is obtained. As we can see the output is given as a function of the output of the convolutional code. Therefore, following the same procedure used in section 5.2 we can design convolutional codes suitable to the hard-limited Offset-QPOM scheme [72].

In Fig. 5.10, c_{il} represents the least significant bit of the symbol c_i. The all zero path of the code is defined by the symbol c_0. Hence,

$$c_0 = 00, \rightarrow c_{0l} = 0.$$

From the same figure, we notice that the only choice for c_{2l} is

$$c_{2l} = 1,$$

i.e., c_2 can take the value 01 or 11. Because if $c_{2l} = 0$ then the obtained code is a catastrophic code. The product of the squared distances along the shortest error event path is a function of the following symbols:

$$c_1c_0c_{0l}, \quad c_0c_0c_{2l}, \quad c_0c_2c_{1l}, \quad c_2c_1c_{0l}.$$

We notice from Fig. 5.10 that if $c_{1l} = 1$ than c_{3l} has to be 0 and vis versa. Using these restrictions, the following code is obtained:

$$g_1 = [1\ 0]$$

$$g_2 = [1\ 1]$$

Now consider the case when $c_{2l} = 0$, then the 2-state convolutional code will have the following generators:

$$g_1 = [g_{1,0}, g_{1,1}], \qquad g_2 = [g_{2,0}, 0].$$

This means that the least significant bit of the output symbol is independent of the

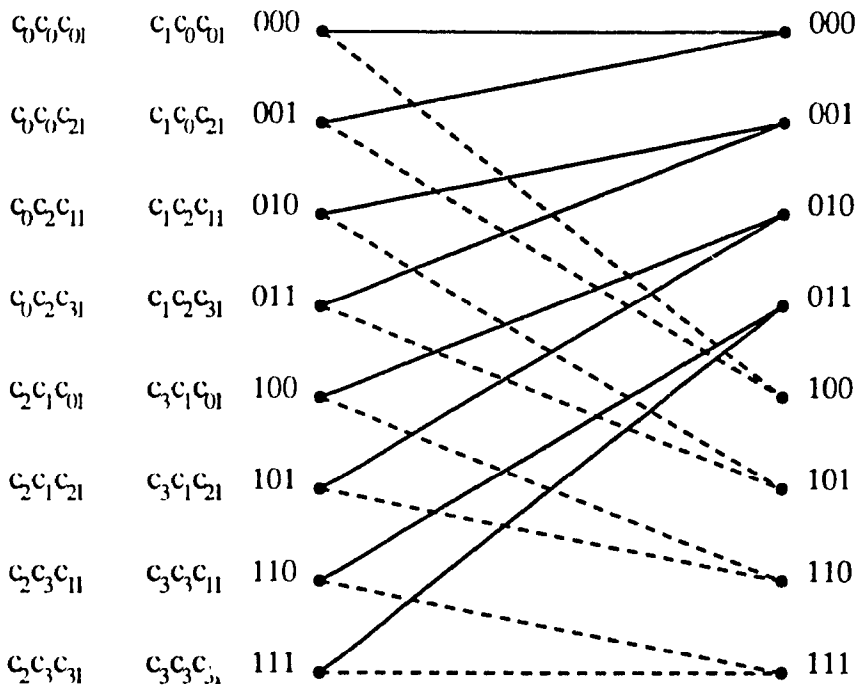

Fig. 5.10 - The trellis diagram of the equivalent code resulting from the concatenation of the code of Fig. 5.2 and the Offset-QPOM encoder.

memory of the code. From Eq. (5.3), the generators of the concatenated code can be written as

$$g_1 = [g_{1,0}, g_{1,1}, 0], \qquad g_2 = [g_{2,0}, 0, 0],$$
$$g_3 = [0, g_{1,0}, g_{1,1}], \qquad g_4 = [0, g_{2,0}, 0],$$
$$g_5 = [0, 0, g_{2,0}]. \tag{5.14}$$

As we can see the memory of the concatenated code has been reduced from 8 to 4. In this case the trellis diagram of Fig. 5.10 becomes a 4-state trellis diagram. Therefore, the complexity of the concatenated code is reduced by a factor of 4. The following convolutional code offers such structure:

$$g_1 = [1\ 1]$$

$$g_2 = [1\ 0]$$

We have considered the two different codes. The results are illustrated in Fig. 5.11. Code 1 is the code resulting to an 8-state Offset-QPOM scheme and Code 2 to a 4-state coded scheme. It is observed that both codes offer comparable results. Therefore, it is better to consider 2-state convolutional codes satisfying Eq. (5.14).

Further improvement in the performance of convolutionally coded Offset-QPOM can be achieved by increasing the number of states of the convolutional. In the following, 4-state, rate 1/2 convolutional codes are considered. These codes are combined with the linear encoder of the Offset-QPOM scheme.

5.3.2. Rate 1/2 4-State Convolutional Codes

A 4-state, rate 1/2 convolutional code can also be represented by its trellis diagram as shown in Fig. 5.6. When this code is concatenated with the hard-limited Offset-QPOM encoder, the concatenated code is also a convolutional code.

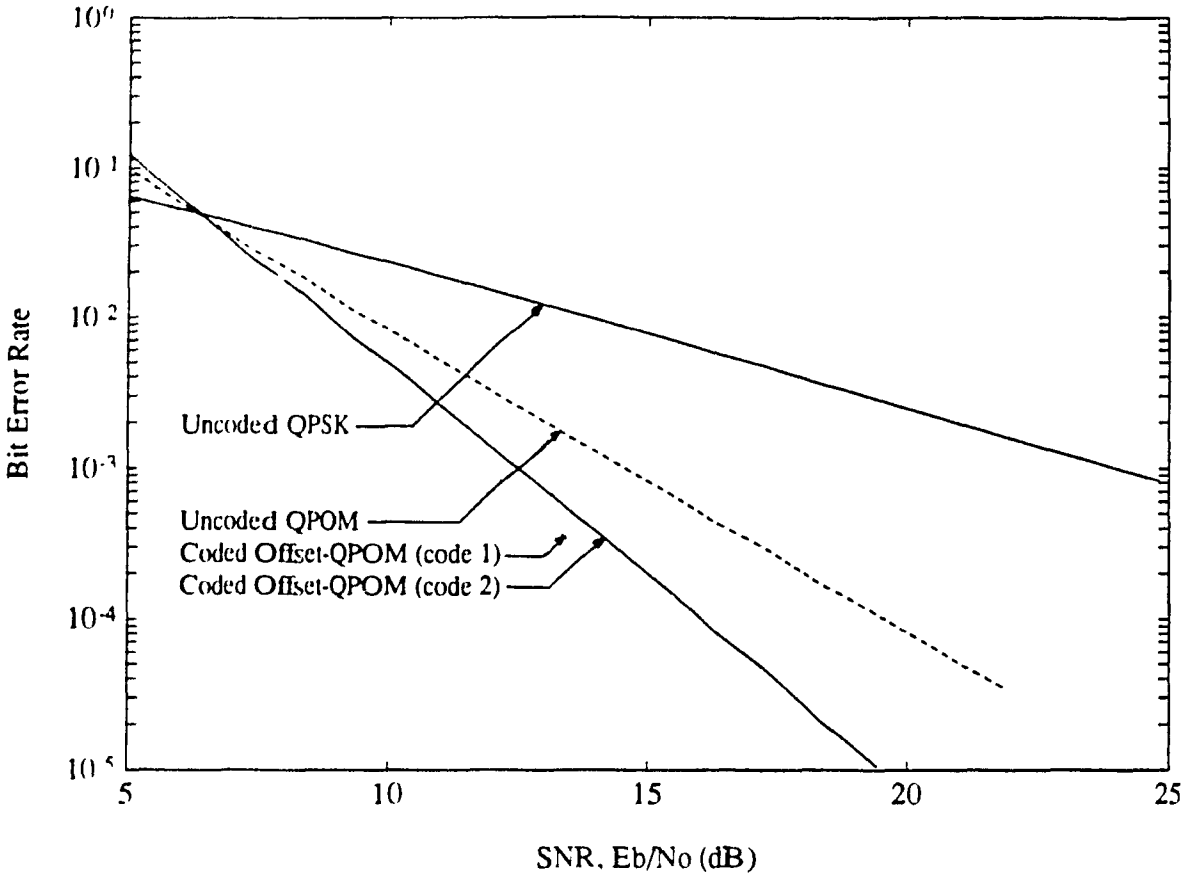

Fig 5.11 – Performance of coded hard-limited Offset-QPOM schemes in Rayleigh fading channels (using 2-state convolutional codes).

Following the same procedure used in selecting 2-state convolutional codes, it is easy to express the output of the concatenated code in terms of the output of the convolutional code. The trellis diagram of this code is shown in Fig. 5.12. We notice that the length of the shortest error even path through the trellis is L = 5, which is equal o the length of the shortest error event path of the convolutional code plus two.

As it was the case for 2-state codes, the design is based on maximizing the distance between signals leaving the same state, the distance between signals merging into the same state, and the product of the squared branch distances along the shortest error event path.

The product β^2, along the shortest error event path is a function of the following symbols:

$$c_1c_0c_{0l}, \quad c_0c_0c_{2l}, \quad c_0c_2c_{4l}, \quad c_2c_4c_{1l}, \quad c_4c_1c_{0l}$$

Assuming that the all zero path is defined by the symbol c_0c_0, i.e.

$$c_0 = 00.$$

From the trellis diagram, we notice that the bit c_{2l} has to be:

$$c_{2l} = 1.$$

The selection of the rest of the symbols are obtained following the same procedure. The design leads to the convolutional codes given in the following Table.

Table 5.3
4-State Convolutional Codes for Hard-Limited Offset-QPOM Schemes

Code	c_0	c_1	c_2	c_3	c_4	c_5	c_6	c_7
code 1	00	11	11	00	01	10	10	01
code 2	00	11	11	00	10	01	01	10

Again when we consider the case of $c_{2l} = 0$, the number of states of the concatenated

code will be reduced from 16 to 8.

5.4. DISCUSSION

The idea of combining convolutional codes and QPOM schemes has been introduced and studied in this chapter. After concatenation, the memory of the two schemes is considered as one entity to be optimized.

To get an idea of the coding gains achievable with combined convolutional codes and Offset-QPOM scheme, some of the codes have been considered. The results are shown in Fig. 5.13. Notice that the potential coding gains are quite significant compared to uncoded BPSK and uncoded Offset-QPOM. By increasing the signal-to-noise ratio, the coding gain is increased. As the memory length v is increased, the performance of the system is also improved.

On the other hand, comparing coded Offset-QPOM with coded QPSK, superior performance is obtained without much sacrifice in complexity as shown in Fig. 5.13. It is observed from the figure that uncoded Offset-QPOM outperforms 2-state coded QPSK.

Although this coding/modulation has been done for 4-level QPOM schemes, it is possible to apply the same idea to M-ary QPOM schemes. This matter is addressed in Chapter 6 where more efficient schemes are discussed.

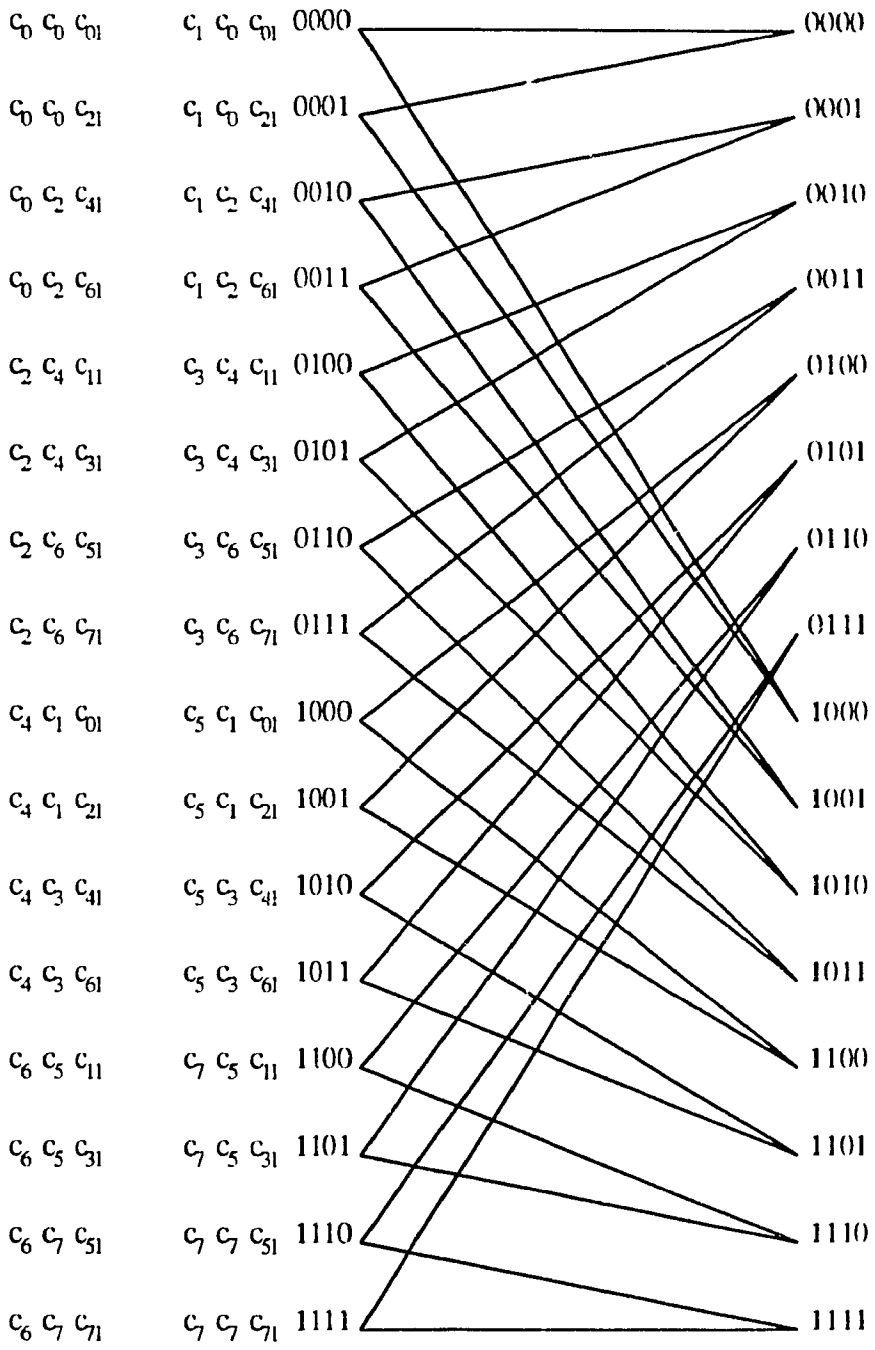

Fig. 5.12 - The trellis diagram of the equivalent code resulting from the concatenation of the code of Fig. 5.6 and the Offset-QPOM encoder

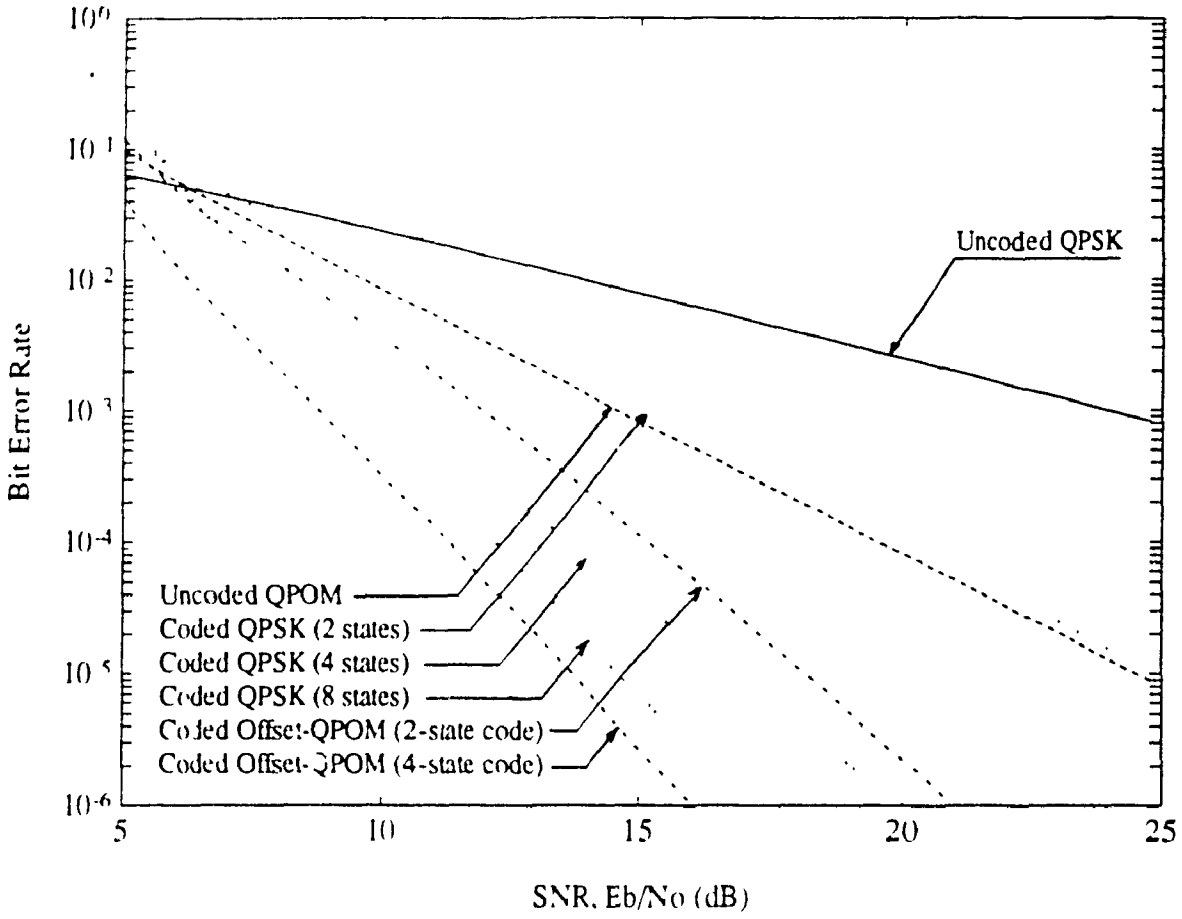

Fig. 5.13 – Performance of coded hard-limited Offset-QPOM schemes in Rayleigh fading channels.

CHAPTER VI

M-ARY QUADRATURE PULSE-OVERLAPPING MODULATION SCHEMES

To achieve high spectral efficiency in terrestrial and satellite communication systems, a transmitted signal should retain a compact spectrum and a low spectral regrowth after a non-linear amplification. We have seen in Chapter 2 that the use of overlapping pulse shapes, where each pulse duration is wider than one symbol interval, is a good tool in providing transmitted signals with good spectral properties. For highly efficient (i.e., more than 2 bits/s/Hz) digital systems, it is desirable to apply double-interval overlapping pulse shapes to M-ary QAM systems [34]. In this Chapter, we apply some of the results obtained in the previous chapters to M-ary quadrature pulse-overlapping modulated signals. We limit our study to 16-QPOM, in which we consider two cases. The first modulation scheme is based on direct quadrature modulation using double-interval overlapping pulse shapes. The second modulation scheme is a more power efficient one. It is considered as two hard-limited QPOM schemes in parallel. It uses *four* identical double-interval pulse shapes and one carrier. The combination of these schemes with convolutional codes is also studied.

6.1. A 16-QUADRATURE PULSE-OVERLAPPING MODULATION SCHEME

The block diagram of a linear 16-QPOM scheme is shown is Fig. 6.1. This block diagram is similar to the one given in Fig. 2.2. A conventional quadrature modulator with two DSB-SC mixers is used as the modulator. The baseband pulse shapes are two identical double-interval pulses satisfying the conditions given by (2.24a, b).

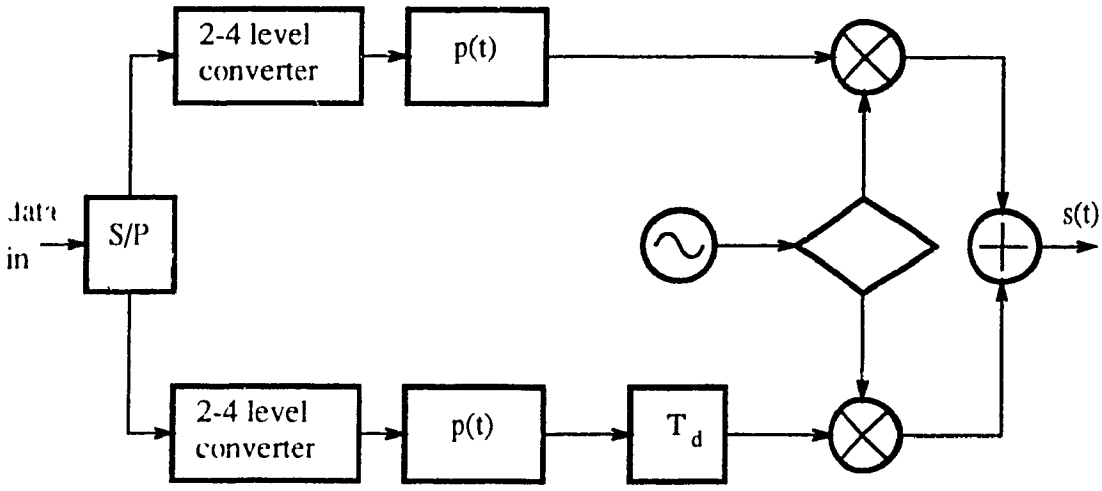

Fig. 6.1 - The block diagram of a 16-QPOM Scheme.

. The transmitted signal can be written as:

$$s(t) = \sum_{n=-\infty}^{+\infty} A_n p(t - nT)\cos 2\pi f_c t + \sum_{n=-\infty}^{+\infty} B_n p(t - nT)\sin 2\pi f_c t. \qquad (6.1)$$

The 2-to-4 level baseband converter converts its input data stream to 4 level, pulse amplitude modulated (PAM) baseband signals having a symbol duration of

$$T = 4T_b,$$

where T_b representing the bit duration. At time nT, the output of each converter can be expressed in terms of its input as:

$$A_n = 2(2a_n + b_n) - 3, \qquad (6.2a)$$

and

$$B_n = 2(2c_n + d_n) - 3. \qquad (6.2b)$$

We notice that the structure of the 16-QPOM modulator is similar to that of 4-level QPOM modulator. For both schemes, the quadrature components are generated in baseband using direct quadrature modulation.

We have seen in Chapter 3 that when the pulse shape is defined over two symbol intervals, at any instant the transmitted signal becomes a function of the present and previous symbols. Furthermore, the two components are independent one from the other giving the option to the receiver to treat each one separately. This last point was proven to be very important because it simplifies the implementation of the MLSE receiver considerably and allow the use of higher bit rates by reducing the delay introduced by the Viterbi decoder.

Applying the procedure used for 4-level QPOM, the 16-QPOM scheme is easily decomposed into two stages, one stage with memory and one stage without memory. As

indicated by Fig. 6.2, each component is represented in the form of a coded scheme. The first stage of each component is a rate 2/4 encoder, where for each pair of input bits a set of *four* bits is generated. The output of this encoder is then mapped to a single interval waveform based on the mapping rules of Table 6.1.

We notice that the structure of this scheme is the same compared to 4-level QPOM schemes with the exception of an increase in the memory of the encoder. Therefore, most of the results obtained in Chapter 3 can be applied here with very little modifications.

Consider the in-phase component of the modulation scheme of Fig. 6.2. Compared to Fig. 3.8, we notice that both schemes have the same encoder. Therefore, the encoder of Fig. 6.2 can be represented by the trellis of Fig. 3.9.

From Table 6.1, it is observed that the transmitted waveform is a function of $(s_0(t), s_1(t))$ defined in (3.3a, b). This implies that each component of the 16-QPOM signal is defined over the same signal space as that of the 4-level QPOM scheme. Therefore, an MLSE receiver for these signals is obtained by using the block diagram of Fig. 3.4, where the Viterbi processor is implemented based on the encoder of the 16-QPOM scheme and the mapping rules of Table. 6.1. This modification is easily done when Digital Signal Processing (DSP) is used. This structure can be easily generalized to M-ary QPOM schemes. For example, if $M = 2^n$ then the M-ary QPOM encoder will be a rate 1/2 encoder with an input symbol of length $n/2$.

Consider the transmission of 16-QPOM signals over the AWGN channel. It is known that the performance is dominated by the minimum squared Euclidean distance of the encoder. Using the trellis diagram, it is easy to show that

$$d^2_{\min} = \int_0^T (s_0(t) + s_1(t))^2 dt = 1.6E_b, \tag{6.3}$$

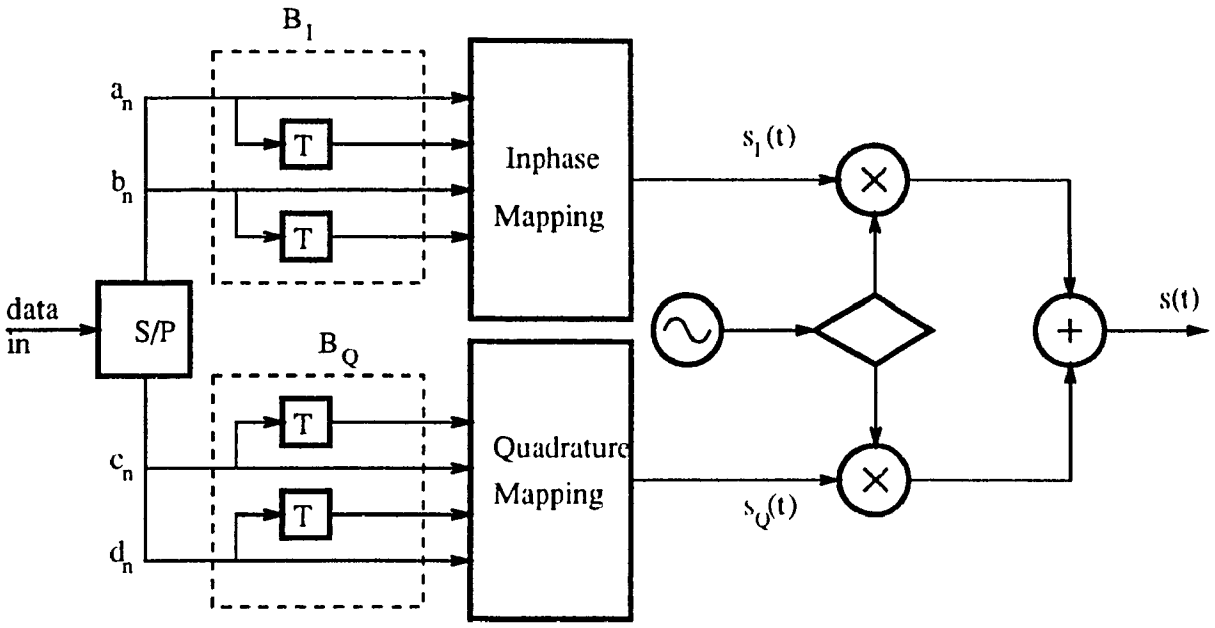

Fig. 6.2 - The new configuration of linear 16-QPOM schemes.

where E_b represents the bit energy, $s_0(t)$ and $s_1(t)$ are given by Eqs. (3.3a, b). Using Eq. (3.34), the bit error rate of 16-QPOM signals over AWGN channels is tightly upper bounded as:

$$P_b \leq \frac{1}{2} erfc\left[\left[0.4E_b/N_0\right]^{1/2}\right]. \tag{6.4}$$

Hence, asymptotically the performance of 16-QPOM signals converges to that of conventional 16-QAM.

Now consider the case of Rayleigh fading channels. From the structure of the trellis diagram of the 16-QPOM encoder, we notice that this scheme offers a time diversity of length 2. Therefore, the performance is expected to vary inversely with the square of the signal-to-noise ratio. Its performance will be better than conventional 16-QAM under the same type of channels. Fig. 6.3 gives the performance of both schemes, it is observed that the 16-QPOM scheme using the new configuration outperforms the conventional 16-QAM for most signal-to-noise ratios. This explains once more the suitability of this structure in fading channels.

Combined convolutional codes and 4-level QPOM schemes was studied in Chapter 5. Results showed that it is possible to improve the performance of QPOM schemes by properly choosing the external encoder. In the following section, the same technique is applied for higher level QPOM schemes. We consider combined convolutional codes and linear 16-QPOM schemes for fading channel applications. The obtained coded scheme has a throughput of 2 bits/symbol and can be compared to most schemes studied in Chapter 4.

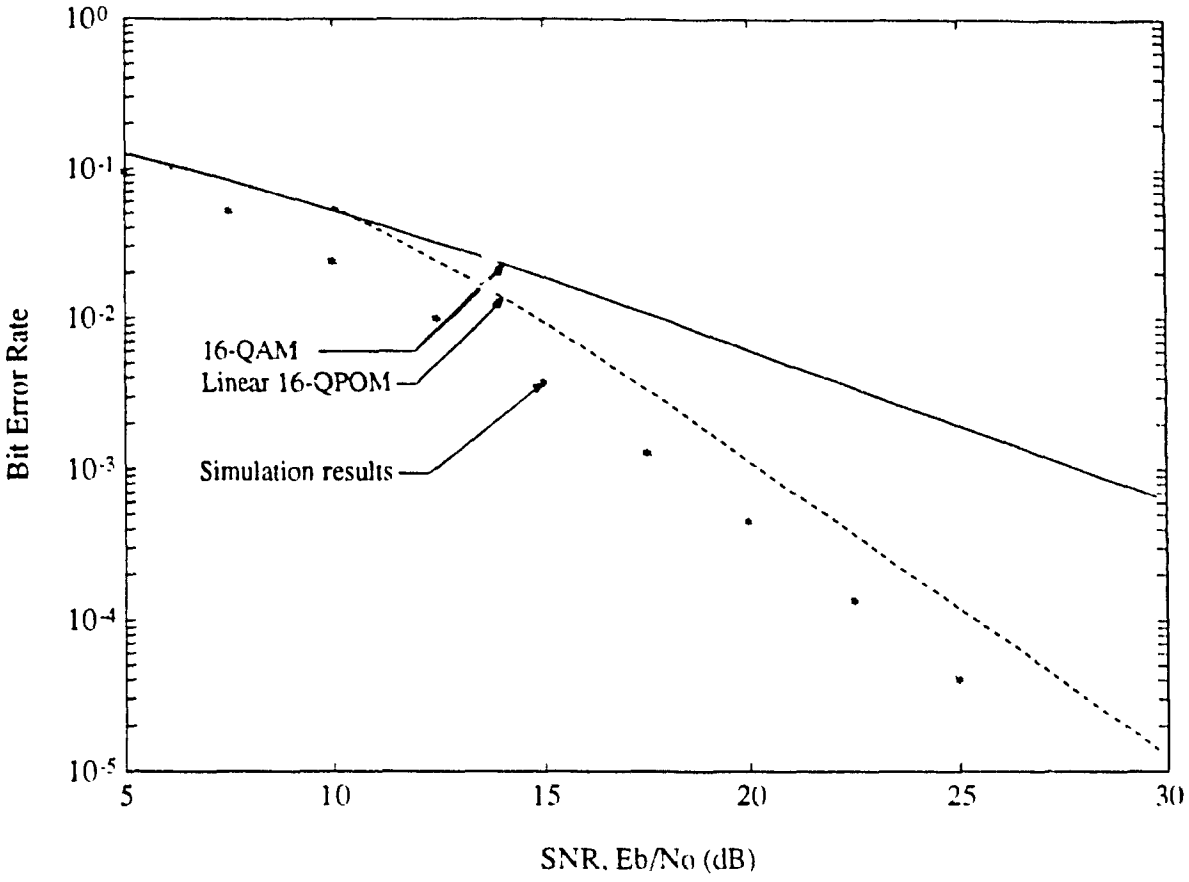

Fig. 6.3 – Performance of 16-QPOM signals in Rayleigh fading channels.

Table 6.1
Mapping Rules for the In-Phase (Quadrature)
Component of Linear 16-QPOM Schemes

Dec.	Symbol $a_n b_n \; a_{n-1} b_{n-1}$	Transmitted signal $s_I(t)$ or $s_Q(t)$
0	00 00	$-3s_0(t)$
1	00 01	$-2s_0(t) - s_1(t)$
2	00 10	$-s_0(t) - 2s_1(t)$
3	00 11	$-3s_1(t)$
4	01 00	$-2s_0(t) + s_1(t)$
5	01 01	$-s_0(t)$
6	01 10	$-s_1(t)$
7	01 11	$+s_0(t) - 2s_1(t)$
8	10 00	$-s_0(t) + 2s_1(t)$
9	10 01	$+s_1(t)$
10	10 10	$+s_0(t)$
11	10 11	$+2s_0(t) - s_1(t)$
12	11 00	$+3s_1(t)$
13	11 01	$+s_0(t) + 2s_1(t)$
14	11 10	$+2s_0(t) + s_1(t)$
15	11 11	$+3s_0(t)$

6.2. CODED LINEAR 16-QPOM SCHEMES

As mentioned earlier, the two components of the linear 16-QPOM scheme are independent from each other. Therefore, we can apply a coding scheme to each one of them independently [80]. This technique can simplify the design of the code and reduce the complexity of the overall system. The coded scheme used in this study is shown in Fig. 6.4. It uses two identical convolutional codes, one for the in-phase component (I channel), and one for the quadrature component (Q channel). The convolutional code is a rate 1/2 code with a total of ν memory. As it was discussed in Chapter 5, the rate of this code is chosen in such a way that the number of states of the concatenated code is reduced. After concatenation, each concatenated code is a rate 1/4 code with a total of $\nu + 1$ memory, and the obtained coded scheme has a net throughput of 2 bits/symbol.

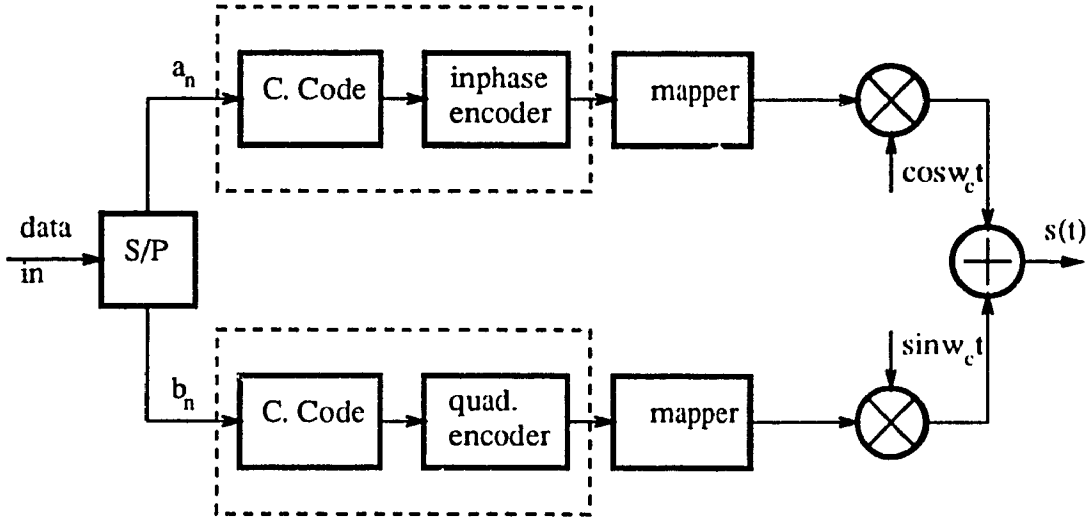

Fig. 6.4 - Convolutionally coded 16-QPOM schemes.

6.2.1. Code selections

In more details, we consider the two cases studied in Chapter 5, namely, 2-state codes and 4-state codes, which have been shown to be effective in the Rayleigh fading environment.

We first consider the linear 16-QPOM scheme and 2-state convolutional codes. From Chapter 5 (section 5.2.1), each concatenated code will have a total of 4 states. Therefore, the coded scheme will have a total of 16 states. However, the configuration of this coded scheme allows the option of independent decoding for each component. In this case the decoding becomes much simpler, and the total number of states is reduced to 8, 4 states for the in-phase component and 4 states for the quadrature component.

In order to select the optimum convolutional code, we consider the signal constellations of one of the two components of the 16-QPOM scheme shown in Fig. 6.5. In addition, the trellis diagram of the concatenated code has to satisfy the conditions of Fig. 5.6. By doing so, the convolutional code having as generators

$$g_1 = [1\ 1] \tag{6.4a}$$

$$g_2 = [1\ 0], \tag{6.4b}$$

(equivalently, $c_0 = 00$, $c_1 = 11$, $c_2 = 10$, $c_3 = 01$), offers the best expected performance. This can be seen from the obtained signal constellation of the concatenated code (Fig. 6.5). We notice that this code is one of the two codes obtained for the hard-limited QPOM scheme.

Combined with the obtained code, the performance of the coded linear 16-QPOM scheme over the Rayleigh fading channel is studied using simulation results. The double-interval overlapping pulse shape used in this study is $p(t) = (1 + cos(\pi t/2T))/2$. The bit error rate is illustrated in Fig. 6.6. For the sake of comparison, the performance of of coherent QPSK, uncoded QPOM, 4-state and 8-state TCM 8PSK are also illustrated in

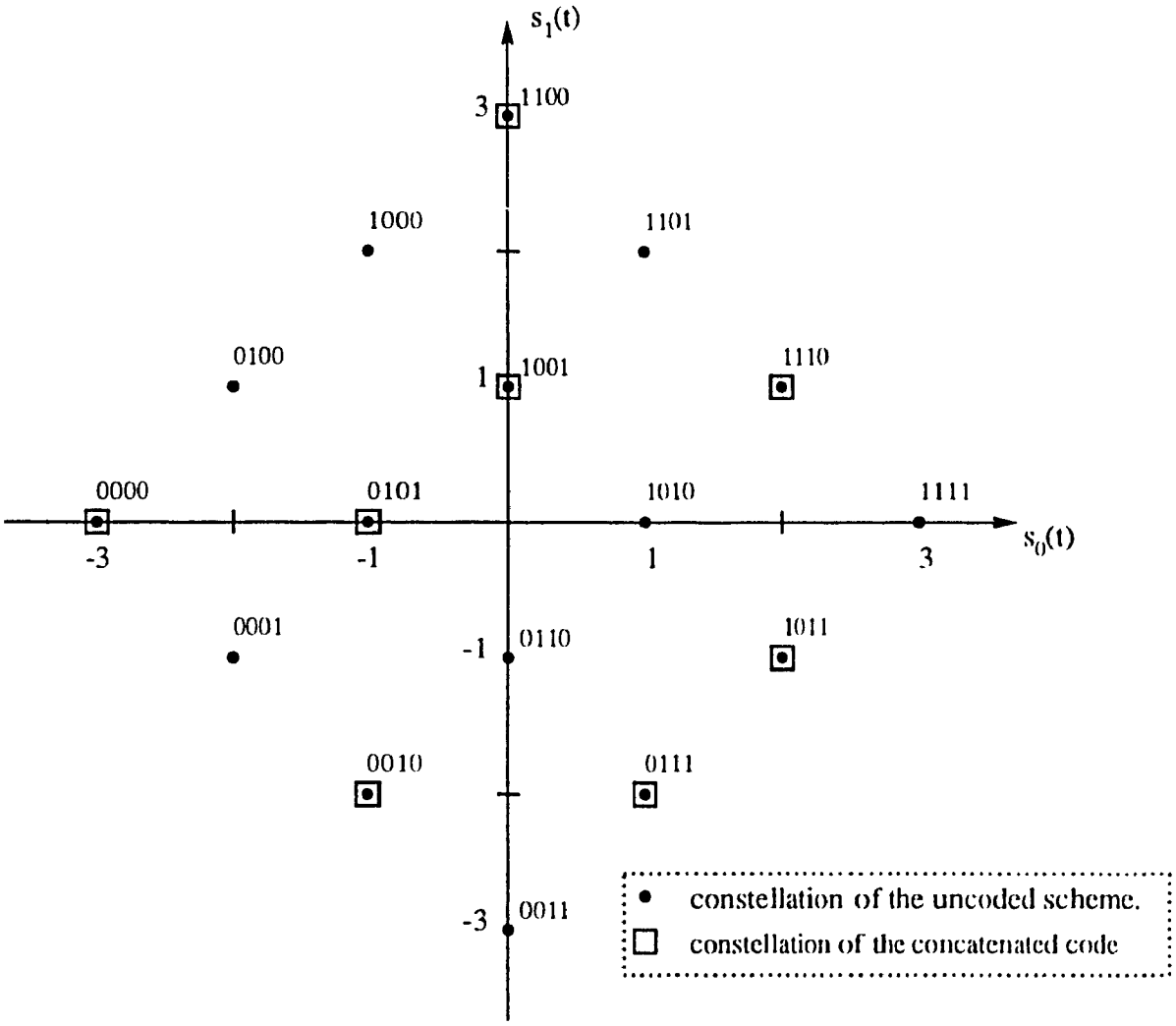

Fig. 6.5 - Signal constellations of the inphase (quadrature) of the 16-QPOM scheme.

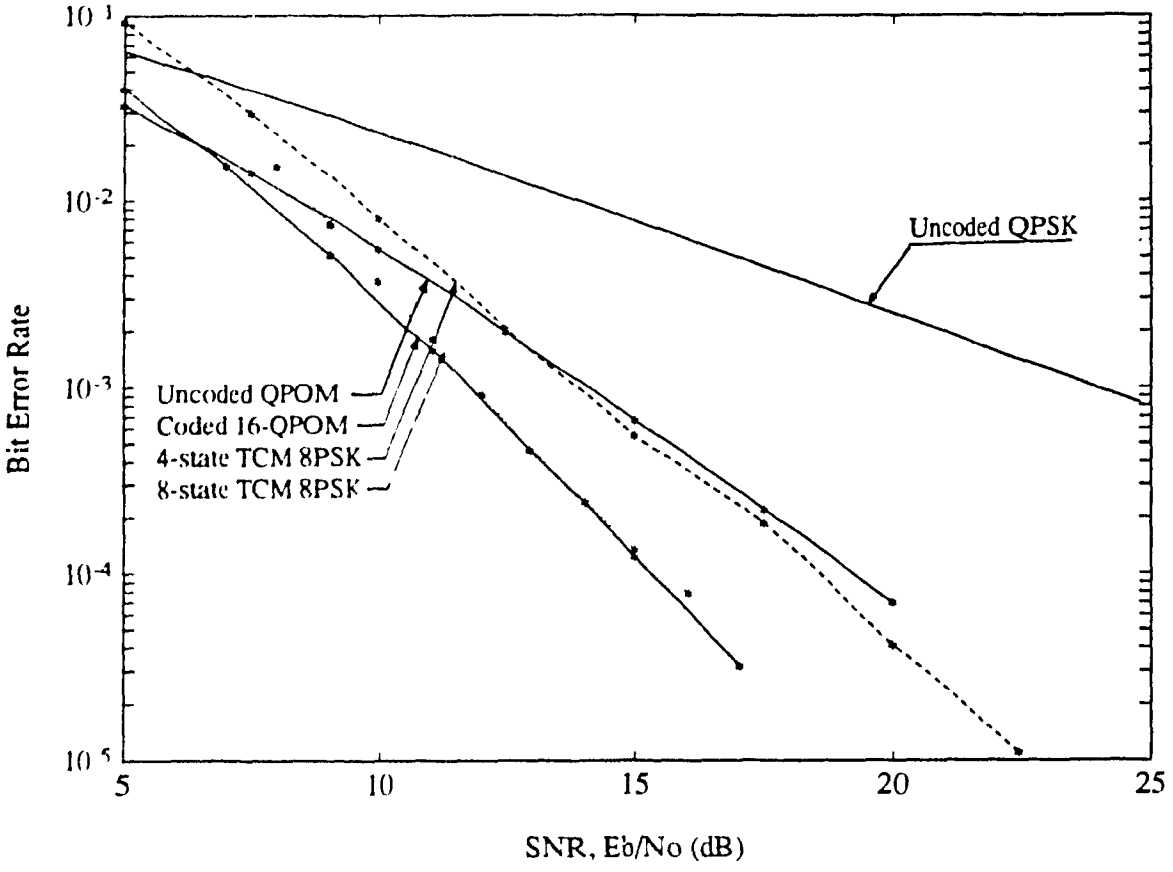

Fig. 6.6 – Performance of coded 16-QPOM signals in Rayleigh fading channels 2-state convolutional code is used).

Fig. 6.6. We observe that the performance improvement compared to uncoded QPOM is quite significant (about 4 dB at a bit error rate of 10^{-4}). This improvement is obtained by simply using a 2-state convolutional code, which shows the importance of the interaction between the memory of the two schemes and the way of combining them. When compared to coding schemes of the same complexity, it is observed that for $E_b/N_0 \leq 15\ dB$, coded 16-QPOM performs better than 8-state TCM 8PSK. Even though the two schemes have the same number of states (a total of 8 states), coded 16-QPOM scheme uses a simpler decoding procedure. This decoding procedure allows the use of two parallel Viterbi processors working on a trellis diagram of 4 states each. This will reduce the time delay introduced by the Viterbi processor and gives the possibility of using higher bit rates. In addition, the 16-QPOM scheme uses pulse shaping in generating the transmitted signal. Therefore, these signals have more compact spectrum compared to uncoded QPSK and coded PSK making coded linear 16-QPOM scheme a better choice for band-limited channels.

With only 2-state convolutional codes, it was possible to generate good coded schemes. By increasing the number of states of the external code, it is possible to design better coding schemes [81]. Next we consider combined linear 16-QPOM schemes and 4-state convolutional codes. Again in this case we use the signal constellations of Fig. 6.5. The selection of the optimum code is done in a manner similar to the one used for the 2-state code. From Chapter 5 (section 5.2.2), when a 4-state convolutional code is used the concatenated code will have a total of 8 states. Therefore, for coded linear 16-QPOM each concatenated code has a total of 8 states. The coded scheme then has a total of 64 states. However, using the option of independent decoding, the total number of states is reduced to 16, 8 states for the in-phase component and 8 states for the quadrature component.

In selecting these convolutional codes we consider the signal constellations of Fig. 6.5 and the trellis diagram of the concatenated code given in Fig. 5.7. We can see that set

partitioning can not be applied here due to the dependence between the subsets of the concatenated code.

Having discussed the way of selecting the appropriate code, we now present the final result without going through all the details. The obtained 4-state convolutional code has the following generators

$$g_1 = [1\ 1\ 1] \tag{6.5a}$$

$$g_2 = [1\ 0\ 1]. \tag{6.5b}$$

Note that this code is one of the two codes selected for hard-limited QPOM schemes.

Fig. 6.7 illustrates the performance of the coded scheme over Rayleigh fading channels. For the sake of comparison, Fig. 6.7 also illustrates the performance of uncoded QPSK, uncoded QPOM, and 8-state TCM 8PSK schemes. It is observed that increasing the number of states has improved further the performance. We may also add that coded 16-QPOM schemes offer very good performance at low signal-to-noise ratio.

In M-ary QAM systems, AM/AM compression and AM/PM conversion non-linearity of transmit HPAs cause significant performance degradation. Thus, for a conventional M-ary QAM, the transmit HPAa are required to operate in a quasi-linear mode, that is, with a high outpnt back-off or at a low power efficiency for a good performance [79]. Therefore, transmitters for multiple amplitude types of signals are inherently less power efficient than those for constant envelope type of signals. For the operation of M-ary QAM at higher power efficiency, we consider a modulation technique that may operate through fully saturated HPAs without need for postmodulation spectral shaping filters while retaining a compact spectrum [78]. Thus a more power efficient signal can be transmitted without significant intersymbol interference due to non-linear effects.

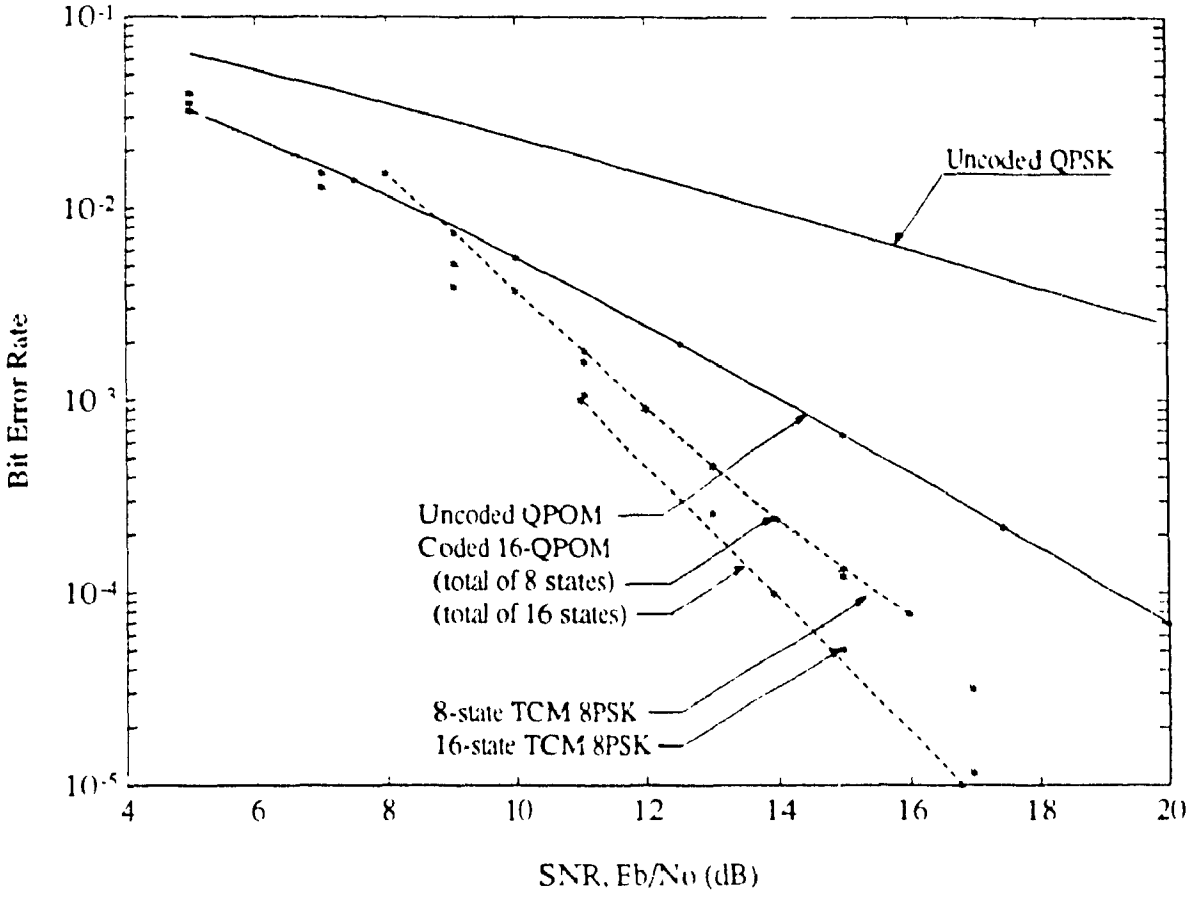

Fig. 6.7 – Performance of coded 16-QPOM signals in Rayleigh fading channels (4-state convolutional code is used).

6.3. POWER EFFICIENT 16-QPOM SCHEMES

Consider the 16-QPOM signal, $s(t)$, given by Eq. (6.1). This signal can be rewritten as:

$$s(t) = \sum_{n=-\infty}^{+\infty} A_n p(t-nT)\cos 2\pi f_c t + \sum_{n=-\infty}^{+\infty} B_n p(t-nT)\sin 2\pi f_c t$$

$$+ 2\sum_{n=-\infty}^{+\infty} C_n p(t-nT)\cos 2\pi f_c t + 2\sum_{n=-\infty}^{+\infty} D_n p(t-nT)\sin 2\pi f_c t \quad (6.6)$$

where

$$A_n = 2a_n - 1, \quad B_n = 2b_n - 1 \quad (6.7a)$$

$$C_n = 2c_n - 1, \quad D_n = 2d_n - 1. \quad (6.7b)$$

It is observed from Eq. (6.6) that the 16-QPOM signal is a linear combination of two Quadrature Pulse-Overlapping Modulated (QPOM) signals, where each QPOM signal is generated independently from the other. Therefore, the 16-QPOM scheme can be considered as two QPOM type signaling schemes in parallel as shown in Fig. 6.8.

In Fig. 6.8, the input data stream is split into 4 parallel streams $\{a_n\}$, $\{b_n\}$, $\{c_n\}$, and $\{d_n\}$. The data streams $\{a_n\}$ and $\{b_n\}$ are fed into the in-phase and quadrature channels of the first QPOM scheme, respectively, and the data streams $\{c_n\}$ and $\{d_n\}$ are fed into the in-phase and quadrature channels of the second QPOM scheme.

The envelope fluctuations of the QPOM signals, $s_1(t)$ and $s_2(t)$, are removed after hard-limiting. Hence, the hard-limited QPOM signals, $z_1(t)$ and $z_2(t)$, suffer no major degradation due to nonlinear amplification. The output voltage of the second high power amplifier is arranged to be twice that of the first amplifier to satisfy Eq. (6.6). The outputs of the two amplifiers are added to give the 16-QPOM transmitted signal.

S/P is a 1-to-4 parallel converter

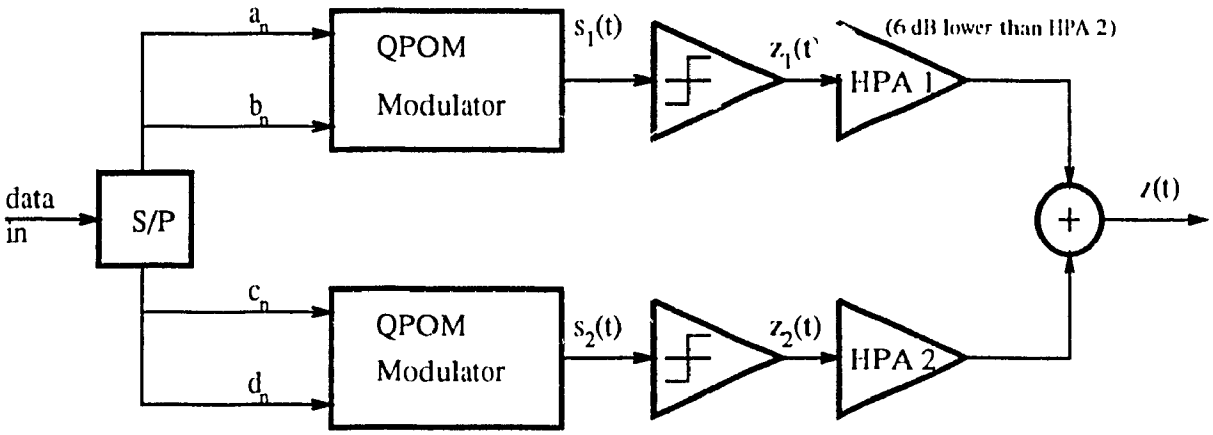

Fig. 6.8 - The block diagram of a power efficient 16-QPOM modulator.

Since the shapes of the power spectral density of both $z_1(t)$ and $z_2(t)$ are identical and the 16-QPOM signal $z(t)$ is a linear combination of those two signals, it can be shown that the power spectrum of $z(t)$ has the same shape as that of $z_1(t)$ or $z_2(t)$ [45]. In addition, the spectral efficiency of this 16-QPOM scheme is double relative to the QPOM scheme for the same bit rate.

Our objective in this section is to study the performance of this scheme in both AWGN and fading channels. The idea is to apply the results obtained in the previous chapters. We have seen in Chapter 3 that at any symbol interval a hard-limited QPOM signal can be represented by a vector $\underline{z}$ in the signal space. This vector is an 8-element vector when hard-limited QPOM signals are considered, or a 12-element vector in the case of Offset-QPOM signals. Given the relation between $z(t)$, $z_1(t)$ and $z_2(t)$, the signal space diagram of $z(t)$ can be derived from those of $z_1(t)$ and $z_2(t)$ using vector additions. Therefore, if at time nT $z_1(t)$ and $z_2(t)$ are represented by the vectors $\underline{z}_{1n}$ and $\underline{z}_{2n}$, respectively, then the 16-QPOM signal, $z(t)$, will be represented by the vector

$$\underline{z}_n = \underline{z}_{1n} + 2\underline{z}_{2n}. \tag{6.8}$$

This indicates that 16-QPOM signals and hard-limited QPOM signals are defined over the same signal space.

Since 16-QPOM signals are linear combinations of two hard-limited QPOM signals, the 16-QPOM scheme can also be decomposed into an encoder followed by a memoryless modulator. The modulation encoder is a rate 4/8 encoder with an input symbol of length 4 and a total of 16 states. This encoder is constructed using two hard-limited QPOM encoders in parallel. The mapping rules of the memoryless modulator consists of all possible combinations of $z_1(t)$ and $z_2(t)$, which gives a total of 256 different pair of waveforms $(z_I(t), z_Q(t))$. Contrary to the case of section 6.1, the two components of the this scheme cannot be treated independently due to the correlation that exists between

them. Therefore, an optimum receiver need to treat both components simultaneously. This means that the detection procedure will be much more complex than the one used in the previous section. Never-the-less, the choice of the modulation/demodulation scheme will depend on the application and the kind of compromise that can be done.

The performance of this scheme can be studied based on its trellis diagram. For example, the minimum squared Euclidean distance is given by

$$d_{\min}^2 = 3.2(1 - \beta_0),$$

where β_0 is a coefficient depending on the pulse shape $p(t)$ and is defined in (3.52a). As β_0 approaches 0.5, the performance of this scheme over AWGN channels approaches that of conventional coherent 16-QAM scheme.

Fig. 6.9 illustrates the performance of this scheme and the performance of the linear 16-QPOM scheme that has been studied in section 6.1. Both schemes use the double-interval pulse shape $p(t) = (1 + cos(\pi t/2T))/2$. As we can see the simulation results agrees with the predicted ones.

The performance of this scheme over the Rayleigh fading channel can be upper bounded as:

$$P_b \leq 0.25\left[1 + 0.4(1 - \beta_0)E_b/N_0\right]^{-2},$$

which as expected varies inversely with the square of E_b/N_0. Fig. 6.10 illustrates the performance improvement of this scheme compared to conventional coherent 16-QAM. The improvement is again due to the time diversity introduced by the memory of the modulation scheme. From the above discussion it is apparent that the penalty paid for improving the performance of power efficient 16-QPOM schemes is an increase in the complexity of the MLSE receiver. In return, the advantage of increasing M is a reduction in the signal-to-noise ratio per bit required to attain a specified probability of error. In the

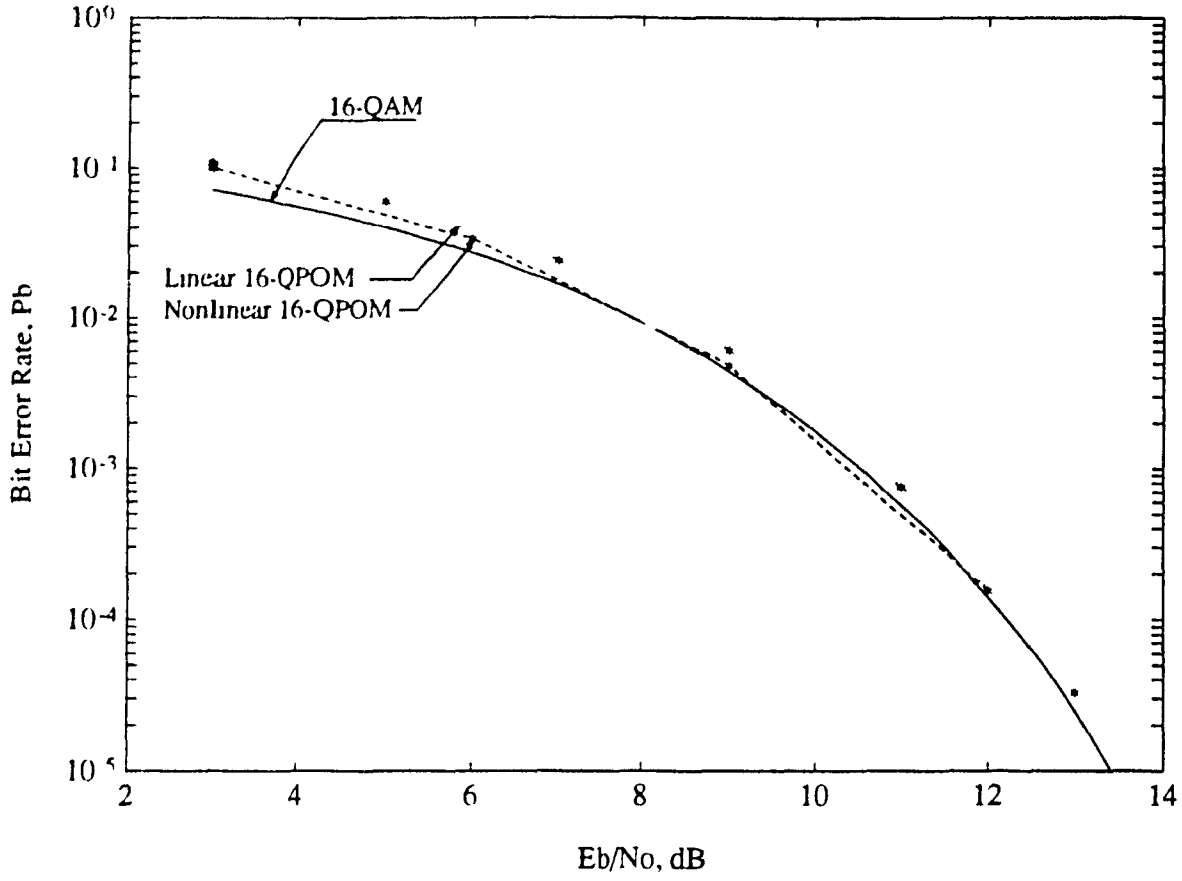

Fig. 6.9 – Performance of power efficient 16-QPOM signals in AWGN channels

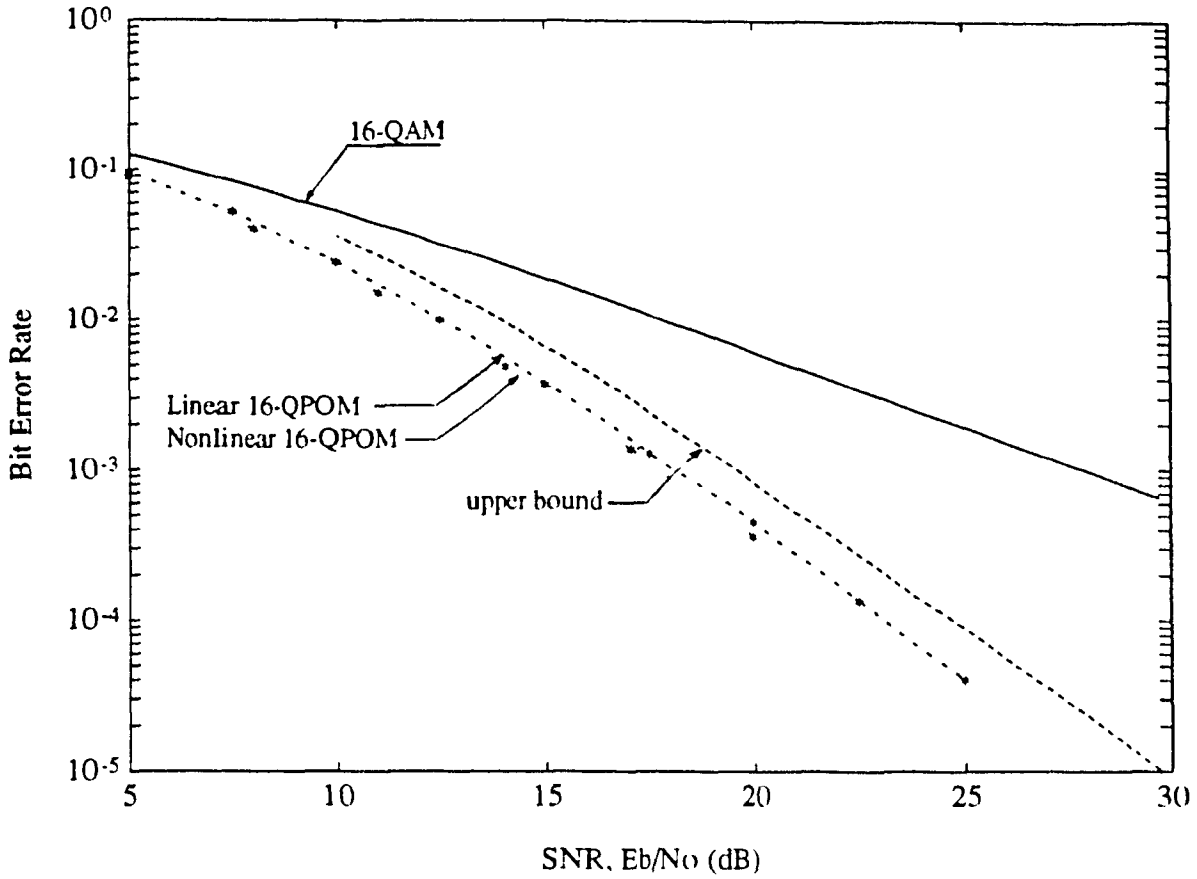

Fig. 6.10 – Performance of power efficient 16-QPOM signals in Rayleigh fading channels.

following section we consider combined convolutional codes and power efficient 16-QPOM schemes.

6.4. CODED HARD-LIMITED 16-QPOM SCHEMES

This scheme can also be combined with convolutional codes in a manner similar to the one used for hard-limited QPOM schemes. Since the total number of states for the uncoded scheme is already high (16 states), we will consider convolutional codes which when combined with the uncoded 16-QPOM scheme will not increase its total number of states. This will depend on the choice of the convolutional code. In achieving this objective, we consider rate 2/4 convolutional codes. The obtained coded scheme will have a net throughput of 2 bits/symbol and can be compared to most schemes studied earlier in this thesis.

6.4.1. Code Selections

Even though the original uncoded scheme has a total of 16 states, it is possible to obtain a coded scheme of only 8 states. Consider a convolutional code of rate 2/4 and a total of 2 states. The length of its output symbol is 4 which matches that of the input symbol of the 16-QPOM encoder. Depending on the input symbol, the output of this code is $\{c_i, i = 0, 1, \ldots, 7\}$, and can take any value from 0 to 15. Since this code has a total of 2 states, then its total memory is 1. When this code is combined with the 16-QPOM encoder, the obtained code is a rate 2/8 convolutional code.

Suppose that output of the external convolutional at time nT is given by the symbol $c_n = c_{0n}c_{1n}c_{2n}c_{3n}$ and its input by the symbol $a_n b_n$. Because this code has only one memory, we can say that each bit of the symbol c_n is a function of (a_n, b_n, a_{n-1}) or (a_n, b_n, b_{n-1}). The output of the concatenated code expressed in terms of c_n can then be written as:

$$cc_n = c_n c_{n-1}$$

$$= c_{0n} c_{1n} c_{2n} c_{3n}\ c_{0(n-1)} c_{1(n-1)} c_{2(n-1)} c_{3(n-1)}.$$

Therefore, each bit of the output symbol of the concatenated code becomes a function of $(a_n, b_n, a_{n-1}, b_{n-1}, a_{n-2})$ or $(a_n, b_n, a_{n-1}, b_{n-1}, b_{n-2})$. This indicates that the total memory of the concatenated code is 3, and its total number of states is 8. The trellis diagram of this code is shown in Fig. 6.11. As we can see it has a total of only 8 states. Of course we do not expect a lot of gain with this code, since it offers a time diversity of length $L = 2$, which is the same as the uncoded scheme. However, the complexity is greatly reduced: First, the total number of states of the concatenated code is half that of the uncoded scheme, and second, the inner connectivity between states is reduced from 8 (uncoded scheme) to 4 (coded scheme).

In order to select a code, we consider the rules used in the previous chapters. These rules consist mostly on maximizing the product of the squared distances along the shortest path of the trellis. By doing so, the convolutional code defined by

$$c_{0n} = a_n$$

$$c_{1n} = a_n + b_n + a_{n-1}$$

$$c_{2n} = a_n + a_{n-1}$$

$$c_{3n} = a_n + b_n + a_{n-1}$$

($a_n b_n$ represents the input symbol) has been selected.

The performance of this coded scheme over Rayleigh fading channels is shown in Fig. 6.12. It is observed that its performance is comparable to that of uncoded QPOM scheme.

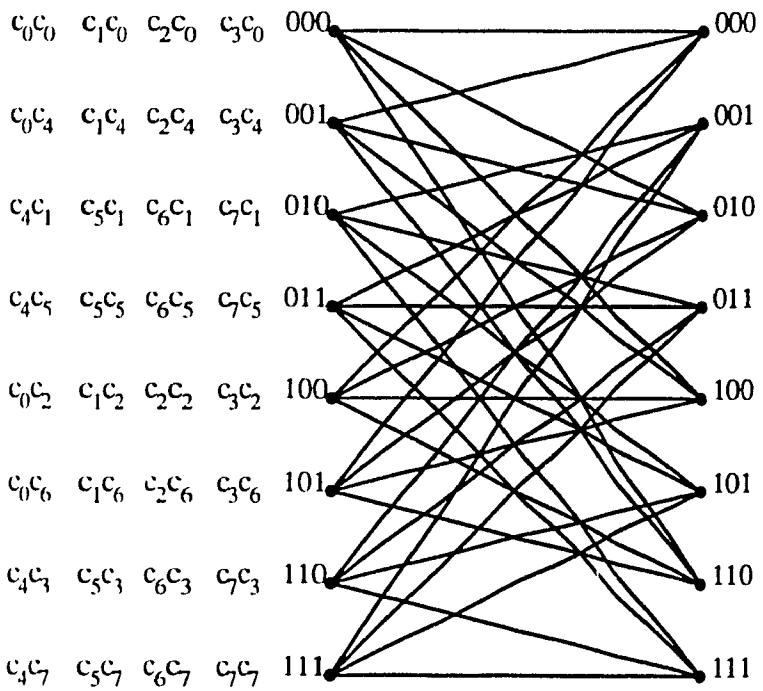

Fig. 6.11 - The trellis diagram of coded nonlinear 16-QPOM schemes.

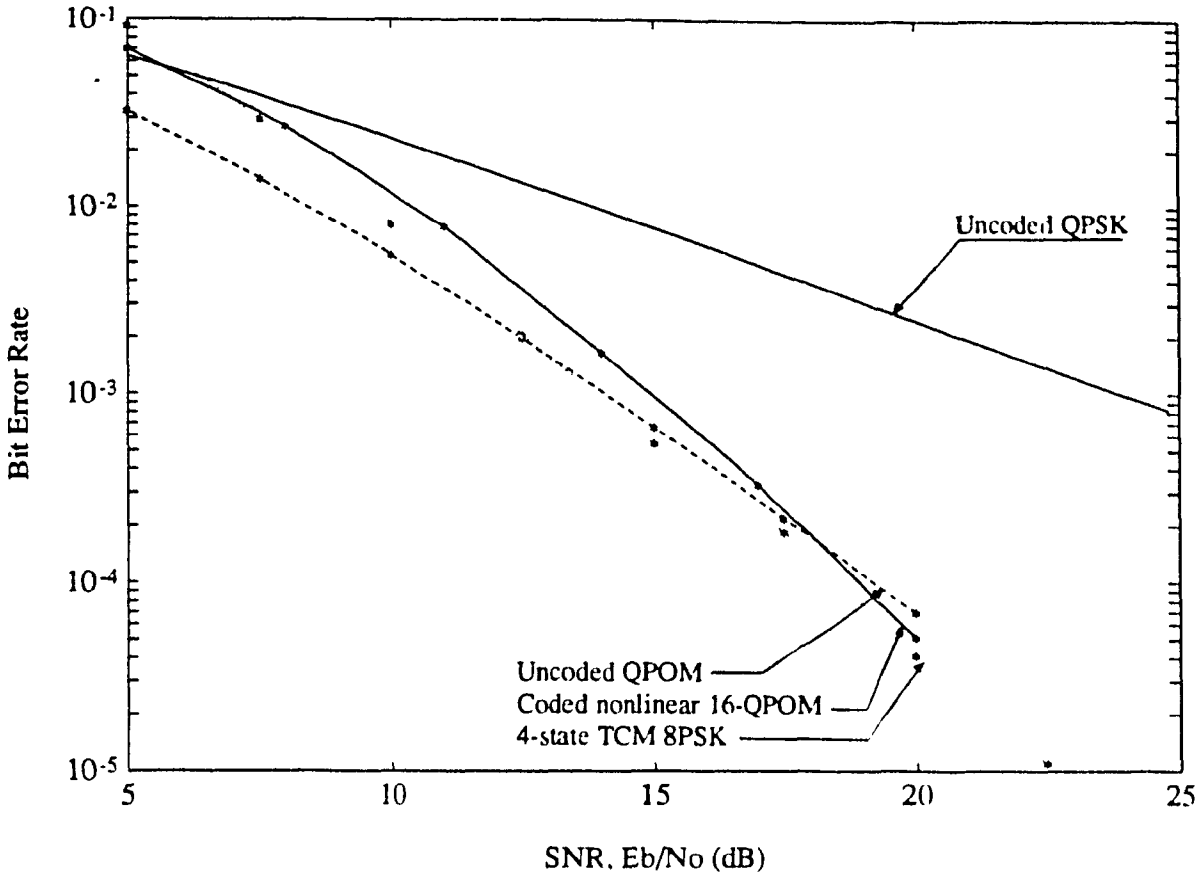

Fig. 6.12 – Performance of coded power efficient 16-QPOM signals in Rayleigh fading channels.

6.5. SUMMARY

In this Chapter We have studied the performance of two 16-level quadrature modulation schemes. The structure of linear 16-QPOM schemes allowed the use of independent decoding for the in-phase and quadrature components of the transmitted signal. Thus, reducing considerably the complexity of the MLSE receiver. To save this structure, we showed that it is possible to apply a coding scheme for each component. We considered 2-state and 4-state convolutional codes. Although these codes are not very strong when combined with conventional schemes, the obtained results showed that by properly combining the memory of these coded schemes and the memory of the modulation, the performance of the system is improved. For example, in Rayleigh fading channels, this coded scheme performs better than TCM 8PSK schemes especially for low signal-to-noise ratio.

Hard-limited 16-QPOM scheme used two parallel hard-limited QPOM schemes. We showed that an optimum MLSE receiver for this type of signal need to consider both in-phase and quadrature components at the same time. Thus, its performance was slightly better than that of linear 16-QPOM signal, but its encoder was more complex. In Rayleigh fading channels both schemes perform better than conventional coherent 16-QAM. Combined convolutional codes and hard-limited 16-QPOM schemes was investigated. By using a 2-state code, the complexity of the decoder was reduced by half and a comparable performance to uncoded QPOM was achieved.

CHAPTER VII

CONCLUSIONS AND SUGGESTIONS FOR FURTHER RESEARCH

7.1. CONCLUSIONS

A Maximum Likelihood Sequence Estimation (MLSE) receiver for Quadrature Pulse-Overlapping Modulated (QPOM) signals for fading channels applications was introduced. Instead of using extra coding to achieve this goal, a detection technique exploiting all the memory introduced by the overlapping pulse shape was used.

The QPOM scheme was decomposed into an encoder followed by a memoryless modulator. The obtained configuration is similar to most conventional coded schemes. The memory introduced by the double-interval overlapping pulse shape and the cross-correlation caused by the hard-limiter are represented in a form that are fully exploited by the receiver.

The performance of both linear and nonlinear QPOM schemes in AWGN channels was analyzed by means of upper bound techniques and simulation results. It was shown that the performance of QPOM signals can be expressed as a function of the transmitted pulse shape. Therefore, it is now possible to select double-interval overlapping pulse shapes for a compact spectrum and good performance simultaneously. The performance of Offset-QPOM signals was also analyzed and discussed. It was shown that the time delay introduced at the quadrature component of the modulator did not affect the performance of linear schemes. However, after nonlinear amplification this time delay introduces more correlation into the transmitted signal and a more complex receiver is required.

In Chapter 4, we considered the performance of QPOM signals in fading channels.

The MLSE receiver was constructed by exploiting the inherent non-redundant coding structure of the modulation scheme. The trellis diagram of this coding structure does not have parallel paths from one state to the next, and makes it suitable to combat fading. When compared to rate 2/3 4-state TCM 8PSK, it was shown that for $E_b \leq 13\ dB$ QPOM schemes offer a better performance.

Consider the fact that hard-limited QPOM schemes are actually 4-level PSK schemes while the TCM is an 8-level PSK scheme. It can be seen that hard-limited QPOM schemes are less sensitive to phase error, and both schemes have the same complexity. For these reasons, hard-limited QPOM schemes are a better choice in practice for portable/mobile satellite communication systems.

In Chapter 5, hard-limited QPOM schemes were successfully combined with outer convolutional codes. Using the new configuration of these schemes, the memory of both schemes was considered as one entity to be optimized. It was shown that by properly choosing the convolutional code, the complexity of the concatenated code can be reduced. For example, the number of states of coded Offset-QPOM schemes was reduced by a factor of *four*. The performance is improved in comparison with the uncoded scheme and some convolutionally coded QPSK schemes. The main result of this Chapter is the way of combining the memory of the QPOM scheme and that of the external encoder. This result was presented in a general form and was easily extented to more efficient schemes.

In Chapter 6, the performance of two different 16-level quadrature pulse-overlapping modulated signals was studied. As it was the case for 4-level schemes, linear 16-QPOM schemes allowed the use of independent decoding for the in-phase and quadrature components of the transmitted signal. Thus, reducing the complexity of the MLSE receiver considerably. Using this structure and applying the results of Chapter 5, coded linear 16-QPOM was studied. The performance was improved and comparable

results to some coded schemes were obtained. A more power efficient 16-QPOM scheme was then considered. This scheme used two hard-limited QPOM schemes in parallel. Its performance was comparable to that of the linear scheme, but its MLSE receiver was more complex. In Rayleigh fading channels, both schemes performed better than conventional 16-QAM. Combined convolutional codes and power efficient 16-QPOM was investigated. By using a 2-state code, the complexity of the decoder was reduced by a factor of *two* and comparable performance to uncoded 4-level QPOM schemes was achieved.

The performance improvement of quadrature pulse-overlapping modulated schemes with its compact spectrum and low-complexity make these schemes a good choice for portable/mobile satellite communications to achieve the requirement of low cost, small size, and high power and bandwidth efficiencies.

7.2. SUGGESTIONS FOR FURTHER RESEARCH

The performance of quadrature pulse-overlapping modulated signals in both AWGN and fading channels were extensively studied in our research. However, there are still other aspects to be considered and studied.

Finite Interleaving: In fading channels, we considered the assumption of ideal interleaving/de-interleaving and ideal channel state information. In practice the depth of interleaving is finite and chosen in relation to the maximum fade duration anticipated [29]. It will be interesting to see the effect of interleaving depth and the unavailability of the channel state information on the performance of QPOM signals.

Non-Coherent Demodulation of QPOM Signals: Throughout this thesis we evaluated the performance of QPOM signals for ideal case of coherent detection. Non-coherent demodulators do not need a carrier recovery and therefore are desirable for their simple structure. For example if an independent local oscillator (same frequency as

the carrier) is used at the receiver, the Viterbi decoder can be modified to resolve the phase offset [28]. The study of non-coherent detection of QPOM schemes using the obtained new configuration may be desirable.

Block Coded QPOM Schemes: We considered combined convolutional codes and QPOM schemes. Block coded modulation schemes using soft-decision decoding show good performance in Rayleigh fading channels. Furthermore, the concatenation of a block code and a convolutional code can improve the performance. Concatenated block codes and convolutional codes are very effective against a mixture of both random and burst-error patterns. Since the QPOM encoder is a convolutional code, it will be interesting to combine this scheme with Reed-Solomn block codes.

The Use of Different Classes of Pulse Shapes: Throughout this thesis, we have considered double-interval pulse shapes satisfying the following characteristics

$$p(t) = p(-t), \quad \forall\ t$$
$$p(t) = 0, \quad |t| \geq T$$

The obtained results showed that the performance of the system depends on the pulse shape $p(t)$. It will be interesting to investigate the performance of QPOM signals using different classes of double-interval pulse shapes. In this case combined modulation/coding/pulse shaping can be considered.

Performance of QPOM Signals in Selective Fading Channels: Throughout this thesis we considered the performance of QPOM signals in non-selective fading channels. However, in some cases the coherence bandwidth of the fading channel is smaller than the signal bandwidth and the fading becomes frequency-selective channel. The effect of this fading channel on the performance of QPOM signals is a good subject to study.

REFERENCES

[1] T. Le-Ngoc, K. Feher, H. Phamvan, "New modulation techniques for low-cost power and bandwidth efficient satellite earth stations," *IEEE Trans. Commun.*, vol. COM-25, NO. 7, pp. 633-643, July 1977.

[2] D. C. Cox, "Universal digital portable radio communications,", *Proc. of the IEEE*, vol. 75, N0. 4, pp. 436-474, April 1987.

[3] S. Pasupathy, "Minimum shift keying: a spectrally efficient modulation," *IEEE Commun. Mag.*, pp. 14-22, July 1979.

[4] S. A Gronemeyer and A. L. McBride, "MSK and offset QPSK modulation," *IEEE Trans. Commun.*, vol. COM-24, pp. 809-820, Aug. 1976.

[5] T. Aulin, C-E Sundberg, "Continuous phase modulation Part I: Full-response signalling", *IEEE Trans. Commun., vol. COM-29, pp. 196-209, March 1981.*

[6] F. Amoroso, "Pulse and spectrum manipulation in the minimum (frequency) shift keying (MSK) format," *IEEE Trans. Commun.*, vol. COM-24, pp. 381-384, March 1976.

[7] J. G. Smith, "Spectrally efficient modulation," *in Proc. IEEE Int. Conf. Commun.* (ICC' 77), pp. 3.1-37/3.1-41, June, 1977.

[8] B. Bazin, "A class of MSK Baseband pulse formats with sharp spectral roll-off", *IEEE Trans. Commun.*, vol. COM-27, pp. 826-829, May 1979.

[9] M. C. Austin, M. U. Chang, "Quadrature overlapped raised-cosine modulation," *IEEE Trans. Commun.*, vol. COM-29, NO. 3, pp. 237-249, March 1981.

[10] F. Amoroso, "The use of quasi-bandlimited pulses in MSK transmission," *IEEE Trans. Commun.*, vol COM-27, pp. 1616-1624, Oct., 1979.

[11] M. K. Simon, "A generalization of minimum shift keying (MSK)-type signalling

based upon input data symbol pulse shaping," *IEEE Trans. Commun.*, vo. COM-24, pp. 845-856, August 1976.

[12] M. Rabzel, S. Pasupathy, "Spectral shaping in minimum shift keying (MSK)-type signals," *IEEE Trans. Commun.*, vol. COM-26, pp. 189-195, January 1978.

[13] C. E. Sundberg, "Continuous phase modulation," *IEEE Trans. Commun. Mag.*, vol. 24, pp. 25-38, April, 1986.

[14] K. Murota, et al., "Spectrum efficiency of GMSK land mobile radio," *IEEE ICC'81, p.23.8.1, June 1981.*

[15] F. de Jager and C. B. Dekker, "Tamed frequency modulation-A novel approach to achieve spectral economy in digital transmission," *IEEE Trans. Commun.*, vol. COM-26, pp. 534-542, May 1978.

[16] K. S. Chung, "Generalized tamed frequency modulation and its application for mobile radio communications," *IEEE Trans. Veh. Technology*, vol. VT-33, NO. 3, August 1984.

[17] T. Aulin et al., "Continuous phase modulation-Part II: partial response signaling," *IEEE Trans. Commun.*, vol. COM-29, N0. 3, pp. 210-225, March 1981.

[18] D. Saha, T. G. Birdsall, "Quadrature-quadrature phase-shift keying," *IEEE Trans. Commun.*, vol. COM-37, NO. 5, pp. 437-448, May 1989.

[19] T. Le-Ngoc, "Power and bandwidth efficient ISI and jitter free (IJF) signals," *Journal, IERE*, vol. 55, NO. 7, pp. 268-274, July 1985.

[20] A. Lender, "Correlative level coding for binary data transmission," *IEEE Spectrum*, vol. 3, pp. 104-115, Feb. 1966.

[21] G. Forney, "Maximum likelihood sequence estimation of digital sequences in the presence of intersymbol interference," *IEEE Trans. inf. Theory*, vol. IT-18, pp. 363-378, May 1972.

[22] S. Samejima, et al., "Differential PSK system with nonredundant error correction," *IEEE J. Selec. Areas Commun.*, vol. SAC-1, pp. 74-81, January 1983.

[23] M. Ishizuka and Y. Yasuda, "Improved detection of GMSK,", *IEEE Trans. Commun.*, vol. COM-32, NO. 3, pp. 308-311, March 1984.

[24] J. G. Proakis, *Digital Communications*, McGraw Hill, 1983.

[25] T. Le.Ngoc, "A differential offset-QPSK modulation/demodulation techniques for point-to-multipoint radio systems," *Globecom '87*, Tokyo Japan, Nov. 15-18, 1987.

[26] H. Suziki, "Optimum Gaussian filter for differential detection MSK," *IEEE Trans. Commun.*, vol. COM-29, pp. 916-918, June 1981.

[27] J. M. Wozencraft, J. M. Jacobs, *Principles of Communication Engineering*, New York, Willey 1965.

[28] G. Ascheid et al., "An all digital receiver architecture for bandwidth efficient transmission at high data rates," *IEEE Trans. Commun.*, vol. 37, NO. 8, pp. 804-813, August 1989.

[29] D. Divsalar and M. K. Simon, "Trellis coded modulation for 4800-9600 bits/s transmission over fading satellite channel," *IEEE J. Select. Areas Commun.*, vol. SAC-5, NO. 2, pp. 162-175, Feb. 1987.

[30] G. J. Garrison, "A power spectral density analysis for digital FM," *IEEE Trans. Commun.*, vol. COM-23, pp. 1228-1242, November 1975.

[31] D. Divsalar and M. K. Simon, "The power spectral density of digital modulations transmitted over nonlinear channels," *IEEE Trans. Commun.*, vol. COM-30, pp. 142-151, Jan. 1982.

[32] D. H. Morais, K. Feher, "The effects of filtering and limiting on the performance of PQSK, Offset QPSK and MSK systems," *IEEE Trans. Commun.*, vol. COM-28,

NO. 12, pp. 1999-2009, Dec. 1930.

[33] P. K. M. Ho and P. J. McLane, "Power spectral density of digital continuous phase modulation with correlated data symbols. Part 1: Autocorrelation function method," *IEE Proc.*, vol. 133, pp. 95-105, Febr., 1986.

[34] P. K. M. Ho, P. J. McLane, "Power spectral density of digital continuous phase modulation with correlated data symbols. Part 2: Rowe-Prabhu method," *IEE Proc.*, vol. 133, pp. 106-114, Febr., 1986.

[35] G. D. Forney et al., "Efficient modulation for band-limited channels," *IEEE J. Select. Areas Commun.*, vol. SAC-2, NO. 5, pp. 632-647, September 1984.

[36] S. B. Slimane and T. Le-Ngoc, "Maximum likelihood sequence estimation of quadrature pulse-overlapping modulated signals in Rayleigh fading channels," *Canadian Conf. Elect. Comp. Eng.*, Quebec, Canada, September 25-27 1991.

[37] T. Le-Ngoc, K. Feher, "Performance of new IJF-OQPSK modulation schemes in the presence of noise, inter-channel and co-channel interference," *NTC'81*, New Orleans, Louisiana, Nov. 29-Dec. 3, 1981.

[38] S. B. Slimane, T. Le-Ngoc, "Performance of quadrature pulse-overlapping modulated signals over fading channels," *Globcom'91*, Pheonix, Arizona, Dec. 2-5, 1991.

[39] T. Le-Ngoc, S. B. Slimane, "IJF-OQPSK modulation schemes with MLSE receivers for portable/mobile communications," *VTC'92*, Denver, Colorado, May 11-13 1992.

[40] J. H. Lodge et al., "A comparison of data modulation techniques for land mobile satellite channel," *IEEE Trans. Vehic. Tech.*, vol. VT-36, pp. 28-35, February 1987.

[41] A. J. Viterbi and J. K. Omura, *Principles of Digital Communication and Coding*, New York: McGrw-Hill, 1979.

[42] E. Biglieri and P. J. McLane, "Uniform distance and error probability properties of TCM schemes," *IEEE Trans. Commun.*, vol. COM-29, NO. 1, pp. 41-53, Jan. 1991.

[43] S. Bendetto, M. Ajmon Marsan, G. Albertengo, and E. Giachin, "Combined coding and modulation: Theory and applications," *IEEE Trans. Inform. Theory*, vol. 34, NO. 2, pp. 223-236, March 1988.

[44] B. E. Rimoldi, "A decomposition approach to CPM," *IEEE Trans. Commun.*, vol. 34, N0. 2, pp. 260-266, March 1988.

[45] S. B. Slimane and T. Le-Ngoc, "Maximum likelihood sequence estimation of quadrature pulse-overlapping modulated signals for portable/mobile satellite communications," *IEEE J. Select. Areas Commun.*, vol. 10, NO. 8, October 1992.

[46] G. Lindell and C. -E W. Sundberg, "An upper bound on the bit error probability of combined convolutional coding and continuous phase modulation," *IEEE Trans. Inf. Theory*, vol. 34, N0. 5, pp. 1263-1269, Sept. 1988.

[47] T. A. Schonhoff, "Symbol error probability for M-ary CPFSK coherent and noncoherent detection," *IEEE Trans. Commun.*, pp. 644-652, June 1976.

[48] T. Aulin and C. -E. Sundberg, "Partially coherent of digital full response continuous phase modulated signals," *IEEE Trans. Commun.*, vol. COM-30, No. 5, pp. 1096-1117, May 1982.

[49] E. Biglieri, "High-level modulation and coding for nonlinear satellite channels," *IEEE Trans. Commun.*, vol. COM-32, NO. 5, May 1984.

[50] D. Chase, "A combined coding and modulation approach for communication over dispersive channels," *IEEE Trans. Commun.*, vol. COM-21, pp. 455-470, Mar. 1973.

[51] S. Yoshida, et al., "Causes of burst errors in multipath fading channel," *IEEE Trans. Commun.*, vol. 36, pp. 107-113, January 1988.

[52] D. Divsalar, M. K. Simon, "The design of trellis coded MPSK for fading channels: Performance criteria," *IEEE Trans. Commun.*, vol. COM-36, NO. 9, pp. 1004-1012, September 1988.

[53] R. J. C. Bultitude, "Measured characteristics of 800/900 MHz fading radio channels with high angle propagation through moderately dense foliage," *IEEE J. Select. Areas Commun.*, vol. SAC-5, NO. 2, pp. 116-127, February 1987.

[54] S. Stein, "Fading channel issues in system engineering," *IEEE J. Select. Areas Commun.*, vol. SAC-5, NO. 2, pp. 68-89, February 1987.

[55] Adel A. M. Saleh, et al., "A statistical model for indoor multipath propagation," *IEEE J. Select. Areas Commun.*, vol. SAC-5, NO. 2, pp. 128-137, February 1987.

[56] K. Pahlavan, "Wireless communications for office information networks," *IEEE Commun. Mag.*, vol. 23, pp. 19-27, June 1985.

[57] R. E. Khan et al., "Advances in packet radio technologies," *Proc. IEEE*, vol. 66, pp. 1468-1496, Nov. 1978.

[58] A. S. Acampora, J. H. Winters, "System applications for wireless indoor communications," *IEEE Commun. Mag.*, vol. 25, pp. 11-20, August 1987.

[59] P. J. Mclane et al., "PSK and DPSK trellis codes for fast fading, shadowed mobile satellite communication channels," *IEEE Trans. Commun.*, vol. 36, pp. 1242-1246, Nov. 1988.

[60] C. Loo, "A statistical model for a land mobile satellite link," *IEEE Trans. Vehic. Techn.*, vol. 34, pp. 122-127, August 1985.

[61] C. Loo, E. E. Matt, J. S. Butterworth, and M. Dufour, "Measurements and modeling of land-mobile satellite signal statistics," *1986 Vehic. Techn. Conf.*, Dallas, TX, May 20-22, 1986.

[62] J. K. Wolf, G. Ungerboeck, "Trellis coding for partial-response channels," *IEEE*

Trans. Commun., vol. COM-34, pp. 765-772, Aug. 1986.

[63] M. K. Simon, D. Divsalar, "The performance of trellis coded multilevel DPSK on a fading mobile satellite channel," *IEEE Trans. Commun.*, vol. 37, pp. 78-91, May 1988.

[64] S. C. Gupta et al., "Land mobile radio systems-a tutorial exposition," *IEEE Commun. Mag.*, vol. 23, pp. 34-45, June 1985.

[65] J. Massey, "Coding and modulation in digital communications," *in Proc. Int. Zurich Sem. Digital Commun.* Zurich, Switzerland, March 1974.

[66] M. L. Moher and J. H. Lodge, "TCMP-A modulation and coding strategy for rician fading channels,", *IEEE J. Select. Ar. Commun.*, vol. 7, NO. 7, pp. 1347-1355, dec. 1989.

[67] S . H. Jamali, T. Le-Ngoc, "A new 4-state TCM scheme for fast fading, shadowed mobile radio channels," *IEEE Trans. Veh. Tech.*, vol. VT-40, pp. 216-223, Feb. 1991.

[68] G. Ungerboeck, "Channel coding with multilevel/phase signals," *IEEE Trans. Inform. Theory*, vol. IT-28, NO. 1, pp. 55-67, January 1982.

[69] C. Scheegel, D. J. Costello, Jr., "Bandwidth efficient coding for fading channels: code construction and performance analysis," *IEEE J. Select. Areas Commun.*, vol. SAC-7, NO. 9, pp. 1356-1368, December 1989.

[70] A. C. Lee and P. J. McLane, "Convolutional interleaved PSK and DPSK trellis codes for shadowed, fast fading mobile satellite communication channels," *IEEE Trans. Vehic. Technol.*, vol. 39, NO. 1, pp. 37-47, Feb. 1990.

[71] S. V. Pizzi and S. G. Wilson, "Convolutional coding combined with continuous phase modulation," *IEEE Trans. Commun.*, vol. COM-33, NO. 1, pp. 20-29, Jan. 1985.

[72] S. B. Slimane and T. Le-Ngoc, "Coded offset-quadrature pulse-overlapping modulation techniques," *Globecom'92*, Orlando, Florida, December 6-9 1992.

[73] B. Rimoldi, "Design of coded CPFSK modulation systems for bandwidth and energy efficiency,", *IEEE Trans. Commun.*, vol. 37, N0. 9, pp. 897-905, Sept. 1989.

[74] G. D. Forney, Jr., and M. V. Eyuboglu, "Combined Equalization and coding using precoding," *IEEE Commun. Mag.*, pp. 25-34, December 1991.

[75] S. B. Slimane, and T. Le-Ngoc, "Coded quadrature pulse-overlapping modulation techniques for personal communications," *ICUPC'92*, Dallas, Texas, Sept. 29-Oct. 2, 1992.

[76] S. T. Andersson, N. A. B. Svensson, "Noncoherent detection of convolutionally encoded continuous phase modulation," *IEEE J. Sel. Ar. Commun.*, vol. 7, N0. 9, pp. 1402-1414, Dec. 1989.

[77] R. H. Deng, D. J. Costello, Jr., "High rate concatenated coding systems using multidimentional bandwidth-efficient trellis inner codes," *IEEE Trans. Commun.*, vol. 37, N0. 10, pp. 1091-1096, October 1989.

[78] T. Le-Ngoc, "A class of power and bandwidth efficient transmission techniques for digital radio communications systems," *Ph.D. dissertation*, U. of Ottawa, Ottawa, Canada, February 1983.

[79] J. S. Seo, and K. Feher, "Bandwidth compressive 64-state SQAM modems for non-linearly amplified SATCOM systems," *Int. J. Satell. Commun.*, vol. 9, pp. 149-154, 1991.

[80] P. Ho, J. Cavers, J. Varaldi, "The effect of constellation density on trellis coded modulation in fading channels," *VTC'92*, Denver, Colorado, May 11-13, 1992.

[81] S. B. Slimane and T. Le-Ngoc, "Coded quadrature pulse-overlapping modulated signals," *IEEE J. Select. Areas Commun.* (under review).

[82] S. W. Cheung, "Performance of a CE16QAM modem in a regenerative satellite system," *Int. J. Sat. Commun.*, vol. 7, pp. 425-434, 1989.

APPENDIX A

THE WEIGHT PROFILE OF THE QPOM ENCODER

In this appendix we present the weight profile of the QPOM encoder for different patterns **e**.

As an illustrative example consider the subset

$$\mathbf{A}_0 = \{0, 4, 8, 12\}.$$

When an error event $\mathbf{e} = 0001$ occurs, the subset $\mathbf{A}_0$ will be decoded to the subset

$$\mathbf{A}'_0 = \{1, 5, 9, 13\},$$

causing a non-zero Euclidean distance between the original channel signal and the decoded one. This distance is easily calculated and is given by

$$dist. = \{\alpha_3, \alpha_4, \alpha_3, \alpha_4\}.$$

The weight profile of the subset $\mathbf{A}_0$ with respect to the error event $\mathbf{e} = 0001$ is then obtained using Eq. (3.36)

$$F(\mathbf{A}_0, 0001, D) = 2(D^{\alpha_3} + D^{\alpha_4})$$

Following the same procedure, the weight profile of hard-limited QPOM signals is calculated and is given in the table bellow. The hard-limited QPOM encoder has a Uniform Euclidean Profile (UEP) as all subsets have the same profile.

Subset of Channel Signal	e	Weight Profile
A_i	0000	4
A_i	0001	$2(D^{\alpha_3}+D^{\alpha_4})$
A_i	0010	$2(D^{\alpha_3}+D^{\alpha_4})$
A_i	0011	$4D^{\alpha_2}$
A_i	0100	$2(D^{\alpha_3}+D^{\alpha_4})$
A_i	0101	$4D^{\alpha_2}$
A_i	0110	$4D^{\alpha_2}$
A_i	0111	$2(D^{\alpha_1}+D^{\alpha_5})$
A_i	1000	$4D^{\alpha_2}$
A_i	1001	$4D^{\alpha_2}$
A_i	1010	$4D^{\alpha_2}$
A_i	1011	$2(D^{\alpha_1}+D^{\alpha_5})$
A_i	1100	$4D^{\alpha_2}$
A_i	1101	$2(D^{\alpha_1}+D^{\alpha_5})$
A_i	1110	$2(D^{\alpha_1}+D^{\alpha_5})$
A_i	1111	$4D^{\alpha_0}$

where $i = 0, 1, \ldots, 3$.

APPENDIX B

DERIVATIVE OF A DETERMINANT OF ARBITRARY ORDER n

In this appendix, we consider the derivative of a determinant of arbitrary order n with respect to a given variable x.

Given an nxn matrix $\underline{A}$

$$\underline{A} = \begin{bmatrix} a_{11} & a_{12} & . & . & . & a_{1n} \\ a_{21} & a_{22} & . & . & . & a_{2n} \\ . & . & . & . & . & . \\ . & . & . & . & . & . \\ . & . & . & . & . & . \\ a_{n1} & a_{n2} & . & . & . & a_{nn} \end{bmatrix} \tag{B1}$$

where the elements a_{ij}'s are differentiable functions of a variable x.

If $det(\underline{A})$ denotes the determinant of the matrix $\underline{A}$ then

$$\frac{d}{dx} det(\underline{A}) = \sum_{i=1}^{n} \det(\underline{A}^{[i]}), \tag{B2}$$

where $\underline{A}^{[i]}$ represents the matrix $\underline{A}$ with its i th row derived with respect to x,

$$\underline{A}^{[i]} = \begin{bmatrix} a_{11} & a_{12} & . & . & . & a_{1n} \\ a_{21} & a_{22} & . & . & . & a_{2n} \\ . & . & . & . & . & . \\ a_{i1}' & a_{i2}' & . & . & . & a_{in}' \\ . & . & . & . & . & . \\ a_{n1} & a_{n2} & . & . & . & a_{nn} \end{bmatrix} \tag{B3}$$

with

$$a_{ij}' = \frac{d}{dx} a_{ij}$$

Proof

For $n = 2$,

$$det(\underline{A}) = \begin{vmatrix} a_{11} & a_{12} \\ a_{21} & a_{22} \end{vmatrix}$$

$$= a_{11}a_{22} - a_{21}a_{12}.$$

The derivative of $det(\underline{A})$ with respect to x is

$$\frac{d}{dx} det(\underline{A}) = a'_{11}a_{22} - a'_{21}a_{12} + a_{11}a'_{22} - a_{21}a'_{12}$$

$$= \begin{vmatrix} a'_{11} & a'_{12} \\ a_{21} & a_{21} \end{vmatrix} + \begin{vmatrix} a_{11} & a_{12} \\ a'_{21} & a'_{21} \end{vmatrix}$$

$$= det(\underline{A}^{[1]}) + det(\underline{A}^{[2]}). \tag{B4}$$

For $n = 3$, it is straightforward to verify that

$$\frac{d}{dx} det(\underline{A}) = det(\underline{A}^{[1]}) + det(\underline{A}^{[2]}) + det(\underline{A}^{[3]}). \tag{B5}$$

Now suppose that the above statement holds for the case of $(n-1)$, i.e. the derivative with respect to x of a given determinant of order $n-1$ is given by

$$\frac{d}{dx} det(\underline{A}) = \sum_{i=1}^{n-1} det(\underline{A}^{[i]}), \tag{B6}$$

then what is the derivative with respect to x of the determinant of a matrix of order n? If the matrix $\underline{A}$ is of order n, then its determinant can be written as the sum of the products of the elements of any row and their respective cofactors, that is,

$$\det(\underline{A}) = a_{i1}\det(\underline{C}_{i1}) + a_{i2}\det(\underline{C}_{i2}) + \ldots, a_{in} det(\underline{C}_{in}) \quad (i = 1, 2, \ldots, n) \tag{B7}$$

where $\underline{C}_{ij}$ is an $(n-1)x(n-1)$ matrix. In this way, the determinant $det(\underline{A})$ is defined in terms of n determinants of order $n-1$. Without loss of generality, we consider the case of $i = 1$. Taking the derivative of $\det(\underline{A})$ with respect to x gives

$$\frac{d}{dx}\det(\underline{A}) = a'_{11} det(\underline{C}_{11}) + a'_{12} det(\underline{C}_{12}) + \ldots, a_{1n} det(\underline{C}_{1n})$$

$$+ a_{11}\frac{d}{dx} det(\underline{C}_{11}) + a_{12}\frac{d}{dx} det(\underline{C}_{12}) + \ldots, a_{1n}\frac{d}{dx} det(\underline{C}_{1n}) \tag{B8}$$

However from from Eq. (B6) we have

$$\frac{d}{dx} det(\underline{C}_{ij}) = \sum_{l=1}^{n-1} det(\underline{C}_{ij}^{[l]}). \tag{B9}$$

Substituting Eq. (B8) into (B9) we obtain becomes

$$\frac{d}{dx} det(\underline{A}) = \sum_{i=1}^{n} a'_{i1} \det(\underline{C}_{1i}) + \sum_{j=1}^{n} a_{1j} \sum_{l=1}^{n-1} \det(\underline{C}_{1j}^{[l]})$$

$$= \sum_{i=1}^{n} a'_{i1} det(\underline{C}_{1i}) + \sum_{i=1}^{n} a_{1i} det(\underline{C}_{1i}^{[1]})$$

$$+ \ldots, \sum_{i=1}^{n} a_{1i} det(\underline{C}_{1i}^{[n-1]}).$$

Hence,

$$\frac{d}{dx} det(\underline{A}) = det(\underline{A}^{[1]}) + det(\underline{A}^{[2]}) + \ldots + det(\underline{A}^{[n]}), \tag{B10}$$

which is equivalent to Eq. (B4).